Interfacial and Stability Studies of Photocathodes for Hydrogen Evolution

Thesis by

Jingjing Jiang

In Partial Fulfillment of the Requirements for the degree of

Doctor of Philosophy

CALIFORNIA INSTITUTE OF TECHNOLOGY

Pasadena, California

2018

(Defended June 8th, 2018)

Jingjing Jiang
ORCID: 0000-0002-3109-229X

ACKNOWLEDGEMENTS

I would like to thank my advisor, Prof. Nathan S. Lewis, for letting me join his group and providing great support all the time. His intelligence and insight in science and research inspired and guided me to be a better scientist and researcher. He cares about students' lives too, which makes me feel that the Lewis group is a warm family.

I have special thanks for Nate and his wife Carol for being supportive during my foot injury. They were very caring after they heard of my injury. They called and emailed me, asking about my situation, making suggestions, referring me to their doctor and sharing their experiences. They relieved my fear for general anesthesia and surgery, and their knee walking device was so useful to walk around and go up and down stairs when my foot could not bear weight. I appreciate it very much.

I would also like to thank the Lewis group. Everyone is very kind and helpful, and they enthusiastically answer questions and have discussions if one has an unsolved scientific problem. I enjoyed our group gatherings including meetings, parties, retreats, and symposiums. It feels like a big warm family. Dr. Bruce Brunschwig is like a nice grandfather, and his patience and wisdom would calm down any anxiety from scientific and life concerns. He is also excellent at keeping the Molecular Materials Research Center (MMRC) running in great shape. Also, he is a handy person and has fixed many things in MMRC in a quick and inexpensive way. Dr. Kimberly Papadantonakis is very valuable in getting the important things (a.k.a., papers) done, making G131 Jorgensen cheerful, and keeping memories (a.k.a., photos) of the group alums. She is also known for her ironic jokes. Dr. Shu Hu, Dr. Teddy Huang, Dr. Rui Liu, and Dr. Ke Sun (alphabetically ordered by last name) provided me with much help when I started the research. Dr. Shu Hu was the person who taught me how to make electrodes from scratch. Dr. Teddy Huang trained me on atomic force microscopy (AFM) and offered continued support after he went to work in the Bruker Nano Inc. We also keep close touch in life. Dr. Rui Liu gave me a great deal of guidance in atomic layer deposition (ALD). Dr. Ke Sun had a lot of insightful discussions with me. I benefited very much from his extensive and intensive knowledge. I learned from them all on how to design and conduct scientific research. I also gained help and knowledge from senior graduate students, Dr. Erik Verlage, Stefan Omelchenko, Michael Lichterman, Fadl Saadi, and others. And I thank Ivan Moreno-Hernandez, Pai Buabthong for instrumentation and helpful discussion, Sisir Yalamanchili, Ethan Simonoff, Paul Nunez, Dr. Matthias Richter, Dr. Amanda Shing, Dr. Matt McDowell for instrumentation, and Dr. Xinghao Zhou for helpful discussions. There are so many people I would like to thank, and I may forget to include here. I would just like to thank everyone in the Lewis group here, as each of you has made the group a joyful place.

I want to thank Barbara Miralles, Mabby Howard, Christy Jenstad, and Jennifer Blankenship for their wonderful administrative work, the Materials Science Options Representative Prof. Brent Fultz, and the graduate dean Natalie Gilmore for their help and support. I also thank DOE and the Joint Center for Artificial Photosynthesis (JCAP) for funding.

I would also like to thank Professors Harry Gray, William Goddard, and William Johnson for serving on my thesis committee. I sincerely appreciate their time.

I am also thankful to Alice M. Sogomonian in the Caltech Health Center for keeping me healthy, and Dr. Thomas Harris for performing a successful surgery on my foot.

I thank my friends in and outside Caltech for their support and encouragement.

Lastly, I want to express thanks to my parents, for their strong support and love throughout the years. And I would like to give special thanks to my parents for accompanying and taking care of me during and after surgery. I could not have made it without you.

ABSTRACT

Photoelectrochemical (PEC) water splitting is a promising way to generate clean hydrogen fuel from water and sunlight. The ideal photocathodes for hydrogen evolution reaction (HER) should have good electrical contact and mechanical adhesion on the interface between the semiconductor and the catalyst, and be stable during operation. However, the interfacial properties and the stability have not been intensively studied. We investigated the electrical and mechanical properties on the nanoscale of the interface of commonly used Si/Pt nanoparticles (Pt-NPs) electrodes with Pt-NPs as a catalyst, and showed that the Pt-NPs have a weaker adhesion in electrolyte than in air, and less than half of the Pt-NPs carry high currents, limiting the performance of the common Si/Pt-NPs electrodes. Furthermore, we explored the interfacial engineering of using TiO_2 deposited by atomic layer deposition (ALD), and showed that annealed TiO_2 led to higher open circuit voltages than the as grown ones by the possible formation of an interfacial Si-O-Ti mixture layer. Besides, the stability and corrosion behavior of CdTe electrodes for HER in the dark was studied in 1.0 M H_2SO_4(aq) and 1.0 M KOH(aq). The conditions studied herein include the electrochemical corrosion when biased at -100 mV vs. the reversible hydrogen electrode (RHE), the chemical corrosion when left at open circuit voltage (OCV), and the electrochemical corrosion with an active HER Pt catalyst overlayer when biased at -100 mV vs. RHE. The corrosion comes mostly from chemical corrosion and is reduced at negative bias in electrochemical condition. With a Pt catalyst overlayer at -100 mV vs. RHE, the corrosion rate is further reduced, indicating the promising utilization of CdTe for HER in PEC cells.

PUBLISHED CONTENT AND CONTRIBUTIONS

The work in this thesis has been drawn from the following publications and manuscripts:

Jiang, J., Zhou, X., Sun, K. Enabling Small Band-Gap Semiconductors for Solar Fuel Conversion. (In preparation) Adapted for Chapter 1.

Jiang, J. participated in the writing of the photocathode part.

Jiang, J., Huang, Z., Xiang, C., Poddar, R., Lewerenz, H.-J., Papadantonakis, K. M., Lewis, N. S., Brunschwig, B. S. Nanoelectrical and Nanoelectrochemical Imaging of Pt/p-Si and Pt/p^+-Si Electrodes. *ChemSusChem* **10**, 4657 – 4663 (2017). DOI: 10.1002/cssc.201700893. Adapted for Chapter 2.

Jiang, J. participated in the conception of the project, imaged samples in the air and analyzed the data, assisted in the AFM-SECM experiments in the electrolyte, and participated in the writing and revision of the manuscript.

Jiang, J., Liu, R., Mayer, T., Mitrovic, S., Richter, M., Zhou, X., Sun, K., Papadantonakis, K. M., Brunschwig, B. S., Lewis, N. S. Understanding the Improvement of Photoelectrochemical Water Splitting on p-Si with Annealed Atomic Layer Deposited TiO_2. (In preparation) Adapted for Chapter 3.

Jiang, J. participated in the conception of the project, prepared samples, conducted electrochemical measurements, analyzed data, and participated in the writing and revision of the manuscript.

Jiang, J., Moreno-Hernandez, I., Buabthong, P., Papadantonakis, K. M., Brunschwig, B. S., Lewis, N. S. Chemical and Electrochemical Corrosion Study of CdTe Electrodes for the Hydrogen Evolution Reaction in Acid and Base. (In preparation) Adapted for Chapter 4.

Jiang, J. participated in the conception of the project, prepared samples, conducted electrochemical measurements and collected solution samples for ICP-MS, analyzed data, and participated in the writing and revision of the manuscript.

TABLE OF CONTENTS

Acknowledgements……...iii
Abstract ……v
Published Content and Contributions…….....vi
Table of Contents……vii
List of Illustrations ……..……...viii
List of Tables……...……xii
Nomenclature……xiii
Chapter I: Introduction 1
1.1 Water splitting and Photoelectrochemical (PEC) cells 2
1.2 Fuel forming photocathodes..... 4
1.3 Motivations..... 10
1.4 Contents of the thesis 10
Chapter II: Nanoscale Electrical and Mechanical Characterization of the Pt/Si Interface 12
2.1 Pt/Si sample fabrication 13
2.2 Nanoscale characterization of deposited Pt/Si..... 15
2.3 Resistance Measurements 18
2.4 Results..... 18
2.5 Discussion..... 35
2.6 Conclusion..... 38
Chapter III: Understanding the Improvement of Photoelectrochemical Water Splitting on p-Si with Annealed Atomic Layer Deposited TiO_2 40
3.1 Experimental..... 41
3.2 Results and discussion..... 45
3.3 Conclusion..... 58
Chapter IV: Corrosion Study of CdTe Electrodes for Hydrogen Evolution Reaction in Acid and Base 59
4.1 Experimental..... 59
4.2 Results..... 62
4.3 Discussion..... 73
4.4 Conclusion..... 78
Chapter V: Conclusions..... 79
Bibliography 80

LIST OF ILLUSTRATIONS

Number *Page*

1.1 Illustration for band alignment of semiconductor in acid to drive HER and OER. 3

1.2 Energy positions of the conduction band edge and valence band edge for several photocathode semiconductors. 5

1.3 Dependence of the theoretical maximum solar-to-hydrogen (STH) efficiency and the photocurrent density of photoelectrodes on the band gap under AM 1.5 G irradiation (100 mW cm^{-2}). 6

1.4 (top) Experimentally measured exchange current, log(i0), log(i0), for hydrogen evolution over different metal surfaces plotted as a function of the calculated hydrogen chemisorption energy per atom (top axis). (bottom) The result of the simple kinetic model now plotted as a function of the free energy for hydrogen adsorption.. 8

2.1 Topography, conductivity, and current-voltage (*I-V*) spectroscopy of Pt nanoparticles electrolessly deposited onto a p-Si substrate and measured in air 19

2.2 PF-TUNA scan of the same region of the Pt-NP/p-Si surface at 0.3 V shown in Figure 2.1 20

2.3 Expanded plot for Figure 2.1E 21

2.4 Topography and TUNA current for Pt nanoparticles electrolessly deposited onto a p- Si substrate captured by PF-TUNA. 23

2.5 Topography, conductivity, and current-voltage (*I-V*) spectroscopy of Pt nanoparticles electrolessly deposited onto a degenerately doped p^+- Si substrate and captured by PF-TUNA in air. 24

2.6 (A) Surface topography for a sample area imaged by classic tapping mode in air before the pushing process. (B) Surface topography of the same area in (A) imaged by classic tapping mode in air after the pushing process; and (C) line profiles for the four particles indicated in (A). (D)-(E) Zoomed-in views of particle #2 before (D) and after (E) pushing..... 25

2.7 Topography of electrolessly deposited Pt nanoparticles on a degenerately doped p^+- Si substrate as measured by PeakForce SECM using a SECM probe.. 28

2.8 Indentations remaining on the Si surface after the particles were moved away by the SECM probe in 0.1 M KCl(aq). 29

2.9 Electrochemical performance of a nanoelectrode probe used for PF-SECM imaging. 30

2.10 PeakForce SECM imaging of Pt nanoparticles electrolessly deposited onto a degenerately doped p^+- Si substrate and in contact with 10 mM $[Ru(NH_3)_6]^{3+}$ and 0.1 M KCl(aq).. 31

2.11 3D plot for Figure 2.10 33

2.12 Contour plot for Figure 2.10 34

3.1 *J-V* characterization of the Si/TiO_2/Pt heterojunctions in 1.0 M H_2SO_4 aqueous solution. 46

3.2 AFM images for the Si/TiO_2 heterojunctions before (a) and after (b) annealing. 47

3.3 a) V_{oc} of the Si/TiO_2/Pt heterojunctions in 1.0 M H_2SO_4 aqueous solution. b) Fill Factor of the Si/TiO_2/Pt heterostructures. 49

3.4 Efficiency of the Si/TiO_2/Pt heterostructures. 50

3.5 Mott-Schottky plots for (a) as grown and (b) annealed p Si/250 cycles TiO_2. 51

3.6 V_{oc} of the Si/TiO_2 heterojunctions in different redox couple solutions. 53

3.7 XPS spectra of O 1s for the Si/TiO_2 heterojunctions,

a) as grown samples; b) annealed samples 54

3.8 XPS spectura of Ti 2p for the Si/TiO_2 heterojunctions,
a) as grown samples; b) annealed samples 55

3.9 Band diagram of the Si/TiO_2 heterojunctions,
a) as grown samples; b) annealed samples 56

3.10 100 cycles CV of p-Si/250 TiO_2an/Pt and p-Si/Eless-Pt..... 57

3.11 XPS of Si 2p peaks of (a) fresh p-Si/Eless-Pt (b)
p-Si/Eless-Pt after 100 cycles CV (c) fresh p-Si/TiO_2an/Pt
(d) p-Si/250TiO_2an/Pt after 100 cycles CV 58

4.1 Chronoamperometry (current density vs. time) for the
n-CdTe electrodes (dark) biased at -100 mV vs. RHE
over 24 hours in H_2(g)-saturated (a) 1.0 M H_2SO_4(aq);
(b) 1.0 M KOH(aq). 63

4.2 (a-b) Concentrations of dissolved Cd, Te species in the
working compartment biased at -100 mV vs. RHE in
the dark over 24 hours, normalized to 1 cm^2 n-CdTe electrode
area and adjusted to 25 mL volume, in H_2(g)-saturated
(a) 1.0 M H_2SO_4(aq); (b) 1.0 M KOH(aq). (c-d) total amounts
of dissolved Cd, Te species in the working compartment
biased at -100 mV vs. RHE in the dark over 24 hours, normalized
to 1 cm^2 n-CdTe electrode area, in H_2(g)-saturated (c)
1.0 M H_2SO_4(aq); (d) 1.0 M KOH(aq). 64

4.3 SEM images of n-CdTe electrodes (a) before test; (b) after the
chronoamperometry test biased at -100 mV vs. RHE in the dark
over 24 hours in H_2(g)-saturated 1.0 M H_2SO_4(aq);
(c) after the chronoamperometry test biased at -100 mV vs. RHE
in the dark over 24 hours in H_2(g)-saturated 1.0 M KOH(aq). 65

4.4 (a-b) Concentrations of dissolved Cd, Te species in the
working compartment at open circuit voltage (OCV) in the
dark over 24 hours, normalized to 1 cm^2 n-CdTe electrode

area and adjusted to 25 mL volume. (c-d) total amounts of dissolved Cd, Te species in the working compartment at open circuit voltage in the dark over 24 hours, normalized to 1 cm^2 n-CdTe electrode area.. 67

4.5 SEM images of n-CdTe electrodes after being left at open circuit voltage in the dark for 24 hours 68

4.6 XPS of (a) Cd, (b) Te peaks of n-CdTe electrodes (dark). 69

4.7 Chronoamperometry for the n-CdTe electrodes (dark) with ~ 2nm sputtered Pt catalyst on the front surface biased at -100 mV vs. RHE over 24 hours in H_2(g)-saturated (a) 1.0 M H_2SO_4(aq); (b) 1.0 M KOH(aq). 70

4.8 Concentrations of dissolved Cd, Te species in the working compartment when ~ 2 nm Pt catalyst is applied and biased at -100 mV vs. RHE in the dark over 24 hours 72

4.9 SEM images of n-CdTe electrodes with ~ 2 nm sputtered Pt catalyst on the front surface after being biased at -100 mV vs. RHE in the dark for 24 hours in H_2(g)-saturated (a) 1.0 M H_2SO_4(aq); (b) 1.0 M KOH(aq). 73

LIST OF TABLES

Number *Page*

2.1 Results from fitting the *I-V* data for particles #1–3 to the thermionic emission equation with a series resistor. 22

2.2 Apparent mean diameters of the particles in Figure 2.6A and 2.6B before and after Nanoman pushing. 26

NOMENCLATURE

STH. solar to hydrogen.

***E*g.** band gap energy.

***J*sc.** short-circuit current density.

***V*oc.** open-circuit voltage.

AFM. atomic force microscopy

ALD. atomic layer deposition.

AM1.5. air mass 1.5 solar spectrum.

CV. cyclic voltammetry.

FF. fill factor.

HER. hydrogen evolution reaction.

KOH. potassium hydroxide.

OCV. open circuit voltage

OER. oxygen evolution reaction.

p+. highly-doped p-type material.

PEC. phtoelectrochemical.

PV. photovoltaic.

RHE. reversible hydrogen electrode

SCE. saturated calomel electrode.

SCEM. scanning electrochemical microscopy

SEM. scanning-electron microscopy.

TDMAT. tetrakis(dimethylamido)titanium.

XPS. X-ray photoelectron spectroscopy

Chapter 1

INTRODUCTION

Content in this chapter is drawn from the following publication:

Jiang, J., Zhou, X., Sun, K. Enabling Small Band-Gap Semiconductors for Solar Fuel Conversion. (In preparation)

Jiang, J. participated in the writing of the photocathode part.

Decarbonization of our current energy system from production to consumption while providing a secure energy supply for economic and population growth is important. This issue is one of the most important topics globally. The success of decarbonization will ultimately depend on production and use of fuels from renewable energy. Among all the forms of renewable energies, solar energy is by far the largest energy source known to man-kind. Solar energy reaches earth surface in any instant is equal to 130 million 500 MW power plants.[1] It is also more than all the other forms of renewables all combined. However, without storage, due to its intermittency, one can never a reliable energy system solely based on solar energy. Battery technology is a great technology, but too expensive to scale up due to its high cost and low energy density for grid-level storage. Meanwhile, transmission of electricity needs high capital cost and suffers high transmission loss. Liquid chemical fuels have advantages such as high energy and power density. They can also directly interface with our current infrastructures of storage and transportation. Therefore, directly storage of solar energy in the form of chemical fuels has attracted global attention.

There are different approaches to realize efficient solar fuel production. One way is to use photovoltaic/electrolyzer systems, which connects photovoltaic (PV) panels, modules or cells in series with an electrolyzer. However, the high systems cost leads to high fuel cost. Another way is to use a photoelectrochemical (PEC) cell system. This chapter will introduce the basics of photoelectrochemical water splitting, the photocathode part where the hydrogen

fuel is produced, and provides motivation for the study of the interface and stability of the photocathode.

1.1 Water splitting and Photoelectrochemical (PEC) cells

The water splitting reaction as in Equation 1.1 needs free energy of $\Delta G = 237.2$ kJ/mol to separate one molecule of H_2O to H_2 and ½ O_2, which corresponds to $\Delta E° = 1.23V$ per electron transferred, according to the Nernst Equation. [1]

$$H_2O \longrightarrow H_2 + \frac{1}{2}O_2 \qquad (1.1)$$

It can be separated to two half reactions, hydrogen evolution reaction (HER) and oxygen evolution reaction (OER). In acid, the half reactions are as below:

$$2H^+ + 2e^- \longrightarrow H_2 \qquad (1.2)$$

$$H_2O \longrightarrow \frac{1}{2}O_2 + 2H^+ + 2e^- \qquad (1.3)$$

While in base, the half reactions are:

$$2H_2O + 2e^- \longrightarrow H_2 + 2OH^- \qquad (1.4)$$

$$2OH^- \longrightarrow \frac{1}{2}O_2 + H_2O + 2e^- \qquad (1.5)$$

Equation 1.2 and 1.4 correspond to HER, and Equation 1.3 and 1.5 correspond to OER.

PEC water-splitting systems use sunlight and water as input and outputs hydrogen as fuel. It consists of two electrodes immersed in electrolyte. At least one of the electrodes is semiconductor material that absorbs light and convert solar energy into separated positive and negative charges. [2] [3] [4] Such an electrode is called a photoelectrode.

To use a single semiconductor and perform unassisted solar water splitting, the semiconductor needs to have a band gap energy (E_g) of >1.23 eV and the band edges of the conduction band and the valence band must straddle the electrochemical potentials $E°(H^+/H_2)$ and $E°$ (O_2/H_2O) as in Figure 1.1 to drive HER and OER.

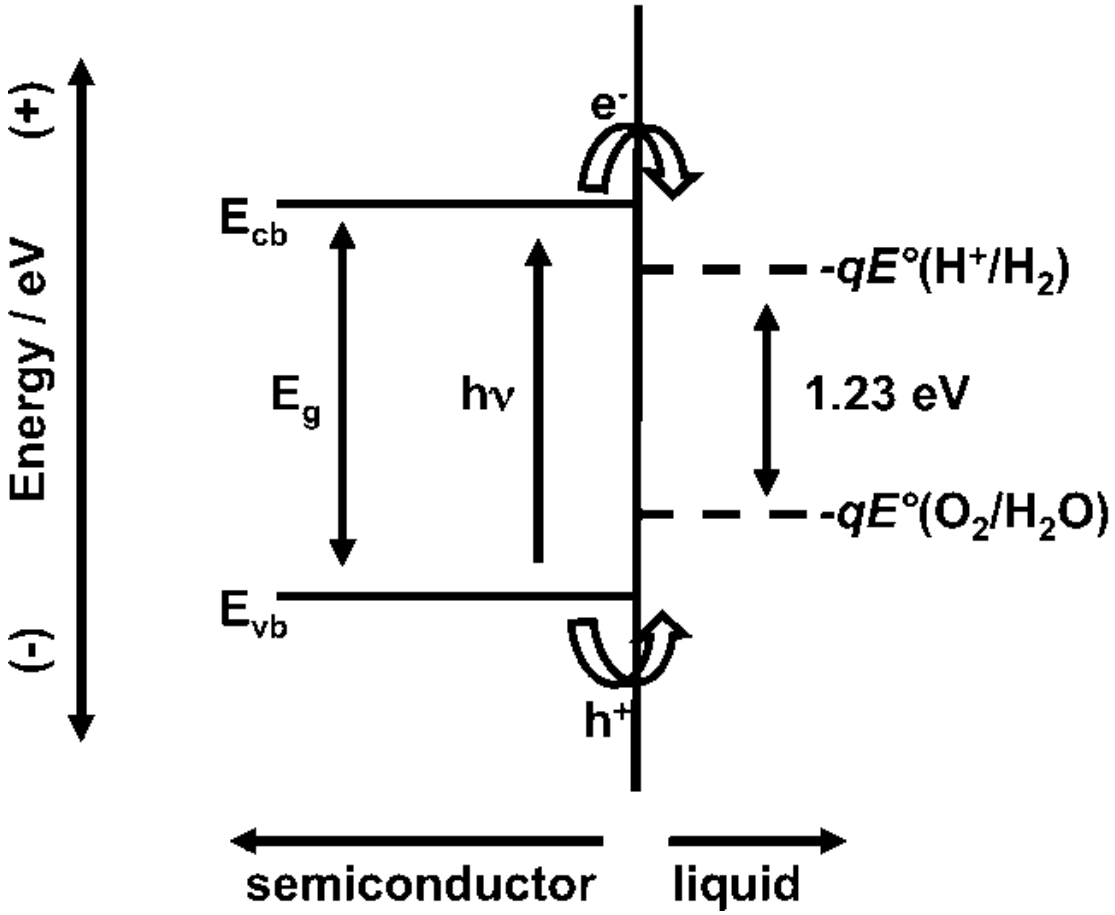

Figure 1.1 Illustration for band alignment of semiconductor in acid to drive HER and OER. Adapted from *Chem. Rev.*, 2010, 110 (11), pp 6446–6473, with permission from ACS Publications in copying and redistribution for non-commercial purposes under an ACS AuthorChoice License.

However, the actual energy required is higher due to overpotential losses for electrochemical reactions, resistances losses from every part of the charge transfer process, and finally, the pH difference between the reductive and oxidative compartments. Due to the non-radiative recombination either in the bulk or at surface, the potential can be affected, resulting in a higher band gap, and the photocurrent can be affected as well partially because of the reduced utilization of the solar spectrum from the increased band gap. This will effectively degrade the solar-to-fuel conversion efficiency. Systems using single materials without external energy input can be achieved at a cost of low efficiency. Moreover, it also requires a proper band edge alignment to the thermodynamic potentials of the reduction and oxidation reactions. So far there is no single material that can do solar fuel conversion effectively and efficiently.

A tandem design which stacks two semiconductors together would be able to result in a better chemical conversion efficiency.[1] This enables the use of small band-gap materials including traditional photovoltaic semiconductors such as Si, group III-V, and group II-VI semiconductor families.

1.2 Fuel forming photocathodes

In the tandem design, a photocathode can be coupled with a counter anode or photoanode to form a PEC water splitting device. In this configuration, the cathode is photoactive. Photogenerated electrons are driven by the band bending in the p-type semiconductor to the interface between semiconductor and solution, reducing protons (low pH) or water (high pH) to hydrogen gas, while photogenerated holes are swept to the bulk and combine electrons flown from the anode[1].

Photocathode materials

A good photocathode material should have the following properties: 1) The semiconductor should have proper band alignment relative to the water redox potentials. The conduction band minimum (CBM) of the p-type semiconductor should be more negative than the water reduction potential H^+/H_2. Band edge positions for some selected semiconductors are listed in Figure 1.2. 2) The semiconductor should have a small band gap to utilize the solar energy

efficiently. Theoretical maximum solar to hydrogen (STH) efficiency versus bandgap is shown in Figure 1.3. 3) It should be stable during operational condition. This includes that the semiconductor is either intrinsically stable or protected. 4) The recombination of carriers should be low to reduce loss of the solar energy conversion efficiency. 5) The semiconductor is earth-abundant and inexpensive to reduce the cost of PEC and to compete with traditional fossil fuels.[5, 6]

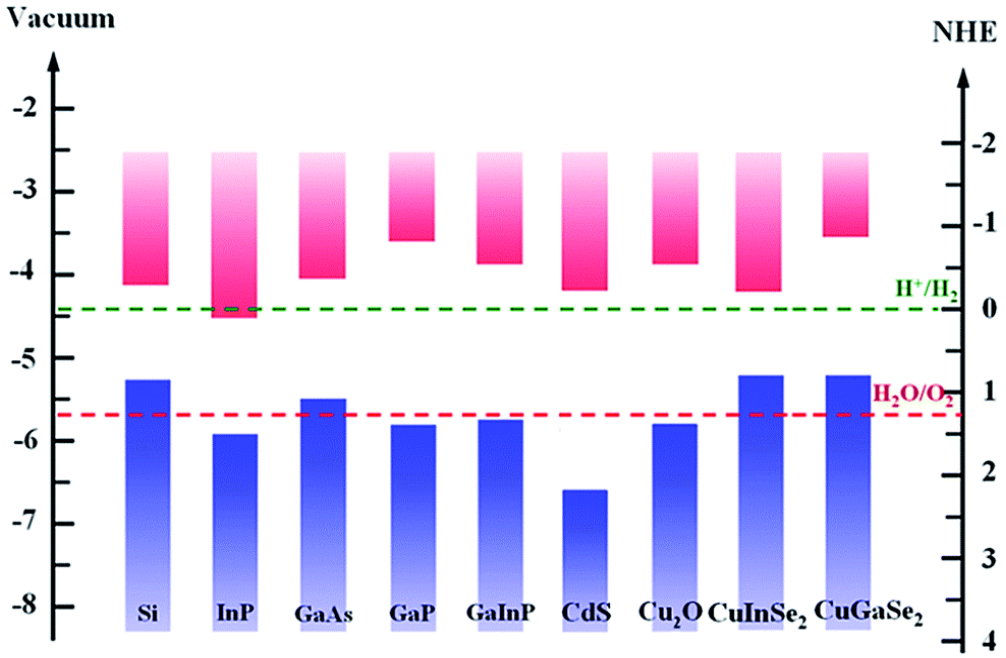

Figure 1.2 Energy positions of the conduction band edge and valence band edge for several photocathode semiconductors. Also shown as the dashed lines are the water oxidation/reduction potential levels[5]. Reprinted with permission from Royal Society of Chemistry.

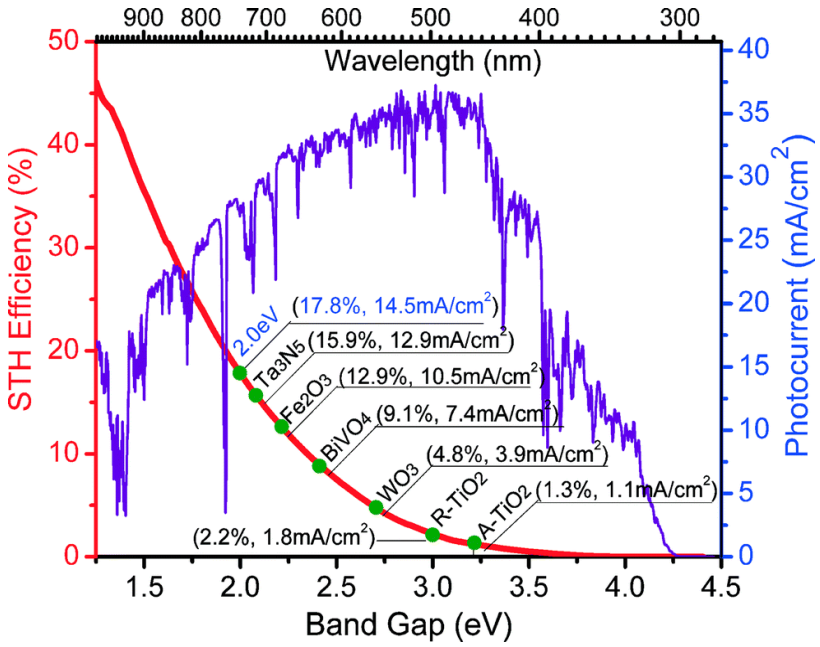

Figure 1.3 Dependence of the theoretical maximum solar-to-hydrogen (STH) efficiency and the photocurrent density of photoelectrodes on the band gap under AM 1.5 G irradiation (100 mW cm^{-2})[6]. Reprinted with permission from Royal Society of Chemistry.

To date, there has been no material which satisfies all the requirements. Research is still ongoing to look for such materials. Materials that have been explored include metal oxides, Si, III-V group semiconductors, chalcogenides, and II-VI group semiconductors.

Silicon has a bandgap of 1.12 eV, which is a desirable small band gap to be used in dual band gap PEC systems[1]. Moreover, p-type Si has a suitable conduction band edge for HER. Si is also earth-abundant, making the cost competitive. As a widely used material in the photovoltaic industry, fabrication and processing methods of Si are mature. Research on Si photocathodes involves protection and band energetics engineering. Si is readily oxidized in aqueous solution, which needs a protective layer.

CdTe is a suitable photocathode material for HER due to the proper band positions, optimum bandgap (1.44 V) and high absorption coefficient. Ohashi et al.[7] reported a photoelectrochemical cell composed of n-TiO_2 or n-$SrTiO_3$ with p-CdTe in 1M KOH and

was stable for over 12h. Mathew et al.[8] reported an enhanced photoelectrochemical performance on Ru modified p-CdTe.

HER catalysts

Small bandgap p-type semiconductors have been reported to have poor surface energetics for HER. To lower the activation energy and reduce overpotential, catalysts need to be incorporated onto photocathode surfaces to improve efficiency. Pt-group metals are known as the most efficient electrocatalysts for HER. Other Earth-abundant HER catalysts have also been explored.

Although expensive, Pt-group metals are the best HER catalysts. These state-of-art catalysts include Pt[9-11], Ir[12], and Ru[13]. Widely accepted mechanisms for HER on metal catalysts include formation of metal-hydrogen bond M-H during hydrogen adsorption, and chemical or electrochemical desorption in the second step. Therefore strength of the M-H bond plays a critical role in the reaction kinetics. If the bond is too weak, hydrogen does not bind to the catalyst and the proton/electron transfer step is slow. If the bond is too strong, hydrogen is hard to release from the M-H bond, and the second step is inefficient. Noble metals are at the peak of the volcano shaped exchange current density vs. M-H bond strength plot[14, 15] (Figure 1.4), which explains why they are the best HER catalysts, while metals on the left bind hydrogen too strongly and metals on the right bind hydrogen too weakly.

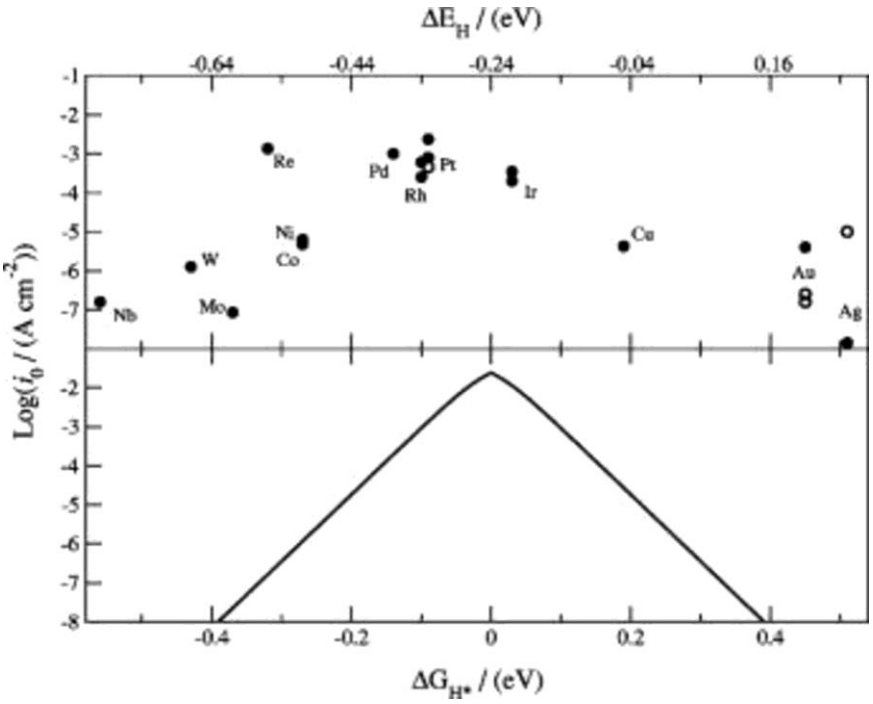

Figure 1.4 (top) Experimentally measured exchange current, log(i0),log(i0), for hydrogen evolution over different metal surfaces plotted as a function of the calculated hydrogen chemisorption energy per atom (top axis). Single crystal data are indicated by open symbols. (bottom) The result of the simple kinetic model now plotted as a function of the free energy for hydrogen adsorption. [15] Reprinted with permission from ECS and the Copyright Clearance Center.

Pt is mainly used in acidic solutions because the reaction pathway is relatively simple and well elucidated[16]. It shows less great activity in alkaline solutions[17]. Yet Pt in base still shows more superior activity than most non-noble metal HER catalysts[18].

Photocathode protection/stability

It is believed that corrosion is less severe for p-type semiconductor photocathodes than n-type semiconductor photoanodes, because photocathodes are protected under cathodic condition. It is true to some extent, for a single-element material like Si. Si is more stable when cathodically protected while it is easy to oxidize under anodic condition. However, for some compound semiconductor materials like III-V or Cu_2O, cathodic condition does not

prevent them from having reduction reactions. Even for p-Si photocathodes, surface oxidation is still an issue in idle conditions when the voltage is near open circuit potential, and a big issue when in alkaline solutions (Fig x.7 Si pourbaix diagram). What is worse is that even under cathodic protection, photocathodes are still readily oxidized. Research has shown that the dissolved O_2 concentration has to be less than 15 ppb to prevent silicon oxidation during HER, which is not practical for a commercial water-splitting device[19].

The Chorkendorff group has developed several protective layers for p-Si photocathodes in acid. They first used a thin Ti layer to protect an n^+p Si photocathode in 1.0 M $HClO_4$ for 1h[20], then they developed a 100 nm thick sputtered TiO_2 conductive protective layer on top of a thin Ti metal layer which protected an n^+p Si photocathode in 1.0 M $HClO_4$ during HER for 72 h[10]. Later on, they employed atomic layer deposition (ALD), which can deposit highly conformal and uniform coatings, to form a 100 nm TiO_2 layer on 5 nm Ti/n^+p Si photocathode. After being annealed in vacuum at 400 °C, this ALD TiO_2 layer protected the photocathode for 2 weeks with less than 5% degradation during continuous HER in 1.0 M $HClO_4$ for 30 days under constant illumination[21].

Other groups also used $SrTiO_3$[22], TiO_2[12, 23-25], and Al_2O_3[24, 26] to protect Si photocathodes in acid, with a stability from 35 h to 90 h. Protection of amorphous Si photocathodes have also been studied. With a TiO_2 encapsulation layer, Javey et al.[27] demonstrated a 12 h stability for a-Si photocathodes with a 10% decay.

Compared to the progress of protecting Si photocathodes in acid, there is not much work reported of protecting Si photocathodes in base, and the stable hours is not as long as in acid. Reisner et al.[28] reported a 4 h stability on a Ni-Ti composite film protected p-Si photocathode in an aqueous pH 9.2 borate solution. Dai et al.[29] also worked on a Ni/Ti film protected p-Si photocathode in base, and they achieved 12 h stability in 1 M KOH with a 100 mV decay, and 12 h stability in a pH 9.5 potassium borate buffer solution with negligible decay. Boettcher et al.[12] used F: SnO_2/TiO_2 to stablize n^+p Si in 1M KOH for 24 h. And Chorkendorff et al.[30] deposited TiO_2 by high power magnetron sputtering as a protective layer for an n^+p Si photocathode in 1M KOH running HER for over 24 h.

TiO_2 can also be used to protect other p-type semiconductor photocathodes like p-InP. An amorphous TiO_2 layer grown by ALD was able to protect p-InP nanopillars for more than 4 h with a stable HER photocurrent of 37 mA cm^{-2} in 1M $HClO_4$[13].

1.3 Motivations

Photoelectrochemical (PEC) water splitting is a promising way to generate clean hydrogen fuel from water and sunlight. Due to the sluggish kinetics for HER on most semiconductor surfaces, catalysts are usually needed. The interface between the catalyst and the semiconductor needs to be mechanically robust and able to conduct high electrical currents. A thorough understanding of the interface would be useful in designing HER photocathodes. However, the understanding of the interfaces is very limited, and mostly confined to macroscopic scale. So we want to have a more detailed study of the mechanical and electrical properties of the interfaces, and it is good to be on a microscale or a nanoscale. After understanding the interface, we would like to do some interfacial engineering as well.

Stability is also important for a good photocathode. Rigorous efforts have been made to stabilize photoanodes, with less focus made on the photocathodes part. CdTe is predicted to be stable thermodynamically in the pourbaix diagram from calculation, and has been used in photovoltaic devices. It would be interesting to study how stable it is under PEC operation conditions.

1.4 Contents of the thesis

In this thesis, interfacial studies of a common Si/Pt cathode were presented, and interfacial engineering has been explored with TiO_2 deposited between Si and Pt. Stability of another promising semiconductor material for photocathodes, CdTe, has been investigated under electrochemical and chemical corrosion conditions.

In Chapter 2, the interfacial properties of electrolessly deposited Pt nanoparticles (Pt-NPs) on p-Si and p^+-Si electrodes were investigated on the nanometer scale using a combination of scanning probe methods.

In Chapter 3, the interface between p-Si and Pt was engineered with TiO_2 by atomic layer deposition (ALD). The annealed TiO_2 showed a higher open circuit voltage V_{oc} than the as grown one. It was further investigated in aqueous and non-aqueous redox couple solutions and XPS to understand how the interfacial layer changed during annealing.

In Chapter 4, the stability/corrosion of dark CdTe electrodes were studied in 1M H_2SO_4 and 1M KOH, at -100 mV vs. RHE bias and at open circuit voltage. Chemical corrosion and electrochemical corrosion were compared, and corrosion of dark CdTe electrodes with Pt catalyst was also studied.

Finally, the work is summarized and the outlook for future research is discussed.

Chapter 2

NANOSCALE ELECTRICAL AND MECHANICAL CHARACTERIZATION OF THE PT/SI INTERFACE

Content in this chapter is drawn from the following publication:

Jiang, J., Huang, Z., Xiang, C., Poddar, R., Lewerenz, H.-J., Papadantonakis, K. M., Lewis, N. S., Brunschwig, B. S. Nanoelectrical and Nanoelectrochemical Imaging of Pt/p-Si and Pt/p^+-Si Electrodes. *ChemSusChem* **10**, 4657 – 4663 (2017). DOI: 10.1002/cssc.201700893.

Jiang, J. participated in the conception of the project, imaged samples in the air and analyzed the data, assisted in the AFM-SECM experiments in the electrolyte, and participated in the writing and revision of the manuscript.

Photoelectrochemical (PEC) water-splitting systems place catalysts for the water-splitting half-reactions in electrical contact with semiconducting photoelectrodes that convert light energy into separated positive and negative charges. [2] [3] [4] In such systems, the interfaces between the light absorbers and catalysts must provide a robust mechanical attachment of the catalyst to the surface as well as a pathway for charge to flow from the light absorber to the catalyst.

Electroless plating is a widely used method for the deposition of metal catalysts onto photoelectrodes.[31-34] Kulkarni and coworkers have summarized the history of electroless deposition methods, including optimization of plating conditions (concentration, pH, temperature, etc.), particle density on the surface, and proposed particle-growth mechanisms.[35]

Pt/Si interfaces show different electron transport behaviors for hydrogen production when Pt is deposited electrolessly relative to when Pt is deposited by e-beam evaporation.[34] X-ray photoelectron spectroscopy (XPS) indicates the formation of Si oxide at the interface

between the electrolessly deposited particles and the Si substrate, whereas no interfacial Si oxide is observed for evaporated Pt.[34] Further, weak adhesion has been observed for some metals films and nanoparticles (NPs) to Si surfaces with SiO_2 layers.[36-39]

The present understanding of interfaces between Pt NPs and Si substrates is derived primarily from macroscopic measurements, as opposed to methods that provide information about the electrical and electrochemical properties of individual NPs.[40],[41]

We describe herein the electrical and mechanical properties of individual electrolessly deposited Pt NPs on Si(111) surfaces as measured using atomic-force microscopy (AFM). The electrical and mechanical properties were measured both in air and in contact with an electrolyte. The surface topography and conductivity of electrolessly deposited Pt NPs were simultaneously imaged by AFM. The force needed to move the particles on the surface was measured, and the area under the particles examined. Furthermore, the conductance of the particles in contact with an electrolyte was mapped using AFM-based scanning electrochemical microscopy (SECM).

2.1 Pt/Si sample fabrication

Materials

Boron-doped, Czochralski-grown Si wafers with resistivities, ρ, of~ 7.5 (p-Si) and < 0.005 Ω·cm (p^+-Si) were purchased from Silicon Resource Inc. All other chemicals used were obtained commercially (see Supporting Information). H_2O with a resistivity of ≥18 MΩ·cm was obtained from a Barnstead Nanopure station (Thermo Scientific).

Fabrication of electrodes for microscopic studies

Prior to use, p-Si (111) and p^+-Si (111) wafers were cleaved into 2.0 × 3.0 cm or 3.8 x 3.8 cm chips. The chips were cleaned by immersion 1) for 15 min in an RCA 1 etching solution; 2) 30 s in buffered HF(aq); and (3) 15 min in an RCA 2 solution at 75 °C. The chips were then cut into 1.0 x 1.0 cm pieces, etched in buffered HF(aq) for 30 s, rinsed in H_2O, dried

with N_2(g) and immediately submerged in a Pt electroless plating solution for 45 s, followed by a thorough rinse with H_2O. The Pt electroless plating solution consisted of 1 mM H_2PtCl_6(aq) in 0.50 M HF(aq). A diamond scribe was used to scratch a Ga/In eutectic mixture (Aldrich) onto the back side of each Pt/Si chip.

Characterization of deposited Pt nanoparticles

Conductive AFM using PeakForce tapping (PFT) mode on a Bruker Dimension Icon atomic force microscope (AFM) was used to characterize the morphology, interfacial mechanics, conductivity and electrical properties of the electrode surfaces.[42] Conductivity imaging while mapping the surface topography was done using PeakForce Tunneling AFM (PF-TUNA).

AFM-SECM was done on the same Dimension Icon AFM using a PF-SECM with commercial probes obtained from Bruker. In PF-SECM, alternating line scans are run in PFT and lift modes. In lift mode, the tip does not oscillate and follows the topographical profile obtained by the previous PFT scan at a defined height above the surface. In this work, the lift height was 100 nm. The topography and conductivity of the sample were captured in PFT mode, and the electrochemical current was measured in lift mode. The currents during contact between the tip and the surface in the presence of an electrolyte were measured using a different algorithm than the contact currents measured in air by PF-TUNA.

For the electrochemical studies, an aqueous solution of 10 mM $[Ru(NH_3)_6]]^{3+}$ and 0.1 M KCl was used. A CHI760 bipotentiostat (CH Instruments, Texas) was used to control the electrochemical conditions. The electrochemical cell had a Pt wire counter electrode and a AgCl-coated Ag wire as a quasi-reference electrode (AgQRE). In the SECM scan the tip was biased at -0.4 V vs AgQRE to reduce the $[Ru(NH_3)_6]^{3+}$, while the sample was held at -0.1 V vs AgQRE to reoxidize any $[Ru(NH_3)_6]^{2+}$ generated by the AFM tip.

The RCA 1 etching solution contained 5:1:1 by volume of H_2O : H_2O_2(aq) (30%) : conc. NH_4OH (28%). The RCA 2 etching solution contained 5:1:1 by volume of H_2O : aq H_2O_2

(30%): conc. HCl(aq) (37%) and was maintained at 75 ºC. The solution for electroless deposition of Pt consisted of 1 mM H_2PtCl_6(aq) in 0.50 M HF(aq). A diamond scribe was used to scratch a Ga/In eutectic mixture (Aldrich) onto the back side of each Pt/p-Si chip. For AFM studies, 1.0 x 1.0 cm chip samples were mounted onto an SPM sample-mounting disk (SD-101, Bruker) using Ag paint (SPI, Inc.), and allowed to dry overnight. For PF-SECM measurements, a 3.8 x 3.8 cm p^+-Si chip was loaded onto a flat Cu foil of the same size, instead of a sample-mounting disk.

2.2 Nanoscale characterization of deposited Pt/Si

Peak Force tapping mode (PFT): In PFT mode, the probe was sinusoidally modulated at a low, off-resonance frequency. The frequency was 1 or 2 kHz with an amplitude of 100 or 150 nm. The feedback signal in PFT was the maximum force between the tip and the sample during every tapping cycle. The tip intermittently contacted the surface for ~ 100 to 300 μs. For surface topography mapping, ScanAsyst-air probes (Bruker) with a nominal tip radius of 2 nm were used. The surface was scanned using a relatively rapid line scan (left to right) while slowly moving the tip in the orthogonal direction (vertical in the plotted figures). Generally only data from the reverse scan direction (right to left, retrace) was used.

Peak-Force Tunneling AFM (PF-TUNA) mode: To capture current signals under an applied sample bias, an electronic module with a bandwidth of 10–20 kHz was used.[43] The PF-TUNA software algorithm allowed capture of currents during the period of maximum contact force, averaged over the contact duration (contact current), and averaged over the whole tapping cycle (TUNA current). The conductive probes used were SCM-PIT probes from Bruker with Pt/Ir coating layers and nominal tip radii of 20 nm. The imaging force was 5 – 10 nN.

For moving the particles in air, the Nano-Manipulation (NanoMan) software package was used with a TESPA probe (Bruker, nominal spring constant 40 N/m). After the sample was imaged using AFM conventional tapping mode, a script was written to control subsequent tip movements to push a particle. When pushing a particle, the tip stopped oscillation and maintained a 10 nm distance above the substrate surface while moving across the particle

from left to right. When the script was complete, the same area of the surface was re-imaged using conventional tapping mode.

Peak-Force Scanning Electrochemical Microscopy (PF-SECM): PF-SECM was used for local, in situ electrical and electrochemical measurements using commercially available nanoelectrode probes from Bruker. The probes were fully coated by SiO_2 except for the Pt conical tip apex with a height of ~200 nm and an end tip diameter of ~50 nm. The detailed electrochemical characterization of these probes has been reported previously.[44, 45] Electrochemical studies by PF-SECM were performed using an aqueous electrolyte solution of 10 mM $[Ru(NH3)_6]]^{3+}$ and 0.1 M KCl. The electrochemical cell had a Pt wire counter electrode and a AgCl-coated Ag wire as a quasi-reference electrode (AgQRE). A CHI760 bipotentiostat (CH Instrument, Texas) was used to control the electrochemical conditions. The probes were briefly tested by running a few cyclic voltammograms at a scan rate of 50 mV/s in the AFM electrochemical cell (Bruker). The surface area of the nanoelectrode probe was ~10^{-9} cm^2. [44, 45] A typical particle in the SECM image (Figure 2.7) had an apparent size of ~ 140 x 180 nm. If the particle is treated as a sphere of 160 nm, the surface area is ~10^{-9} cm^2. Thus when the AFM-SECM tip was in contact with a particle on the surface, the active area for $[Ru(NH_3)_6]]^{3+}$was approximately doubled.

In PF-SECM, the bipotentiostat was used in a 4-electrode scheme, in which the nanoelectrode AFM probe and the sample were working electrodes that shared the same reference and counter electrodes. For SECM imaging, the probe moved in an interleaved scan (PFT and SECM) pattern. First a forward and backward line scan (main scan) in PFT imaging mode captured the topographical profile. The topographical data were stored for use in the second, or lift, forward and backward line scan. During the lift scan, the tip did not oscillate and followed the stored topographical line profile at a defined height above the sample surface. In the lift scan, as in PFT, only the back or retrace scan data were used. The lift height was 100 nm. Electrochemical information was captured during the lift scan. In the SECM scan the tip was biased at -0.4 V vs AgQRE to reduce the $[Ru(NH_3)_6]^{3+}$, while the sample was held at -0.1 V vs AgQRE to reoxidize the $Ru(NH_3)_6]^{2+}$ generated by the AFM

tip. Approaching the tip to a highly resistive region on the surface where $[Ru(NH_3)_6]^{2+}$ is not reoxidized led to a reduction in tip current (negative feedback). For a conductive region where $[Ru(NH_3)_6]^{3+}$ was regenerated, a positive feedback was observed.[2a] These distinct responses allowed imaging the inhomogeneity of the conductance on the sample surface. Before SECM mapping, the approach curve (tip current vs tip-sample distance) of the nanoelectrode probe was measured on a particle-free region of the surface. The tip was biased at -0.4 V vs AgQRE.

During the PFT part of the PF-SECM scan, the conductivity of the sample was also measured. When the tip was in contact with a conductive species, two processes gave rise to an increased current. The nanoparticle can act as an enlarged SECM electrode and thus produce an increase in the Faradaic current. Also, the voltage difference between the tip and the sample can produce an electrical current during tip-sample contact. During the scan, the tip is in contact with the surface for only part of the tapping cycle, ~80 μs for a 500 μs tapping period (2 kHz tapping frequency, 0.5 ms/cycle). The captured current was acquired by the bipotentiostat and routed to the AFM controller for processing into an image, yielding the tapping-cycle-averaged current measured in the PF-SECM scan that is denoted herein as the tip-contact current. The actual contact current is thus ~ 6 times (500/80) the tapping-cycle-averaged current.

2.3 Resistance Measurements

p-Si resistance:

$$R = \rho \frac{l}{A} = 7.5\Omega \cdot cm \times \frac{0.05cm}{1cm^2} = 0.375\Omega$$

Pt particle (50 x 50 x 50 nm) resistance:

$$R = \rho \frac{l}{A} = 1.1 \times 10^{-7} \Omega \cdot m \times \frac{50 \times 10^{-9} m}{50 \times 10^{-9} nm \times 50 \times 10^{-9} nm} = 2.2\Omega$$

Pt/Ir tip resistance: **~10Ω from vendor**

2.4 Results

2.4.1 Topography and Conductivity of Pt/p-Si in air

Figures 2.1 and 2.2 show the AFM topography and conductivity data for a Pt-NP/p-Si electrode prepared using electroless Pt deposition. Figure 2.1A shows a typical scan of the Pt/p-Si sample. Analysis of multiple scans indicated that the width of the particles varied between ~20–150 nm while the height of the particles was between ~20–250 nm. Figures 2.1B - C show contact currents measured at sample biases of 0.3 and -0.3 V, respectively. The magnitudes of the currents were asymmetric with respect to the sign of the applied voltage. For example, at 0.3 V, the contact currents varied from the detection limit of <1 pA to 10^3 pA (Figure 2.2); while at -0.3 V, the reverse current ranged from ≤ 1 to 10 pA. No apparent correlation was observed between the contact currents at the two voltages (Figure 2.1D, blue-solid line at 0.3 V vs red-dotted line at -0.3 V), and little apparent correlation was observed between the current and the surface height (green-dashed). Only about half of the particles exhibited contact currents that were above the detection limit. For example, the topographic line profile shown in Figure 2.1 crossed 10 nanoparticles, but only 5 particles exhibited measurable currents (> 2 pA) when the sample was biased at 0.3 V.

The current-voltage (*I-V*) data measured for individual particles showed rectifying behavior; however, the *I-V* behavior under forward bias varied substantially from particle to particle. For particle #1, #2 and #3, the currents started rising at ~0, ~0.1 and ~0.3 V, respectively. No nanoparticle was present at location #4, and negligible current (-1.8 to -1.4 pA) was measured at this location.

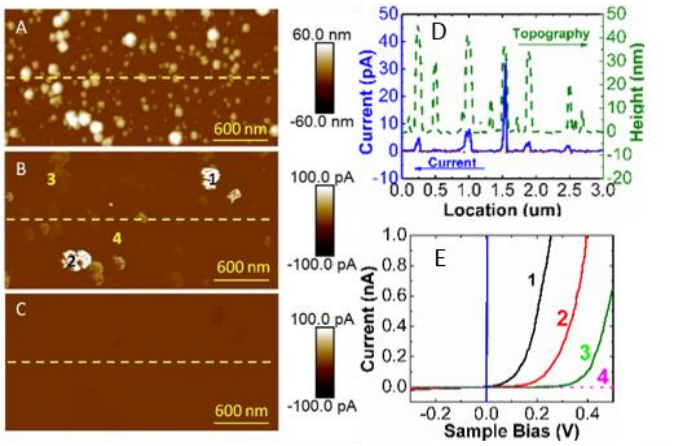

Figure 2.1. Topography, conductivity, and current-voltage (*I-V*) spectroscopy of Pt nanoparticles electrolessly deposited onto a p-Si substrate and measured in air. (A) Surface topography. (B) and (C) contact currents shown for sample biases of 0.3 V and -0.3 V, respectively. (D) Cross-sectional analysis of surface topography (green-dashed), contact current at 0.3 V (blue-solid) and -0.3 V (red-dotted) sample biases for the portion of the sample indicated by the yellow-dashed line in (A), (B) and (C). The left and right ordinates are contact current and surface topography, respectively. (E) Point-specific *I-V* characteristics for the locations corresponding to the labels in (B). The vertical blue curve is an *I-V* measurement from a Pt thin film deposited onto p-Si by electron-beam evaporation. The solid lines for curves 1-3 in E are fits to equation 1, while the blue solid line is a fit to Ohm's law. The fitted curves match well with the experimental curves. No nanoparticle was present at location 4.

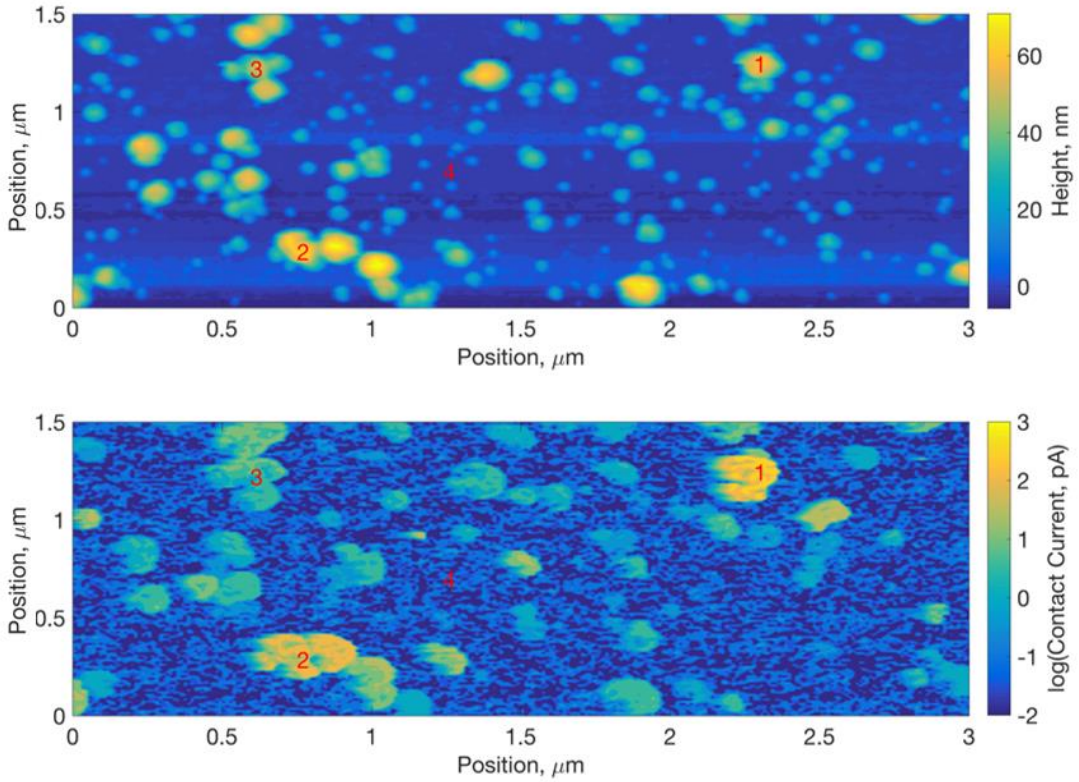

Figure 2.2 PF-TUNA scan of the same region of the Pt-NP/p-Si surface at 0.3 V shown in Figure 2.1. (top) Contour plot of the surface topography after flattening; (bottom) Logarithm of the absolute value of the current. Note that the larger particles showed contact currents, and notice that the observed currents varied by a factor > 1000. Replotted from Figure 2.1AB to more clearly show the variance in scale.

The *I-V* data of particles #1 – 3 were fitted to the thermionic emission equation (Equation 2.1) considering a series resistance in the circuit:

$$I(V) = AA^{*}T^{2}e^{\left(\frac{-q\varphi_B}{k_BT}\right)}\left[e^{\left(\frac{q(V-IR)}{nk_BT}\right)}-1\right] \qquad (2.1)$$

where *I(V)* is the current at voltage *V* relative to the equilibrium voltage; *A* is the junction contact area; *A** is the effective Richardson's constant (1.2×10^6 A m^{-2} K^{-2})[46]; *T* is the

absolute temperature, q is the unsigned charge of an electron, k_B is Boltzmann's constant; φ_B is the barrier height, n is the ideality factor, and R is the resistance of the sample. Fitted results are plotted as solid lines in Figure 2.1E, and the fitted values of φ_B, n, and R are listed in Table 2.1. The particles had barrier heights of ~ 0.55 V with resistances of 12 – 60 MΩ.

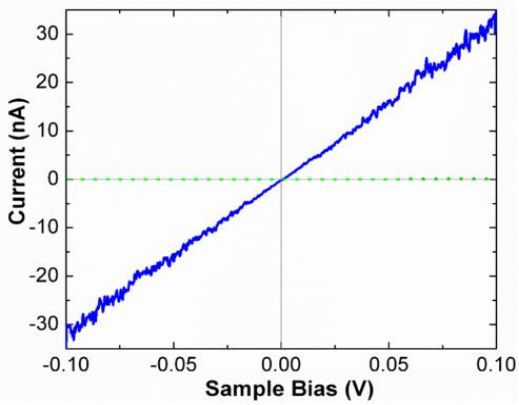

Figure 2.3 Expanded plot for Figure 2.1E. *I-V* data (blue solid line) captured from the Pt-TF/p-Si sample. The resistance obtained from the data was $3 \times 10^6\ \Omega$.

Figure 2.1E and Figure 2.3 show the *I-V* characteristics of a Pt thin film/p-Si (Pt-TF/p-Si) sample prepared using electron-beam evaporation. The data were spatially uniform, indicating that the deposition resulted in a homogenous metal thin film. A linear response was observed, Figure 2.3, within the range of the voltage scan, with a resistance of 3 MΩ, for the measured contact area.. A much larger current was observed for the Pt-TF/p-Si sample than for the samples prepared using electroless Pt deposition.

Table 2.1. Results from fitting the *I-V* data for particles #1–3 to the thermionic emission equation with a series resistor (Equation 2.1). Parameters are described in the text. The *I-V* data of the Pt thin film / p-Si was fitted to Ohm's law.

Particle	φ_B (eV)	n	R (MΩ)
1	0.53	1.5	49
2	0.52	2.6	12
3	0.57	1.4	63
Thin film	N/A	N/A	3

The results presented in Figure 2.1 were qualitatively similar for several replicate samples. For example, Figure 2.4 shows results from a different sample that was prepared following nominally the same procedures as the sample displayed in Figure 2.1. Both the 2D images as well as the 3D topographic images showed a highly dispersed distribution of particle sizes and a range of currents that spanned thousands of pA.

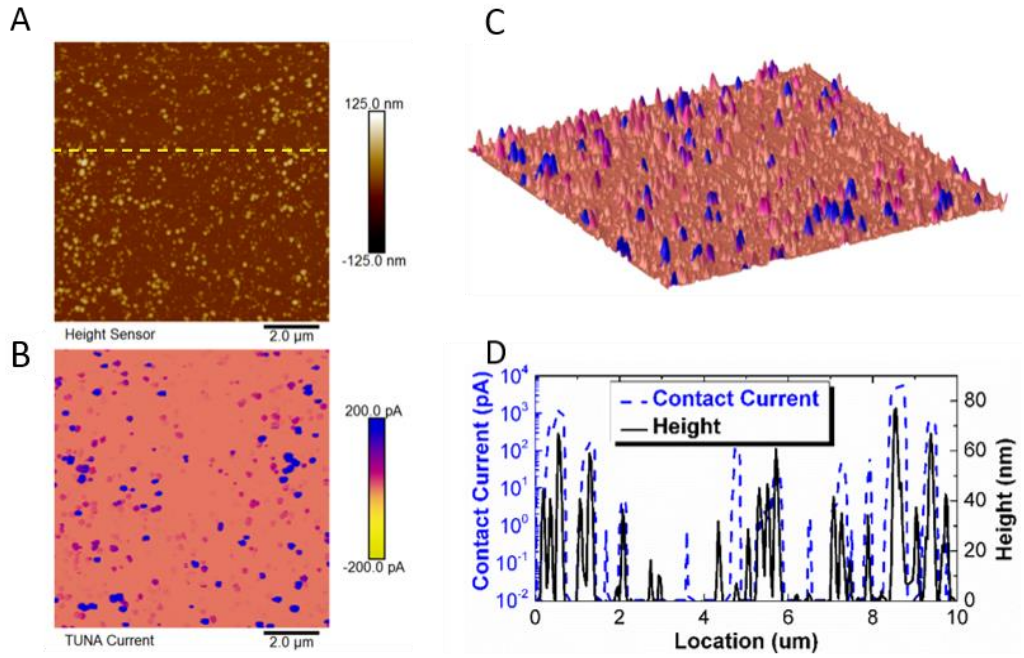

Figure 2.4. Topography and TUNA current for Pt nanoparticles electrolessly deposited onto a p- Si substrate captured by PF-TUNA. (A) Surface topography; (B) TUNA current at a sample bias of 0.5 V; (C) The 3-D rendering of the surface topography painted by the false-color current map; and, (D) Cross-sectional analysis of the surface topography (solid grey) and TUNA current (dashed blue) at the same sample location as indicated by the yellow dashed line in (A). As shown in Figure 2.1, the contact currents varied from the detection limit of <1 pA to 10^3 pA (Figure 2.2). Figures 2.2 and 2.4 both show this same amount of variation. The line profile plot in Figure 2.1D only shows currents < 40 pA, because the line was not drawn through any high current points, as shown in Figure 2.1B.

2.4.2 Topography and Conductivity of Pt/ p^+-Si in air

Conductivity (PF-TUNA) imaging and local *I-V* spectroscopy was also performed on Pt/p^+-Si electrodes made from either electrolessly deposited Pt nanoparticles or by e-beam deposition of a Pt thin film. The size and height distributions for the particles were ~20 - 150 nm and 30 – 300 nm, respectively, on a Pt-NP/p^+-Si sample (Figure 2.5A), similar to observations for the Pt-NP/p-Si sample. As seen in Figure 2.5B, only about one third of the particles showed conductive contrast on a 5 nA scale. The contact currents ranged from

~10 pA (for a particle not evident in the topographic image) to ~50 nA (a factor of 10^3 larger than for Pt-NP/p-Si). Figure 2.5C shows *I-V* data for the locations labeled in Figure 2.5A. Particles #1 and #2 showed relatively ohmic behavior in this measurement window, with resistances of 1.5 and 26 MΩ, respectively, between -50 and 50 mV. A Pt-TF/p^+-Si sample showed location-independent ohmic *I-V* data with a resistance of 2 kΩ.

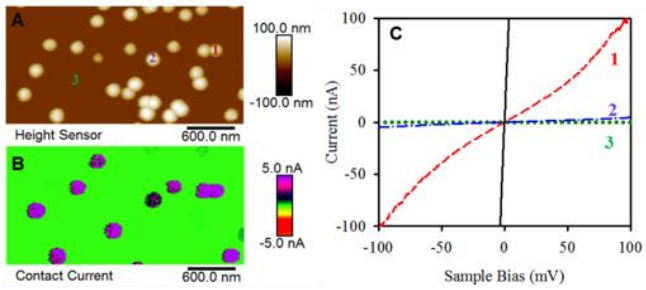

Figure 2.5 Topography, conductivity, and current-voltage (*I-V*) spectroscopy of Pt nanoparticles electrolessly deposited onto a degenerately doped p^+- Si substrate and captured by PF-TUNA in air. (A) Surface topography; (B) Contact currents for a sample bias of 0.1 V. (C) Point-specific *I-V* characteristics at locations corresponding to the labels on (A); no particle was present at location 3. An *I-V* plot for a sample with a thin film of Pt prepared by electron-beam evaporation on p^+–Si is also shown (black solid).

2.4.3 Adhesion for Pt-NP/p^+-Si in air

A TESPA probe was used to evaluate the adhesion of the particles to the substrate. The probe had a nominal spring constant of 40 N/m, ~20 times that of the SECM probe (2.2 N/m) used below. During the pushing process, a particle was first locally detected using conventional tapping mode. The tip oscillation was stopped and then the tip was held 10 nm above the surface while moving from left to right across a particle for more than 1 µm. Particles subjected to pushing had heights of > 150 nm.

Figures 2.6A-B present the surface topography for an area of the sample before and after the particle-pushing process for samples in contact with air.

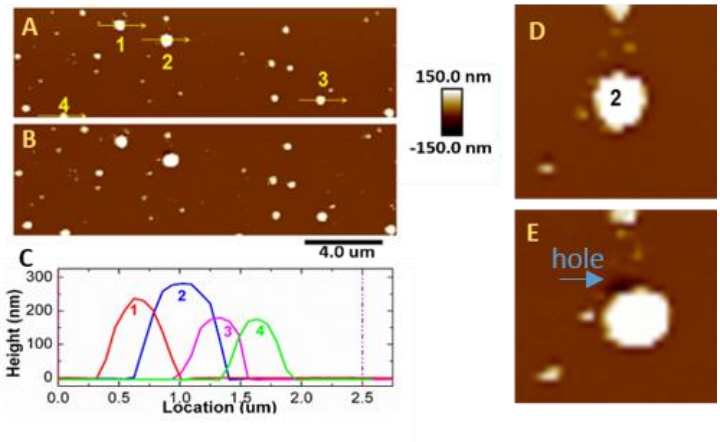

Figure 2.6 (A) Surface topography for a sample area imaged by classic tapping mode in air before the pushing process. Yellow arrows and numerical labels indicate the four particles subjected to pushing from left to right by the probe tip. (B) Surface topography of the same area in (A) imaged by classic tapping mode in air after the pushing process; and (C) line profiles for the four particles indicated in (A). From left to right are particle #1 (red line), #2 (blue line), #3 (pink line), and #4 (green line). (D)-(E) Zoomed-in views of particle #2 before (D) and after (E) pushing.

From the comparison, only particle #2 was moved by the force from the tip. Particle 2 was the particle with the largest height (~275 nm) for which pushing was attempted, and after particle #2 was moved, a small hole (200 nm width and 50 nm depth) was observed on the top left adjacent to the particle. For particles that remained in position, contact made by the

cantilever during the pushing attempt resulted in bending the cantilever > 100 nm, corresponding to a force of > 4 μN. This contact force would be expected to dull the tip. An ~10% increase in the mean apparent particle diameter was observed after pushing, consistent with dulling of the probe tip (Table 2.2).

Table 2.2. Apparent mean diameters of the particles in Figure 2.6A and 2.6B before and after Nanoman pushing.

	Before NanoMan (nm)	After NanoMan (nm)	Increment
Ensemble	368	402	9.2%
#1	558	598	7.2%
#2	648	743	14.7%
#3	412	458	11.1%

2.4.4 Adhesion for Pt-NP/p^+-Si in electrolyte

Figure 2.7 shows the topography for an electrode surface in contact with 0.1 M KCl(aq), as measured during a PF-SECM scan using an imaging force of 2.8 nN. The white arrows in Figure 2.7A and 2.7B indicate the slow-scanning direction for the 5 x 5 μm scan area. The scan rate of 1 Hz corresponded to a horizontal tip velocity of 10 μm s^{-1}. The SECM image was captured, following a PFT line scan, on the retrace cycle (right to left scan) during the lift mode. The Pt particles were swept away from their original locations during the prior PFT line scan, and were observed only in the upper-left-hand half of the image. A subsequent bottom-to-top scan showed particles only in the top left-hand corner of the scanning area (Figure 2.7B). High-resolution topographic imaging within the original scan area showed indentations in the Si surface left after the SECM scan, where the particles were located

originally, inferred from the size and distribution of the holes, and the particles were pushed to the edges of the surface. The depressions had depths between 0.2 and 0.8 nm and showed a variety of in-hole structures. Figure 2.8 shows the cross-sectional analysis of a typical hole, which exhibited a width and depth of ~150 and ~ 0.7 nm, respectively.

After SECM imaging in contact with the aqueous electrolyte, the sample was vigorously rinsed with a large quantity of water, dried under flowing N_2(g), and reimaged. Using the same SECM probe, a different area of the sample was examined in air with an imaging force of 4.3 nN, similar to the 5 to 10 nN force used by the PF-TUNA scans in air. The surface topography (Figure 2.6D) was similar to the Pt-NP/p^+-Si surface image in air obtained previously, Figure 2.5A. The sample was then soaked in 0.1, 0.5, and 1.0 M KCl(aq) for 2 h, rinsed with water, dried with N_2(g), and imaged again. These images indicated that the particles were not moved by the SECM probe when the surface was mapped in air.

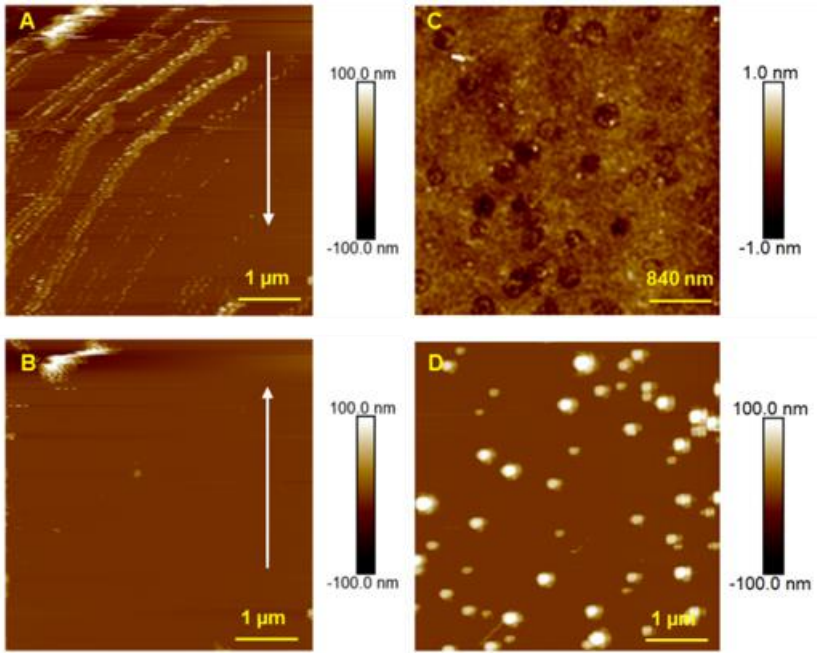

Figure 2.7 Topography of electrolessly deposited Pt nanoparticles on a degenerately doped p^+- Si substrate as measured by PeakForce SECM using a SECM probe. (A) Retrace (right to left scanning) image of the surface topography in 0.1 M KCl at an imaging force of 2.8 nN with a slow scanning direction from top to bottom, and (B) the subsequent bottom-to-top scan. The tip velocity was 10 µm/s. (C) Surface topography of the featureless area in (B) showing depressions in the surface where the particles were before being moved by the SECM probe. (D) Surface topography of a different area of the same electrode imaged in air at an imaging force of 4.3 nN after being vigorously rinsed with H_2O and dried under N_2.

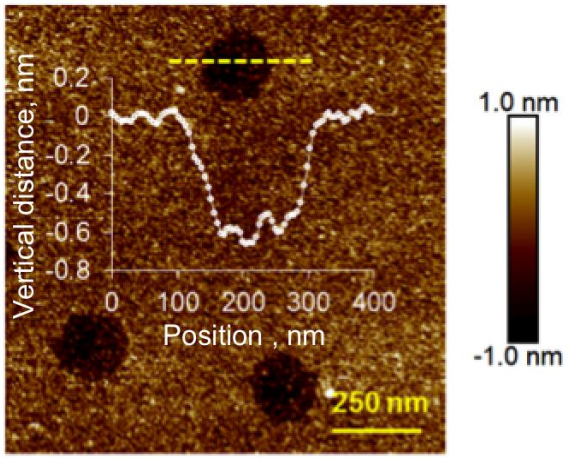

Figure 2.8 Indentations remaining on the Si surface after the particles were moved away by the SECM probe in 0.1 M KCl(aq). The on-image plot is a cross-sectional analysis of the line profile across a hole as indicated by the yellow dashed line.

2.4.5 SECM of Pt-NP/p^+-Si in electrolyte

The nanoelectrode SECM probe had a conical tip with an exposed active tip end that was ~50 nm in diameter and ~250 nm in height.[47] Figure 2.9A shows two cyclic voltammograms (CVs) for the probe used in imaging, with the sigmoidal shape typical of a nanoelectrode.

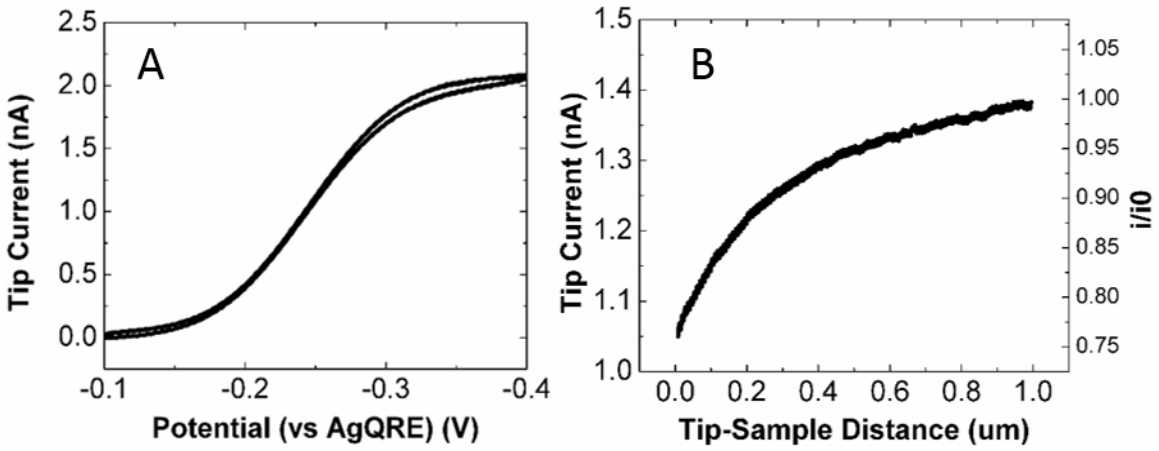

Figure 2.9 Electrochemical performance of a nanoelectrode probe used for PF-SECM imaging. (A) Two cyclic voltammograms measured in 10 mM $[Ru(NH_3)_6]^{3+}$ and 0.1 M KCl (aq) at a scan rate of 50 mV/s. A Pt wire was used as the counter electrode and a Ag wire coated with AgCl was used as the quasi-reference (AgQRE) electrode. (B) Approach curve (tip current vs tip-sample distance) captured under the same electrochemical conditions through force ramping the SECM probe at a triggered force of 10 nN and a ramp rate of 0.25 Hz. The normalized current is shown on the right ordinate axis.

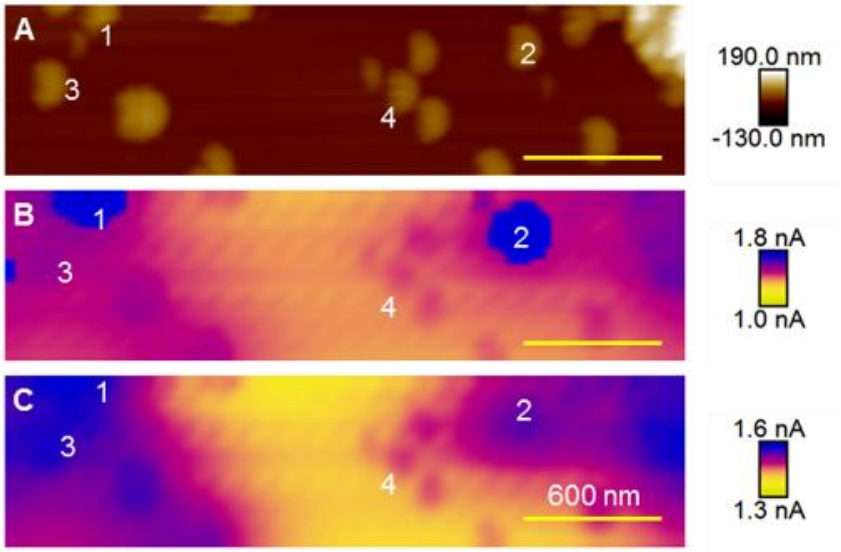

Figure 2.10 PeakForce SECM imaging of Pt nanoparticles electrolessly deposited onto a degenerately doped p^+- Si substrate and in contact with 10 mM $[Ru(NH_3)_6]^{3+}$ and 0.1 M KCl(aq) with an imaging force of 700 pN and a tip velocity of 1.2 µm/s. The nanoelectrode probe and the sample were biased at -0.4 V and -0.1 V vs a AgCl-coated Ag wire as a quasi-reference electrode (AgQRE), respectively. A 3 µm x 750 nm area was scanned. (A) Surface topography. (B) Tip-contact current captured during the main PeakForce-tapping scan. (C) Electrochemical current captured during the lift scan at a lift height of 150 nm. The scale bar is 600 nm.

To confirm that the measured current originated from the tip apex rather than the sides of the tip, the approach curve of the nanoelectrode probe was measured over a particle-free region of the Pt/p^+-Si electrode (Figure 2.9B) while the tip was biased at -0.4 V vs AgQRE to obtain a diffusion-limited current. The tip current decreased from 1.38 nA at a tip-sample distance of 1 µm to 1.05 nA when the tip was at the sample surface. The 25% reduction in current is consistent with simulations reported in previous work.[47]

A very low imaging force (700 pN) and small tip velocity (1.2 µm/s) were used to obtain PF-SECM measurements on a Pt-NP/p^+-Si substrate while minimizing movement of particles under the electrolyte. Figure 2.10A and Figures 2.11-2.12 show the surface topography in an

area where particles of sizes 20 to 250 nm were observed. The heights of these particles were between 30- 100 nm. Figure 2.10B shows the tip-contact current obtained from the main scan during the SECM imaging. These tip-contact currents had a distribution from ~ 1.37 nA for the background signal on a flat Si area to ~ 7 nA on particle #2. Except for particles #1 and #2, the tip-contact currents for all the other particles were < 1.6 nA (Figure 2.11). Region #4 was a cluster of 4 nanoparticles close together with sizes of ~ 120 x 180 nm. The tip-contact-current map barely differentiated between these four particles, as shown in Figure 2.10B.

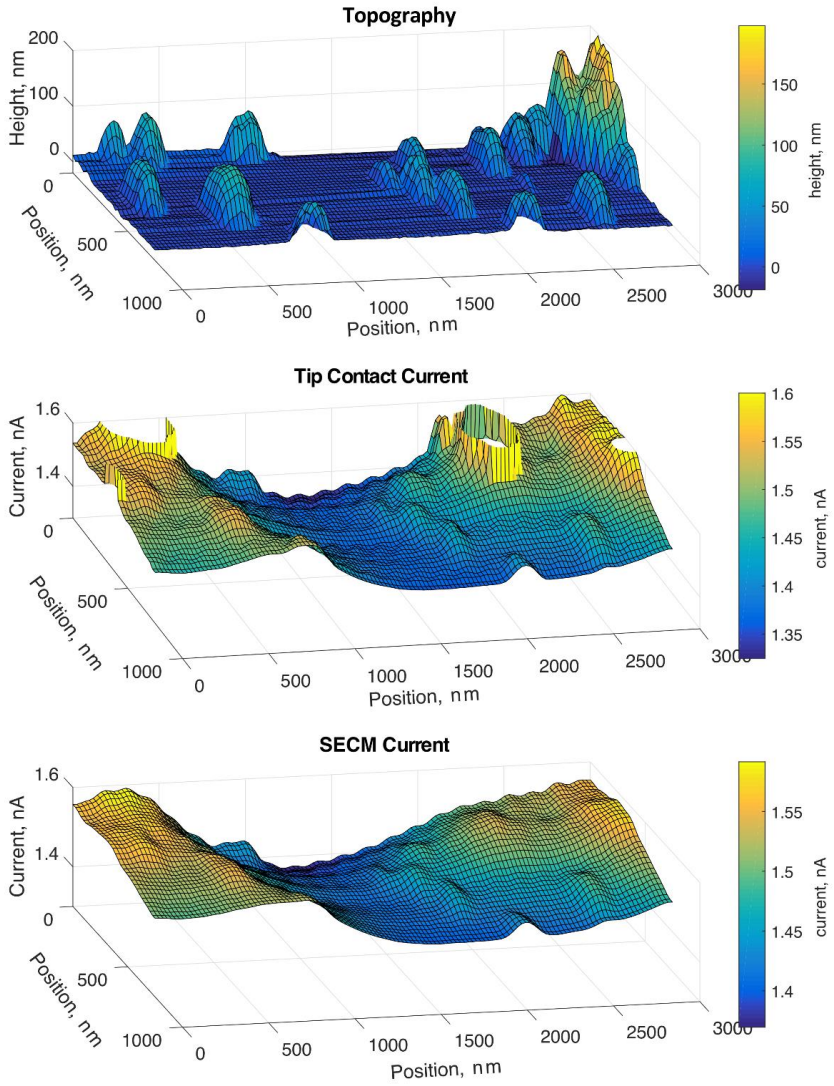

Figure 2.11 Same PeakForce SECM scans as shown in Figure 2.10 for Pt nanoparticles electrolessly deposited onto a degenerately doped p^+- Si substrate and measured in contact with 10 mM $[Ru(NH_3)_6]^{3+}$ in 0.1 M KCl(aq). (top) Topography of the surface; (middle) Plot of the tip contact current truncated at 1.6 nA; (bottom) Plot of the SECM current.

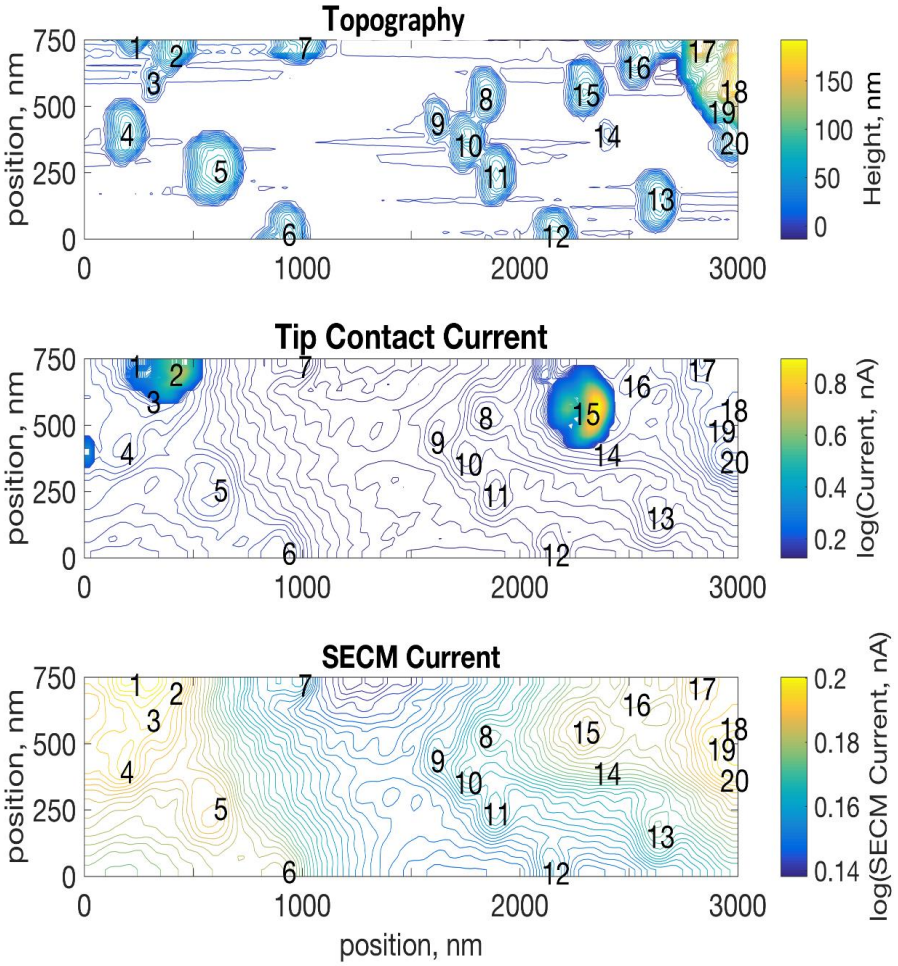

Figure 2.12 Same PeakForce SECM scans shown in Figure 2.10 for Pt nanoparticles electrolessly deposited onto a degenerately doped p^+- Si substrate and measured in contact with 10 mM $[Ru(NH_3)_6]^{3+}$ in 0.1 M KCl(aq). (top) Contour plot of the topography of surface; (middle) Contour plot of the common logarithm of the tip contact current; (bottom) Contour plot of the common logarithm of the SECM current.

Figure 2.10C shows the SECM current measured during the lift scans, while a tip-to-sample distance of 100 nm was maintained. The SECM current map, much like the tip-contact-current map, showed a more convoluted surface than the current maps in air, as evidenced

by a comparison of Figures 2.2 and 2.4 with Figure 2.11. This behavior was in part due to the Faradaic current observed even when the tip was in contact with an electrochemically inactive area of the surface. The SECM current near the center of the image was ~1.40 nA. For particles in region #4, the SECM current increased by ~ 50 pA, while the current increased by ~0.18, 0.14 and 0.17 nA for particles #1, #2 and #3, respectively. The electrochemical imaging resolved the particles in region #4. These correlated maps allowed comparison between the surface topography, contact current and SECM faradaic current for the different particles. For example, particle #2 and #3 both had sizes of ~120 x 200 nm and a height of ~65 nm, but particle #2 had a tip-contact current ~ 5 times larger than that of #3 while exhibiting an SECM current ~20% less than particle #3.

KCl (aq) at a scan rate of 50 mV/s. A Pt wire was used as the counter electrode and a Ag wire coated with AgCl was used as the quasi-reference (AgQRE) electrode. (B) Approach curve (tip current vs tip-sample distance) captured under the same electrochemical conditions through force ramping the SECM probe at a triggered force of 10 nN and a ramp rate of 0.25 Hz. The normalized current is shown on the right ordinate axis.

2.5 Discussion

$PtCl_6^{2-}$ and $PtCl_4^{2-}$ are strong oxidants (E^0 ~ 0.7 V vs NHE for the $PtCl_6^{2-}/PtCl_4^{2-}$ and $PtCl_4^{2-}$ /Pt couples). Thermodynamically, these metal cations can oxidize Si, and in the presence of water, SiO_2 can form on the surface, eq 2.2.

$$H_2PtCl_6 + Si^0 + 2\,H_2O \rightarrow Pt^0 + SiO_2 + 6\,HCl \qquad (2.2)$$

$$SiO_2 + 6\,HF \rightarrow H_2SiF_6 + 2\,H_2O \qquad (2.3)$$

Since metal deposition is hindered by the presence of SiO_2 on the Si surface, HF(aq) was added to the deposition solution to remove the SiO_2, eq.3. However, the oxide is not completely removed under the Pt nanoparticles.[34] The data reported herein underscore the impact on the interfacial conductivity and energetics of this interfacial oxide layer between the Si and the Pt particles.

The electron affinity of bulk Si(111) has been estimated to be 4.05 eV[48] and the Si band gap is 1.12 eV. Thus, under flat-band conditions, the valance-band edge of Si is located at a potential of 5.17 V vs vacuum.[48] Pt has a work function of ~5.6 eV[49], so the band positions suggest that an ideal Pt/Si contact would be ohmic, as is generally observed for p-Si.[46] The rectifying behavior observed on the nanoparticle samples can thus be attributed to the interfacial Pt-NP/Si junction, which produces a resistive diode-like junction. Although a resistive junction is not desired for kinetic reasons (current), the observed high barrier height due to the rectifying junction benefits the energetics (photovoltage).

The Pt-NP/p^+-Si samples yielded ohmic behaviors, as expected for two metallic materials in contact, even if a thin oxide layer exists at the interface. The Pt-NP/p^+-Si junction was more conductive locally than the Pt-NP/p-Si junction (1.4-26 vs 10-60 MΩ), similar to observations for the Pt-TF/p-Si. The high resistances observed for the particles may be due in part to the SiO_2 layer between the silicon and the Pt-NPs.

The mechanical adhesion is not robust between a Pt thin film and Si. An interfacial adhesion layer is consequently normally required when Pt is deposited by physical vapor deposition onto Si substrates. For a Pt thin film deposited directly on Si, imaging forces of < 10 nN did not damage the surface in air. The Pt-NP/Si sample showed strong mechanical attachment of the particles to the substrate in air, and even a stiff cantilever did not push the particles away from the surface. However, the adhesion changed substantially in aqueous solution, and under such conditions intermittent contact imaging with a force < 1/20 of that used in air pushed the Pt nanoparticles out of the imaging scan. The presence of an electrolyte may change the interfacial energetics at the semiconductor/metal junctions,[50-52] and such changes may be due to the change of interfacial mechanics.

Movement of the particles on the surface allows study of the surface of the substrate that was originally beneath the particle. The metal particles were partially embedded into the Si surfaces (Figures 2.7 and 2.8),[23, 2][53, 54] and the surface indentations varied, typically being < 1 nm in depth.

Although only loosely attached to the Si surface when in contact with an electrolyte, currents were passed by the particles, with some particles supporting high current densities. For example, the tip-contact current depicted in the SECM scans of Figures 5B and S7 was > 7 nA for particle #2. The tip was in contact with the particle for only a small part of the tapping cycle, so the contact current was actually ~ 6 times larger than the measured current, or > 40 nA (see PF-SECM in experimental). For a particle of ~3 × 10^4 nm^2, this value corresponds a current density of ~ 10^2 A cm^{-2}.

The tip-contact current observed during the SECM scan results from two sources: 1) current due to the potential difference between the tip and the substrate, and 2) current due to the reduction of $Ru(NH_3)_6^{3+}$ in solution. The SECM tip is a Pt-coated cone ~250 nm in height, and therefore remains exposed to the solution even when in contact with the surface.[55] For samples in contact with an electrolyte, the reduction current measured during tip contact can thus increase relative to the current measured during lift mode. Substantial tip-contact current can thus be present even in areas that do not contain particles.

The SECM current varied from 1.37 to 1.6 nA at 100 nm above the surface, whereas the diffusion-limited current at 1.0 μm above the surface was ~ 1.4 nA, Figure 2.9. The SECM currents measured above the Pt-NP/p^+-Si surface were <1.6 nA, with the SECM current surface showing small peaks on a convoluted surface, Figure 2.11-S7.

The observed tip-contact current showed a minimum value of about 1.3 nA, slightly less than the minimum SECM current. The approach curve data, Figure 2.9B, suggest that the tip-contact current for a particle-free region would show ~ 10% lower currents than the SECM current obtained 100 nm above the surface. A tip-contact current of ~1.3 nA is thus expected even in a particle-free region, in accord with observations. Moreover, all of the NPs observed in the topological scan should show a tip-contact current > 1.3 nA due to the enlarged effective tip area, again in accord with observations.

Only three particles showed a tip-contact current > ~1.6 nA, Figure 2.12, suggesting that most of the particles observed were not in electrical contact with the surface and only showed

reductive current due to diffusion in the solution. This observation agrees with the PFT scans in air, which indicated that only about half of the particles showed a contact current.

The SECM current surface had a convoluted shape that closely matched that of the tip-contact current surface (if one ignores the three large peaks, Figure 2.11). The similarity of the SECM and tip-contact current surfaces is expected if the source of both currents is primarily due to reduction of $Ru(NH_3)_6^{3}$. The tip-contact current for some of the particles was ~7 nA, e.g., particle #2 in Figure 2.10B, which is a much larger current than that displayed by most of the other particles. In such cases, current flowing through the Si via the Pt NP to the tip contributes substantially to the total current. If the actual contact current for particle #2 is ~40 nA, as estimated above, then the resistance for current flow through the particle is ~ 10 MΩ, consistent with the measurements made in air.

The variation in contact and SECM currents, as well as the differences in the depressions under the particles, suggest that the electrochemical performance of electrolessly deposited Pt particles is not only the result of the uniformly low activity of all the particles, but also arises from the wide range of conductance through the particles that allows only some of the NPs to contribute substantially to the bulk electrochemical activity of the surface.

2.6 Conclusion

Scanning probe AFM-based topographical, electrical, mechanical, and electrochemical measurements were used to investigate the interfaces between electrolessly deposited Pt nanoparticles and p-type Si surfaces, both *ex situ* in air and *in situ* during electrochemical reactions. Highly size-dispersed and randomly distributed particles were observed on the electrode surfaces. About one third of the particles did not exhibit observable contact currents, and another third of the particles exhibited only low contact currents. A factor of 10^3 difference was observed between the contact currents of the particles in air. Local current-voltage measurements revealed a rectifying junction at the Pt-NP/p-Si interface with a local resistance of $\geq$ 10 MΩ, whereas an Ohmic junction with a local resistance of $\geq$ 1 MΩ was observed at the Pt-NP/p^+-Si interface.

The electroless deposition resulted in particles that were slightly embedded into the Si. The particles were mechanically well attached to the sample surface in air, whereas in contact with an aqueous electrolyte the adhesion of the particles to the surface was substantially weaker, and surface imaging required the use of sub-nN force.

When Pt-NP/p^+–Si samples in contact with an electrolyte were imaged in SECM mode, tip-contact currents were observed for all of the particles. However, for the majority of the particles, the current was only due to reduction of the redox couple in solution and not to conduction from the Si substrate. For the particles with the highest currents, conduction through the Si dominated the current, with the particles having a resistance of ≥ 10 MΩ. The electrical conduction through many of the particles, both in air and under the electrolyte, showed that the electrochemical performance of electrolessly deposited Pt particles was the result of 1) many of the particles not being in electrical contact with the silicon substrate, 2) the high resistance between the NPs and the silicon substrate, and 3) the low adhesion of Pt NP to the Si surface. Thus, the bulk electrochemical activity electrolessly deposited Pt NP on Si electrodes is a consequence of the current in such devices being carried only by a fraction of the Pt particles.

Chapter 3

UNDERSTANDING THE IMPROVEMENT OF PHOTOELECTROCHEMICAL WATER SPLITTING ON P-SI WITH ANNEALED ATOMIC LAYER DEPOSITED TiO_2

Content in this chapter is drawn from the following publication:

Jiang, J., Liu, R., Mayer, T., Mitrovic, S., Richter, M., Zhou, X., Sun, K., Papadantonakis, K. M., Brunschwig, B. S., Lewis, N. S. Understanding the Improvement of Photoelectrochemical Water Splitting on p-Si with Annealed Atomic Layer Deposited TiO_2. (In preparation)

Jiang, J. participated in the conception of the project, prepared samples, conducted electrochemical measurements, analyzed data, and participated in the writing and revision of the manuscript.

Many small band gap semiconductor photocathodes that are potentially useful for water splitting are unstable towards decomposition or surface reactions under illumination in aqueous electrolytes.[56] Relatively thick films of TiO_2 have recently been used successfully as a protective layer for photocathodes, which functions as an electron conductor by charge carrier movement in the TiO_2 conduction band.[57-62] The interfacial energetics between the semiconductor and the electrolyte, and the ability to tune the energy of the photogenerated electrons that couple to the electrocatalysts on top of the TiO_2 film, have not been well elucidated. Understanding and controlling energetics of these heterojunctions are crucial to the utilization of this approach for protection of small band gap semiconductors such as Si, GaAs, and GaP for the solar-driven water splitting.[63] Thus, detailed studies of the interfacial energetics of semiconductor interfaces with TiO_2 will be performed as the key focus of this field.

In this application of TiO_2, the photogenerated electrons are usually presumed to be transferred through the relatively thick TiO_2 coating by electron conduction/hopping in the

TiO_2 conduction band. Therefore the energy of the photogenerated electrons that is transferred to the catalyst should be dictated by the energy of the TiO_2 conduction band edge. Therefore, the simplistic picture of electrons having the potential on the TiO_2 conduction band edge clearly does not apply to this situation since the difference between the water reduction potential (V_{HER}) to TiO_2 conduction band edge are too close to support high efficient water reduction current. Additionally the value of the photovoltage should be affected both by the photocathode/TiO_2 interface and the redox potential of the electrolyte plus the water reduction catalyst.

In this study, we deposit TiO_2 onto the surface of silicon by employing the atomic layer deposition (ALD). As an earth abundant material, silicon stands out as one of the most promising semiconductors, with its outstanding good performance on light absorption, incident photon to electron conversion efficiency, charge transfer property, etc. for solar energy driven devices. As a photocathode, the electrons generated by solar irradiation in silicon easily flow from its conduction band into the TiO_2 passivation layer, and are then injected into the electrolyte for reduction reactions. By using ALD, the condition of TiO_2 layer on Si surface can be carefully controlled. Investigating the passivation layer thickness effect, the annealing effect, and the redox potentials influences in this paper can help to understand the energetic structure of Si/metal oxide heterostructures and the origins of improving water splitting efficiency.

3.1 Experimental

Substrate preparation

Boron-doped p-type Si(111) wafers with a resistivity of 0.8-1.2 Ω•cm (Silicon Resource Company) were evaporated ~ 100 nm Al on the back side and annealed at 800 C for 20 min under forming gas flow to make a p+ layer on the back side for rear contact. Wafers are immersed in buffered HF (Transene) for 30 s to etch away the native silicon oxide before being transferred into the ALD chamber for TiO_2 deposition.

Atomic-layer deposition of TiO_2

TiO_2 deposition was performed using a Savannah ALD system (Cambridge Nanotech). The substrates were heated to 150 °C in a chamber held at a constant pressure of 0.2–0.3 Torr. The precursor, TDMAT (Tetrakis(dimethylamino)titanium, Sigma Aldrich, 99.9999% pure), was heated to 75 °C and was swept into the ALD chamber for 0.1 s using consecutive pulses of N_2 at a flow rate of 20 sccm. The remaining TDMAT was purged from the system for 15 s using nitrogen gas, and then water was pulsed for 0.015 s. Upon completion of ALD, the samples were removed from the chamber and stored under ambient conditions until analyzed. Half of the samples were annealed in air at 400 °C for 1 h in a Thermolyne furnace (Thermo Scientific), and the other half were left as grown.

Deposition of Pt films

2~3 nm of Pt (Kurt J. Lesker, 99.99%) was deposited onto the TiO_2 covered Si substrate in a sputter system (AJA International) with a base pressure of $< 10^{-6}$ torr. Control samples were made to compare stability to the TiO_2/Pt samples by depositing Pt nanoparticles electrolessly onto p-Si electrodes using 1.0 mM H_2PtCl6 in 0.5 M HF (aq) for 2 min, followed by a thorough rinse with H_2O and dried by N_2.

Photoelectrochemistry

The electrodes were fabricated by cutting samples into ~ 0.10 cm^2 pieces, scratching Ga/In eutectic mixture (Aldrich) on the back, and using Ag paint (SPI, Inc.) to mount samples on coiled Cu wires (Consolidated Electronic Wire & Cable). The wire was threaded through a glass tube, and the edges of each sample were covered by Hysol 9460 epoxy to define the active electrode area. Electrode areas were determined by imaging the electrodes on an optical scanner (Epson Perfection V370) and calculated in ImageJ software.

The electrodes were measured by a Bio-Logic SP200 potentiostat-galvanostat, and the data were collected and analyzed using the Bio-Logic EC-Lab software. For measurements of hydrogen evolution, the electrolyte consisting of ~50 mL of 1.0 M H_2SO_4 was

continuously bubbled by H_2 (research grade, AirLiquide) to maintain a constant RHE potential. A saturated calomel electrode (SCE) (0.244 vs. NHE (normal hydrogen electrode), CH Instruments) and a carbon cloth electrode in a fritted glass tube (Porosity D, Ace glass) were used as the reference and counter electrodes, respectively. The electrochemical behavior was measured using cyclic voltammetry (CV) at a scan rate of 50 mV s^{-1} either in the dark or under simulated 1 Sun illumination provided by an ELH lamp. Stability is measured using 100 cycles CV with scan voltage range from open circuit voltage to the voltage where light limit current has been reached.

The measurements in methyl viologen were carried out under continuous purging of Ar. The electrolyte consisted of 0.5 M K_2SO_4 and 50 mM methyl viologen dichloride (MV_2Cl_2, 98%, Sigma-Aldrich), and was buffered at pH = 2.9 using 0.1 M potassium hydrogen phthalate and sulfuric acid. Prior to measurements, after excluding oxygen by purging Ar for 1 hour, MV^+ radical was generated in situ, by scanning CV between -0.6 V and – 0.9 V versus Ag/AgCl reference electrode, until the solution potential reached -0.6 V versus Ag/AgCl, with a carbon rod electrode as a working electrode, and a carbon cloth electrode in a fritted glass tube (Porosity D, Ace glass) as a counter electrode, and a Ag/AgCl (1M KCl, 0.235V vs. NHE, CH Instruments) as a reference electrode. The generated MV^+ radical cation was ~ 3 mM, and made the electrolyte turn deep blue. Photoelectrochemical data was collected at an incident 850 nm light intensity (band width 30 nm) of 60 mW cm^{-2}, with the sample electrode as a working electrode, a carbon rod electrode as a counter electrode, and a small carbon cloth electrode as a reference electrode. The open circuit voltages of the samples were measured using Open Circuit Voltage (OCV) technique for 30 s.

For non-aqueous electrochemical measurement, we investigated the samples in cobaltocenium/cobaltocene, decamethylferrocenium/decamethylferrocene, and ferrocenium/ferrocene, all of which used acetonitrile (CH_3CN, anhydrous, 99.8%, Sigma Aldrich) as solvent and 1.0 M lithium perchlorate ($LiClO_4$, battery grade, 99.99%, Sigma-Aldrich) as supporting electrolyte. For tests in cobaltocenium/cobaltocene, the electrolyte

contains 2 mM cobaltocene ($CoCp_2$, 98%, ACROS Organics), and 80 mM cobaltocenium hexafluorophosphate ($CoCp_2PF_6$, 98%, Sigma-Aldrich. For tests in decamethylferrocenium/decamethylferrocene, the electrolyte contains 5 mM decamethylferrocene ($Me_{10}Fc$, 99%, Alfa Aesar), and 25 mM decamethylferrocenium tetrafluoroborate ($Me_{10}FcBF_4$). For tests in ferrocenium/ferrocene, the electrolyte contains 5 mM ferrocene (Fc, 98%, Sigma-Aldrich), and 25 mM ferrocenium tetrafluoroborate (FcBF4, technical grade, Sigma-Aldrich). Acetonitrile was dried by flowing through a solvent column, and stored in 3Å, activated, molecular sieves (Sigma-Aldrich). $LiClO_4$ was dried by fusing under a pressure < 1×10^{-3} Torr at 300 °C. Other chemicals were purified by vacuum sublimation. The chemicals were all stored in glove box that contained less than 0.2 ppm of oxygen. The electrochemical measurements were carried out in glove box as well. The open circuit voltages of the samples were measured using Open Circuit Voltage (OCV) technique, under simulated 1 Sun illumination provided by an ELH lamp, with the sample electrode as a working electrode, a Pt gauze (52 mesh, 0.1 mm diam., 99.9%, Alfa Aesar) as a counter electrode, and a Pt wire (0.5 mm diam., 99.99%, Sigma-Aldrich) as a reference electrode.

Mott-Schottky analysis

Mott-Schottky analysis was performed on a Bio-Logic SP200 potentiostat-galvanostat, on solid-state devices of p Si/ TiO_2, as grown and annealed. These samples were sputtered ~ 20 nm Ti and ~ 10 nm Pt to make front contact, and scratched InGa at the back side to make back contact. Cu wires were connected to the front and back sides by conductive epoxy. The working electrode clip of the SP200 was connected to the back side of the sample, and the counter electrode clip with the reference electrode clip was connected to the front side of the sample. SPEIS technique was used, with scan range from -0.7 V to 0 V, separated by 14 potential steps. Scan frequencies were from 1 MHz to 10 Hz. Data was collected and analyzed by the Bio-Logic EC-Lab software.

XPS Characterization

XPS characterization was performed on a Kratos AXIS Nova with DLD (Kratos Analytical, Manchester, UK, a Shimadzu Group Company). We used a monochromatic Al Kα line at 1486.6 eV from a source operating at 15 mA and 15 kV. Spectra were acquired at the pressure at low 10^{-9} Torr, with a spot size of 700 μm by 400 μm, pass energy 10 and a step of 50 meV. Sample surfaces were cleaned only by a nitrogen blow-off, and then contacted from the top. We did not apply charge neutralization.

3.2 Results and discussion

ALD provides us an approach to synthesize ultrathin, extremely uniform materials, and also provides an opportunity to manipulate the materials interfaces. ALD TiO_2 has been shown to effectively protect the n-Si,[63] n-GaP[63], n-GaAs[63], n-CdTe[64], p-n^+ Si[59], amouphous Si[57] and GaP[58] surface from corrosion in PEC water splitting cells. We worked on a schematically study of how the thickness of ALD TiO_2 and the annealing would influence with the p-Si for water splitting. We started with ultrathin layers of TiO_2: 20, 40, 80 ALD cycles of TiO_2, and their thickness were ~ 0.8 nm, 1.6 nm and 3.2 nm respectively (ALD TiO_2 growth rate was 0.4 Å/cycle). Then we also extended to the thicker TiO_2 coating, 250 cycles and 500 cycles (~10 nm and 20 nm) of TiO_2. The as-grown TiO_2 has amorphous structure which already been demonstrated hole conductive on n-Si, n-GaAs and n-CdTe for water oxidation when coupled with Ni catalyst in previous reports.[63, 64] It also showed very promising electron conductivity on p-Si, when sputtered Pt was used as catalyst for water reduction (Figure 3.1). Define the V_{oc} as the turn on voltage of the photocurrent vs. RHE, or hydrogen evolution potential in 1.0 M H_2SO_4 with H_2 gas bubbling, all the samples with as-grown ALD TiO_2 exhibited stable V_{oc} (blue lines in Figure 3.1a-e). V_{oc} on the sample of 20 and 40 cycles ALD TiO_2 protection layer had slightly higher V_{oc} (173mV and 263 mV) compared with other thicker ALD TiO_2 protection layer (167 mV, 141 mV and 122 mV on 80 cycles, 250 cycles and 500 cycles of TiO_2 protection layers respectively), which may due to formation of new Si/SiO_x junction on thinner samples during the water splitting. The ALD layer was too thin to completely avoid the oxidation of underneath Si. Then the thicker ALD

TiO_2 protection layer showed relative stable V_{oc}. Considering some potential drop on ALD TiO_2 protection layer, the V_{oc} was irrelative to the thickness of TiO_2. It implied that the as-grown ALD TiO_2 protection layer would not contribute too much on the band bending on the energy structure.

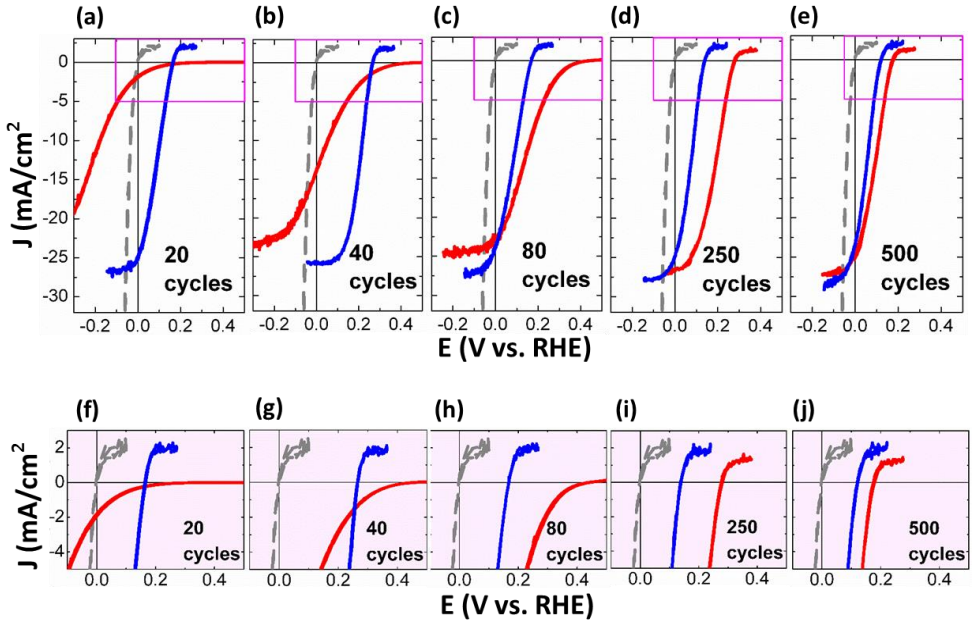

Figure 3.1. *J-V* characterization of the Si/TiO_2/Pt heterojunctions in 1.0 M H_2SO_4 aqueous solution. The *J-V* curves of 20, 40, 80, 250, 500 cycles of ALD TiO_2 on Si/TiO_2/Pt heterojunctions were shown (a)-(e). Zoomed in figures on the onset potential region of (a)-(e) were exhibited in (f)-(j) respectively. Red solid line: Annealed TiO_2 on p Si with sputtered Pt. Blue solid line: As grown TiO_2 on p Si with sputtered Pt. Gray dash line: Pt disk electrode.

Interestingly after annealing 1 hour in air at 400 °C, all the samples had enhanced V_{oc} (Figure 3.1f- 3.1j). The enhancements were too dramatic to be ignored. Figure 3.3 listed detailed V_{oc} improvements of each condition after annealing. The V_{oc} can be achieved as high as 481 mV on p-Si with 40 cycles ALD TiO_2 layer after annealing, which was

comparable to the record of 520 mV obtained on the similar structure of p-n^+ Si/TiO_2/Pt. Large V_{oc} of 440 and 456 mV were also observed on p-Si with 20 cycles and 80 cycles of ALD TiO_2. However, this effect seemed diminished on the thicker TiO_2 samples. *V*oc of 250 cycles (10 nm) ALD TiO_2 sample will decrease to 280 mV, while the 500 cycles (20 nm) one has only 60 mV difference with the as-grown TiO_2 samples (182 mV vs. 122 mV). The ALD TiO_2 surface does not change the roughness, which was approved by AFM (Figure 3.2). Thus it excluded the possibility of annealed ALD TiO_2 forming micro-size grains during annealing, exposing p-Si into the solution, and therefore may result in a higher V_{oc}.

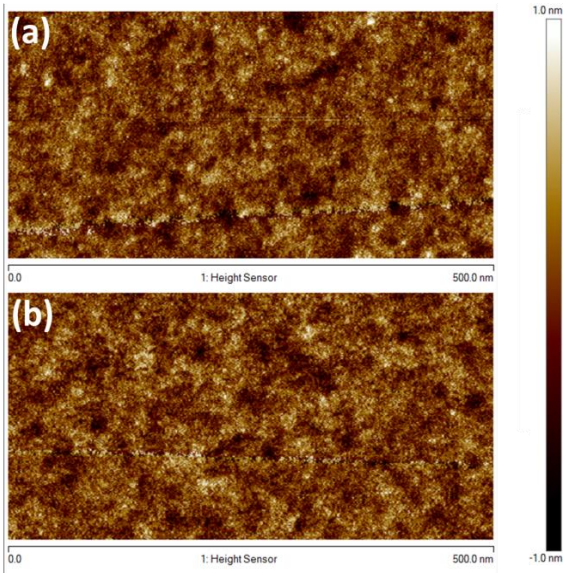

Figure 3.2 AFM images for the Si/TiO_2 heterojunctions before (a) and after (b) annealing

Possibly during annealing, O_2 from the air would diffuse though TiO_2, and immigrate into Si layer and then form a mixture of Si-O-Ti layer. This special Si-O-Ti layer had been observed in similar Si/ALD TiO_2 structure after annealing.[65] The heterojunction of p-Si/[Si-O-Ti] layer contributed to the enlarged V_{oc} in this case. It was also proved by the different photocurrent slopes on the annealed samples (Figure 3.1f-1h).Thinner samples showed that decreasing slope after annealing may be due to the formation of significant amount SiO_x, which was known as a high-resistor material. However, the thicker samples (250 cycles and 500 cycles) have comparable slope with as-grown samples, indicating that

the newly formed Si-O-Ti layer had good electron conductivity for water reduction. The abridged anodic currents of these annealed thin TiO_2 samples indicated that the hole conductivity of these Si-O-Ti layers may not be good enough to complete water oxidation. This was consistent with the results of the previous report.[63, 66]

Moreover, this Si-O-Ti was different from the other non-controlled SiO_x layer on the electronic property. By heating bare p-Si without ALD TiO_2 in air under same annealing condition, a SiO_x layer was intentionally fabricated onto p-Si. With the same amount of Pt sputtered onto this p-Si/SiO_x, the sample was not photoreactive until over -1.0 V (vs. SCE) bias was applied in 1.0 M H_2SO_4 solution. If we calculate the water splitting efficiency by the following equation,

$$\eta = \frac{V_{oc} \times J_{sc} \times FF}{100\ mW/cm^2} \times 100\% \qquad (3.1)$$

where V_{oc} is the open circuit voltage, J_{sc} is the short circuit current, and FF is the fill factor (Figure 3.3b), then the trend of how the efficiency increases with the influence of TiO_2 thickness on annealed sample would be more obvious (Figure 3.4).

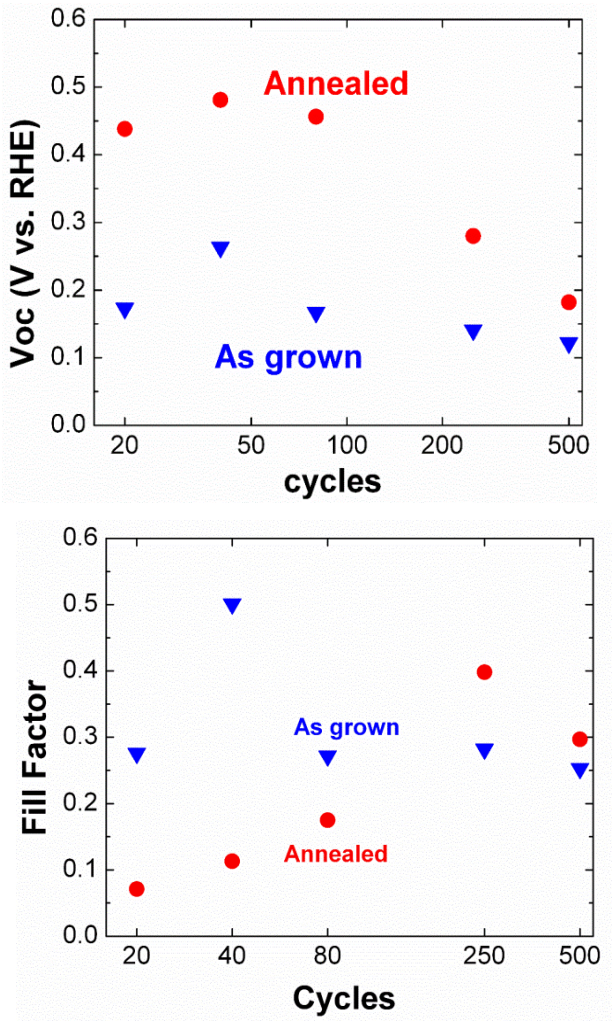

Figure 3.3. a) V_{oc} of the Si/TiO_2/Pt heterojunctions in 1.0 M H_2SO_4 aqueous solution. The investigated samples had 20, 40, 80, 250, 500 cycles of ALD TiO_2 between p-Si and sputtered Pt. b) Fill Factor of the Si/TiO_2/Pt heterostructures.

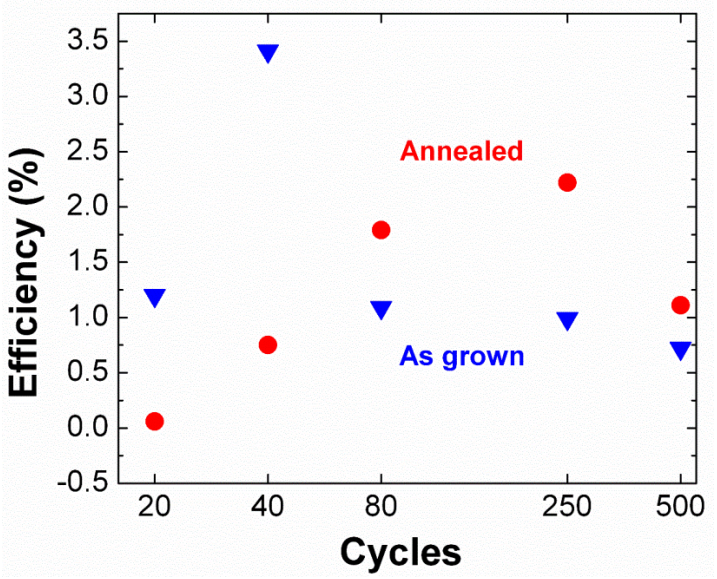

Figure 3.4. Efficiency of the Si/TiO_2/Pt heterostructures.

The efficiency obviously improved after annealing on the samples with greater than 80 cycles of ALD TiO_2 layer. It implied the minimum thickness of TiO_2 to protect Si during annealing process. Significant amount of V_{oc} improvement of the annealed sample contributes to the higher efficiency, with optimized thickness of 250 cycles with a high *FF*. The improvement on thicker samples may be also due to the formation of buried junction on p-Si/ annealed TiO_2 surface. But this buried junction would be different from the thinner sample since the TiO_2 layer was thick enough for O_2 to penetrate through during annealing and create the unique Si-O-Ti layers. Therefore, the photovoltage enhancement was different from the thinner samples.

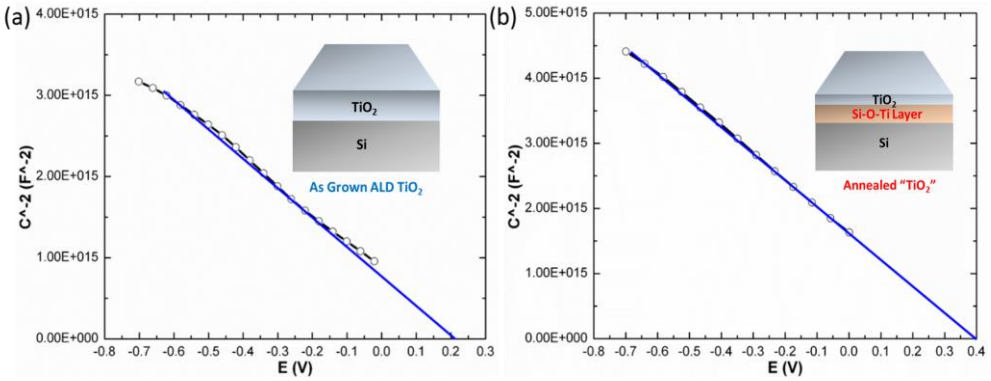

Figure 3.5. Mott-Schottky plots for (a) as grown and (b) annealed p Si/250 cycles TiO_2.

To study the interface energetics, we performed solid-state Mott-Schottky analysis on p Si/TiO_2 samples with 250 cycles TiO_2, as grown and annealed:

$$C_{SC}^{-2} = 2(V - V_{fb} - \frac{kT}{e})/N_D \varepsilon \varepsilon_0 e A^2 \qquad (3.2)$$

where N_D is the doping density, ε is the relative dielectric constant of semiconductor, ε_0 is the permittivity of the vacuum, e is the charge of an electron, A is the electrode surface, k is the Boltzmann constant, T is the temperature, and V_{fb} is the flat band potential at the semiconductor/electrolyte interface. The intercepts of the linear extrapolation in the Mott-Schottky plots indicate flat band potential V_{fb}, which were 0.21 V and 0.40 V for the as grown samples and annealed ones, respectively. The V_{fb} of the annealed samples showed a significant positive shift, which implied greater band bending on the annealed samples and was in agreement with the improvement of V_{oc}.

In order to further verify the V_{oc} enhancement after annealing, the p-Si/TiO_2 junctions were also investigated in methyl viologen (MV) aqueous solution and $CoCp_2$ solution. MV solution was reduced at -0.60 V vs Ag/AgCl reference under Ar (g) protection.[31, 67] The light source was a LED lamp illumination wavelength centered at 850 nm. The p-Si/TiO_2 was measured in three electrode cell with a small carbon cloth as a reference electrode and

a carbon rod counter electrode. The V_{oc} obtained (Figure 3.5a) on varied thickness of as grown ALD TiO_2 show similar trend of the corresponding ones in 1.0 M H_2SO_4 (Figure 3.4). The only difference was that the 20 cycles of as grown TiO_2 on p-Si had higher V_{oc} than the corresponding one in 1.0 M H_2SO_4. It was because in such a reactive solution, oxidation of the Si rarely happened since $MV^{\bullet+}$ was reactive and much easier to be oxidized,[67] and the TiO_2 layer was too thin to influence the depletion region of Si and the chemical potential of the solution. With increased thickness of TiO_2, the additional energy level was formed, which made electrons an intermedia energy station with lower energy level and therefore lowered the V_{oc}. After annealing, all the samples had enhanced V_{oc}, indicating that the assumption of the new formed buried junction between p-Si and Si-O-Ti mixture. The maximum V_{oc} obtained was 517 mV on 40 cycles of annealed ALD TiO_2, which was close to the result of 510 mV on homogenous junction p-n+ Si/TiO_2 in fast redox pair solution. It meant that the quality of this new formed buried junction was as good as the rationally designed homogenous junctions.

Cobaltocenium/cobaltocene/ ($CoCp_2^{+/0}$) was another commonly used redox pair to characterize the p-Si. The chemical potential of $CoCp_2^{+/0}$ system processed around -0.90 V vs SCE, negative enough to form a large band bending contacting with p-Si.[68] A very similar trend of the V_{oc} on the samples of as-grown ALD TiO_2 on p-Si and annealed ones is displayed in Figure 3.5b. Also the generally higher V_{oc} in $CoCp_2^{+/0}$ solution than the one in methyl viologen was due to the more negative chemical potential of $CoCp_2^{+/0}$, resulting in a larger band bending on p-Si.

To see how our samples behave in redox solutions with more positive potential, we further characterized them in decamethylferrecenium/decamethylferrocene and ferrocenium/ferrocene. The $Me_{10}Fc^{+/0}$ cell has a potential of -0.039 V vs. SCE, and bare p-Si only has a V_{oc} around 50 mV. The $Fc^{+/0}$ cell has a potential of +0.481 V vs. SCE, and bare p-Si has ohmic contact with the solution, resulting in a V_{oc} of 0 V. However, our samples showed much higher V_{oc} compared to bare p-Si (Figure 3.6), which means the TiO_2 layer

makes the Si/TiO_2 junction less influenced by the outside electrolyte, and achieved higher Voc.

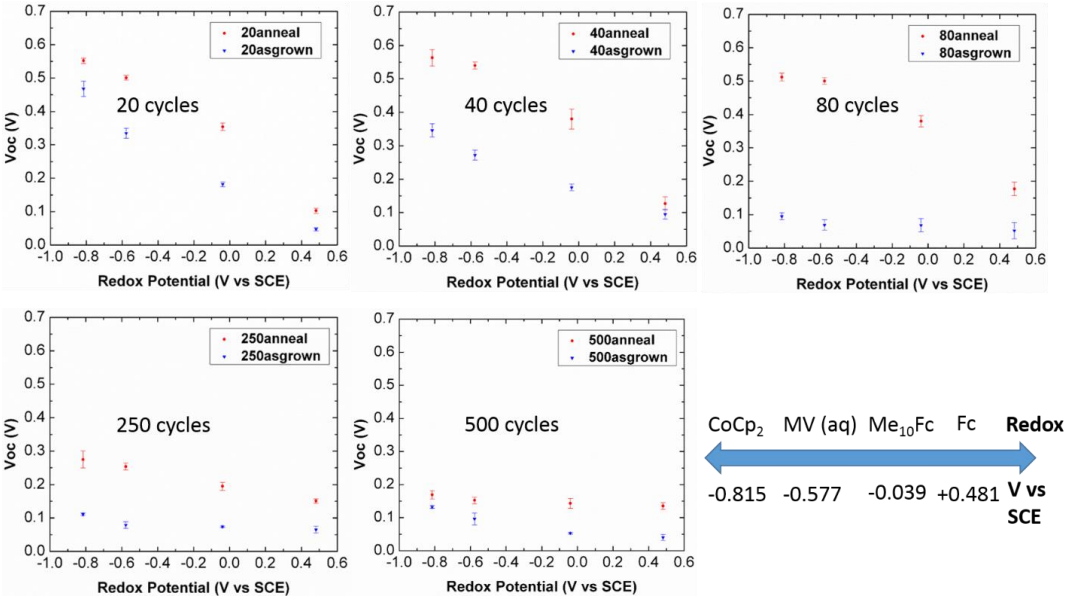

Figure 3.6 V_{oc} of the Si/TiO_2 heterojunctions in different redox couple solutions. The investigated samples had 20, 40, 80, 250, and 500 cycles of ALD TiO_2 on p-Si. The redox couple solutions and their corresponding cell potentials are listed in the bottom right of the figure.

Together with the evidences in fast redox pair solutions, XPS was also used to investigate the unique Si-O-Ti formation of the Si/TiO_2 structures before and after annealing.

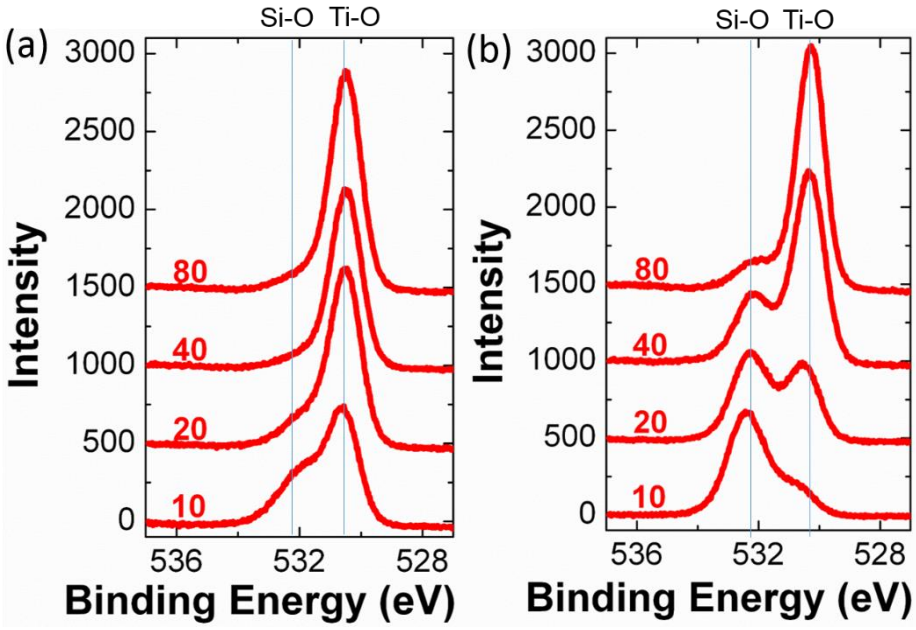

Figure 3.7 XPS spectra of O 1s for the Si/TiO_2 heterojunctions, a) as grown samples; b) annealed samples.

Figure 3.7 showed the changes in O1s XPS spectrum after annealing. In the as grown Si/TiO_2 structures, only the 10 cycle TiO_2 sample showed obvious Si-O bonding. This could be interpreted as SiO_x formation during ALD process. However, after annealing, all the 10 to 80 cycle TiO_2 samples showed Si-O bonding with different intensities. Also it is important to notice that in the annealed samples, as the thickness of TiO_2 increases, the Si-O peak shifted toward the Ti-O peak side, and the Ti-O peak shifted toward the Si-O peak side. This implies that the Si-O bonds and the the Ti-O bonds are influenced by each other, indicating a possible Si-O-Ti mixture.[69]

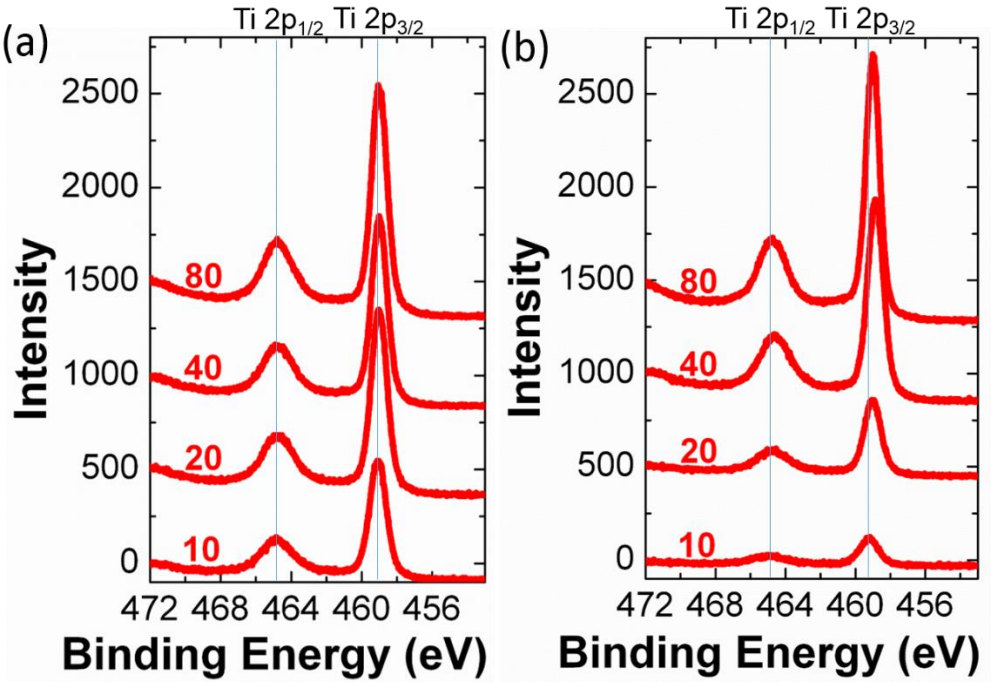

Figure 3.8 XPS spectura of Ti 2p for the Si/TiO_2 heterojunctions, a) as grown samples; b) annealed samples.

The Ti 2p XPS spectrum in Figure 3.8 also showed the similar evidence. In the as grown samples, there were no obvious shifts in the Ti 2p peaks. Oppositely, we clearly saw Ti 2p peak shifts in the annealed ones. The Ti 2p peaks in 20, 40, and 80 cycle annealed Si/TiO_2 samples all shifted toward a lower binding energy compared to the 10 cycle one. The shift for the 40 cycle one is the largest among the three. This agrees with the electrochemical test that the 40 cycle annealed TiO_2 sample had the highest V_{oc} in hydrogen evolution.

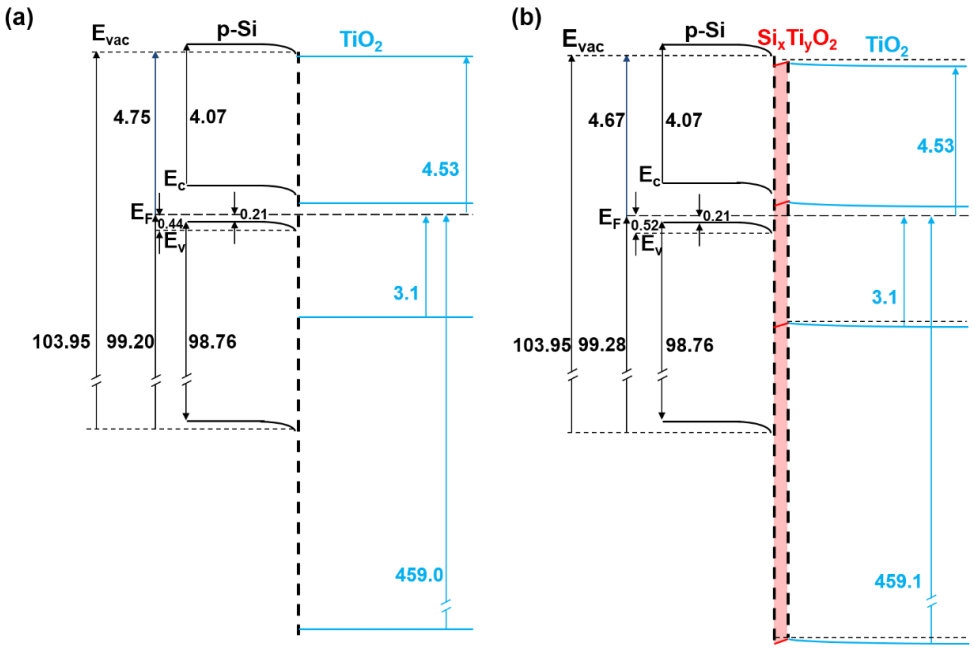

Figure 3.9 Band diagram of the Si/TiO_2 heterojunctions, a) as grown samples; b) annealed samples.

From the XPS spectrum and some other data in literature such as the electron affinity, we can build the energy band diagrams by Kraut's method.[70-73] The binding energies in XPS are measured with reference to the Fermi energy of the spectrometer. The Fermi level of the sample is aligned with the Fermi energy of the spectrometer since the sample is in electronic equilibrium with the sample holder. Thus the positions of the band edges can be determined by the binding energies in XPS. The valance band maximum (VBM) is determined by the linear extrapolation in the VB spectrum in XPS. The Ti 2p core level band edge is determined by the Ti $2p_{3/2}$ peak. As the Ti 2p peaks in annealed samples shift lower from 10 to 40 cycles, and then shift a little bit higher from 40 to 80 cycles, we can see that the bands in TiO_2 first bend upward and then bend downward, with 40 cycles at the turning point. This diagram shows the uniqueness of the 40 cycles annealed TiO_2. The upward bending part is assumed to be the Si-O-Ti interfacial layer.

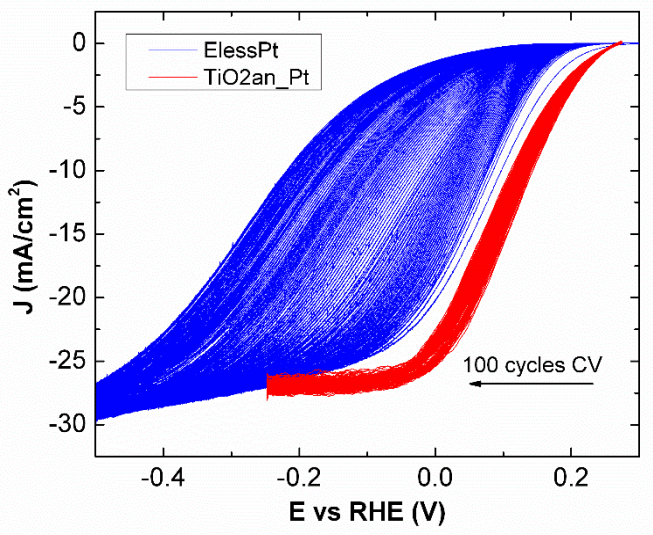

Figure 3.10 100 cycles CV of p-Si/250 TiO_2an/Pt and p-Si/Eless-Pt

To show that the TiO_2 layer enhances the stability of p-Si, we compare 100 cycles CV scan of the p-Si electrode coated with 250 cycles annealed TiO_2/sputtered Pt with the electroless deposited Pt electrode. The p-Si/Eless-Pt electrode degraded rapidly during the CV scan. Oppositely, the 100th cycle CV of p-Si/250 TiO_2(a)/Pt electrode stayed very similar to the 1st cycle, which showed a better stability. To find out what caused the difference, we performed XPS on the two fresh samples and two samples after 100 cycles CV scan. XPS results (Figure 3.11) showed that after the CV scan, the p-Si/Eless-Pt sample was oxidized significantly more than the p-Si/TiO_2/Pt sample. We can conclude that with the TiO_2 layer, the p-Si electrode is more stable than the one without TiO_2.

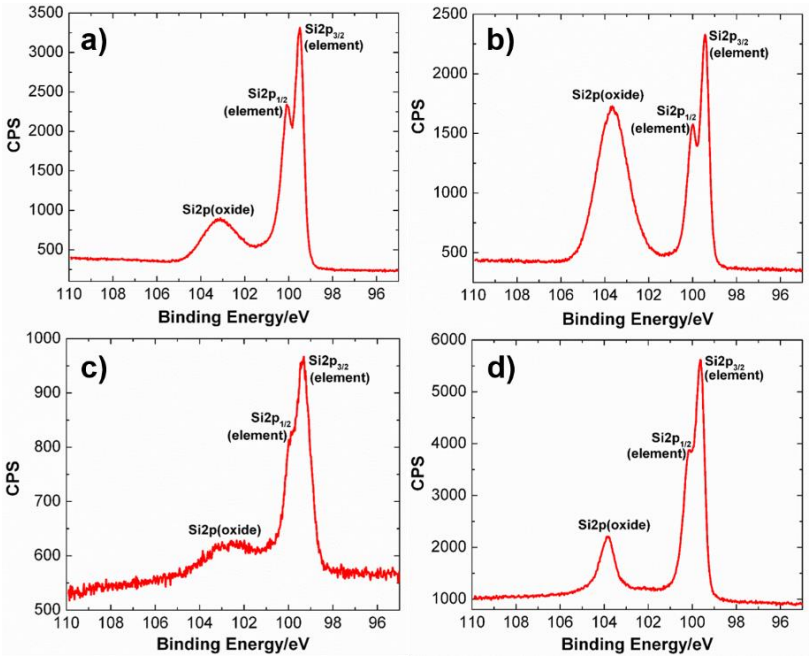

Figure 3.11 XPS of Si 2p peaks of (a) fresh p-Si/Eless-Pt (b) p-Si/Eless-Pt after 100 cycles CV (c) fresh p-Si/TiO_2an/Pt (d) p-Si/250TiO_2an/Pt after 100 cycles CV

3.3 Conclusion

In conclusion, we passivated p-Si by employing the ALD TiO_2, and utilize this system for water splitting test as photocathode. In this system, water reduction photovoltage close to 500 mV on this Si/TiO_2/Pt heterojunctions was obtained after annealing, and the optimal performance was obtained on the annealed sample of 250 cycles TiO_2 on p-Si with a V_{oc} of 280 mV and water splitting efficiency of 2.22%. The V_{oc} improvement was also approved by Mott-Schottky plot and can be explained by the formation of the unique Si-O-Ti mixture layer. The new junction of p-Si/[Si-O-Ti] mixture layer was also investigated in aqueous and non-aqueous redox couple solutions and XPS. The complete energetic band diagram was completed by using XPS results for this system, which provide an in-depth understanding of this system. The TiO_2 layer also enhances the stability of p-Si electrode.

Chapter 4

CORROSION STUDY OF CDTE ELECTRODES FOR HYDROGEN EVOLUTION REACTION IN ACID AND BASE

Content in this chapter is drawn from the following publication:

Jiang, J., Moreno-Hernandez, I., Buabthong, P., Papadantonakis, K. M., Brunschwig, B. S., Lewis, N. S. Chemical and Electrochemical Corrosion Study of CdTe Electrodes for the Hydrogen Evolution Reaction in Acid and Base. (In preparation)

Jiang, J. participated in the conception of the project, prepared samples, conducted electrochemical measurements and collected solution samples for ICP-MS, analyzed data, and participated in the writing and revision of the manuscript.

4.1 Experimental

Materials:

n-CdTe(111) wafers with a carrier concentration 5.5 x 10^{17} cm^{-3} were purchased from JX Nippon Minging and Metals Corporation. All the other chemicals were used as received, including sulfuric acid (H_2SO_4, BDH ARISTAR® ULTRA, 93-98%, ultrapure for trace metal analysis), potassium hydroxide (KOH, Acros Organics, 99.98%, trace metal basis), bromine (Br_2, Sigma-Aldrich, ≥99.99% trace metals basis), methanol (CH_3OH, ≥99.8% ACS, VWR Chemicals), and hydrogen peroxide solution (H_2O_2, 30 % w/w in H_2O, Sigma-Aldrich). Deionized H_2O with a resistivity of ≥18 MΩ·cm was obtained from a Barnstead Nanopure station (Thermo Scientific). A platinum target (Pt, Kurt J Lesker, 99.99%) was used in Pt deposition.

Electrode Preparation:

CdTe pieces were cut from an n-CdTe(111) wafer that had been polished in factory. Then the back was soldered with In to make electrical contact. Pieces were etched for 30 s in a freshly prepared solution of 0.2%(v/v) Br_2 /CH_3OH, then rinsed vigorously with CH_3OH and dried with N_2, followed by 15 seconds exposure in 30 wt.% H_2O_2, then rinsed vigorously with water and dried with N_2, and immersed in CH_3OH until being dried with a stream of N_2(g) before use. Pt deposition was performed in a sputterer (AJA International) with a base pressure of $< 10^{-6}$ torr under an Ar atmosphere at 5 mTorr using RF power. ~2 nm of Pt was deposited onto the front side of the prepared CdTe substrate.

The samples are scratched with Ga-In eutectic (Sigma Aldrich, 99.99%) onto the back, followed by use of Ag paint (SPI Supplies) to attach to a Cu wire (McMaster-Carr). The wire was threaded through a glass tube (Corning Incorporation, Pyrex tubing, 7740 glass). The area around the wire and the sample was coated with non-conductive epoxy (Hysol 9460) and allowed to dry overnight. Electrode areas were imaged using a high-resolution optical scanner (Epson perfection V370 with a resolution of 2400 psi) and then analyzed by ImageJ software.

Electrochemical measurements:

Electrochemical measurements were conducted in a home-made dark box in a custom two-compartment electrochemical cell with a membrane separating the working electrode (with the reference electrode) from the counter electrode. A Nafion membrane is used for measurements in 1.0 M H_2SO_4(aq) and an anion exchange membrane (AEM) is used for measurements in 1.0 M KOH(aq). Each compartment contains 25 mL electrolyte which was filled by a pipette (Fisher Scientific, 5mL). The electrochemical cell was cleaned with aqua regia, rinsed thoroughly with H_2O, dried in an oven, and cooled in air before use.

A carbon rod (Alfa Aesar, ≥99.9995%, metals basis) placed in a fritted glass tube (Aceglass Inc., gas dispersion tube Pro-D) was used as the counter electrode. A mercury/mercurous

sulfate ($Hg/HgSO_4$ in saturated K_2SO_4(aq), CH Instruments, CH151) electrode and a mercury/mercury oxide (Hg/HgO in 1.0 M KOH(aq), CH Instruments, CH152) electrode were used as the reference electrode in 1.0 M H_2SO_4(aq) and in 1.0 M KOH(aq) respectively.

All the electrochemical data was collected on a MPG-2 multichannel potentiostat or a SP-200 potentiostat (BioLogic Science Instruments). Prior to the measurements, the electrolyte was purged with H_2(g) for 30 min to saturate H_2(g) and remove O_2(g). During the measurements, H_2(g) bubbling was maintained to keep a saturated H_2(g) and O_2(g)-free environment. Vigorous stirring was kept before and during the measurements since the H_2(g) purge started, using a magnetic stir bar driven by a model-train motor (Pittman). Chronoamperometric (CA) measurements were performed at a constant potential at -100 mV vs. reversible hydrogen electrode (RHE). Open Circuit Voltage (OCV) measurements were performed with no potential applied to the working electrode. Each electrochemical experiment was run for 24 hours. At 0, 1, 2, 4, 8, and 24 hours of each experiment, 1 mL solution was taken out from the working compartment by a pipette (Fisher Scientific, 1000μL) for further analysis by ICP-MS. The sample taken at 0 hour is after a 30 min purge of H_2(g) and right before the working electrode was put into the cell. After the samples were taken out, no solution was added to the compartment.

Inductively-coupled plasma mass spectrometry (ICP-MS) analysis:

Inductively coupled plasma mass spectrometry (ICP-MS) data were collected on an Agilent 8800 Triple Quadrupole ICP-MS system. Calibration solutions were prepared by diluting the multi-element standard solutions with deionized water. The solution samples were collected from the electrochemical experiments. Acidic samples were diluted from 1 mL to 5 mL using the deionized water, and alkaline samples were diluted from 1 mL to 5 mL with 2 mL 1.0 M H_2SO_4(aq) and 2 mL H_2O to make it acidic and appropriate for ICP-MS. The total amount of the dissolved Cd and Te species respectively in the working compartment at different hours can be calculated by the ICP-MS results with the adjustment of volumes being taken into account. Then this amount was normalized to the geometric electrode area for comparison and can be used to calculate the corrosion rate in thicknesses. The faradaic

efficiencies of the cathodic corrosion can be calculated by dividing the charges transferred in the corrosion process by the total charges passed in the electrochemical experiment.

Scanning-electron microscopy (SEM)

Scanning-electron microscopy (SEM) were performed using a FEI Nova NanoSEM 450 at an accelerating voltage of 5 kV with a working distance of 5 mm.

X-ray photoelectron spectroscopy (XPS)

X-ray photoelectron spectroscopy (XPS) data were collected using a Kratos Axis Nova system with a base pressure of $< 2\times10^{-9}$ Torr. A monochromatic Al Kα source was used to irradiate the sample with X-rays with an energy of 1486.7 eV at a power of 450 W. A hemispherical analyzer oriented for detection along the sample surface normal was used for maximum depth sensitivity. High-resolution spectra were acquired at a resolution of 50 meV with a pass energy of 10 eV.

4.2 Results

Electrochemical stability of n-CdTe

Figure 4.1 shows the chronoamperometry profiles of n-CdTe electrodes biased at -100 mV vs. RHE in H_2(g)-saturated 1.0 M H_2SO_4(aq) and 1.0 M KOH(aq) in the dark. An increasing current density over time was observed in 1.0 M H_2SO_4(aq), while a relatively stable current density was reached in 1.0 M KOH(aq) after 15 hours. The current densities start in the magnitude of $\mu A/cm^2$ and get to around -0.01 mA/cm^2 at 24 hours. Both chronoamperometry curves are smooth in the first ~ 7 hours, and then gradually become noisy in the following hours.

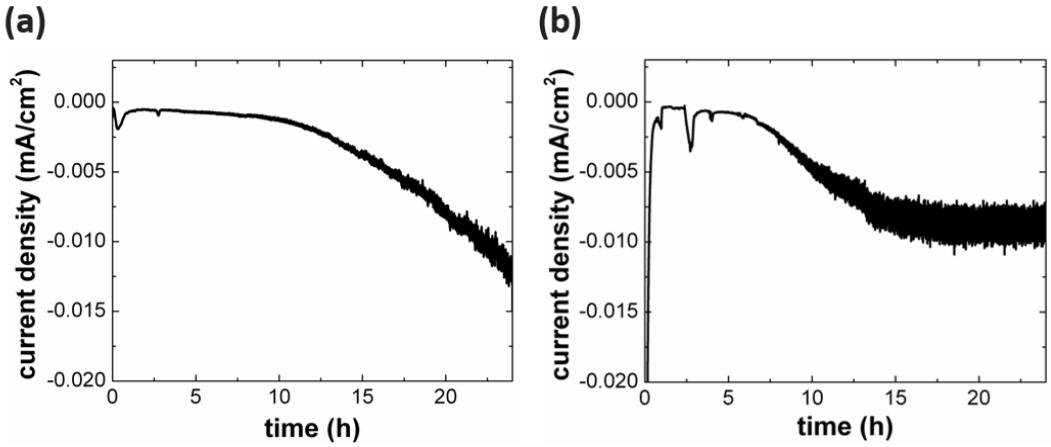

Figure 4.1. Chronoamperometry (current density vs. time) for the n-CdTe electrodes (dark) biased at -100 mV vs. RHE over 24 hours in H_2(g)-saturated (a) 1.0 M H_2SO_4(aq); (b) 1.0 M KOH(aq).

Figure 4.2 shows the concentrations and amount of dissolved Cd and Te species of n-CdTe electrodes in the dark biased at -100 mV vs RHE in H_2(g)-saturated 1.0 M H_2SO_4(aq) (Figure 4.2a and 4.2c) and 1.0 M KOH(aq) (Figure 4.2b and 4.2d) over 24 hours. The concentrations and amount of dissolved Cd and Te species are normalized to 1 cm^2 n-CdTe electrode area, and the concentrations are adjusted to a 25 mL volume. The corrosion thickness in Figure 4.2a and 4.2b is calculated from the amount of dissolved Te species (in μmol, Figure 4.2c and 4.2d) and the density of CdTe to have a more straightforward idea of how fast or slow the semiconductor is leaching. From the comparison of Figure 4.2a and 4.2b, as well as the comparison of Figure 4.2c and 4.2d, the dissolved concentrations of Cd and Te in 1.0 M H_2SO_4(aq) are higher than in the 1.0 M KOH(aq). The concentrations of dissolved Cd species were ~60 μg/L in 1.0 M H_2SO_4(aq) and ~15 μg/L in 1.0 M KOH(aq) at 1 hour, and reached ~135 μg/L in 1.0 M H_2SO_4(aq) and ~40 μg/L in 1.0 M KOH(aq) at 24 hours. The concentration of dissolved Te species reached ~ 180 μg/L in 1.0 M H_2SO_4(aq) and ~60 μg/L in 1.0 M KOH(aq) at 1 hour, and did not change much afterwards. While the concentration of dissolved Cd species in 1.0 M H_2SO_4(aq) showed a slow increasing trend, the concentration trend of dissolved Te species was pretty flat in 1.0 M H_2SO_4(aq) after 1 hour, if we take into the error bars into account. However, the corrosion rate of Cd slowed down

over time, as we could see that the differential of the concentration curve of Cd in 1.0 M H_2SO_4(aq) becomes smaller gradually. In 1.0 M KOH(aq), Cd and Te had a similar trend as in 1.0 M H_2SO_4(aq), but with a lower dissolved concentration in general. The corrosion rates in thickness were about 0.33 nm/h in 1.0 M H_2SO_4(aq), and about 0.10 nm/h in 1.0 M KOH(aq), respectively.

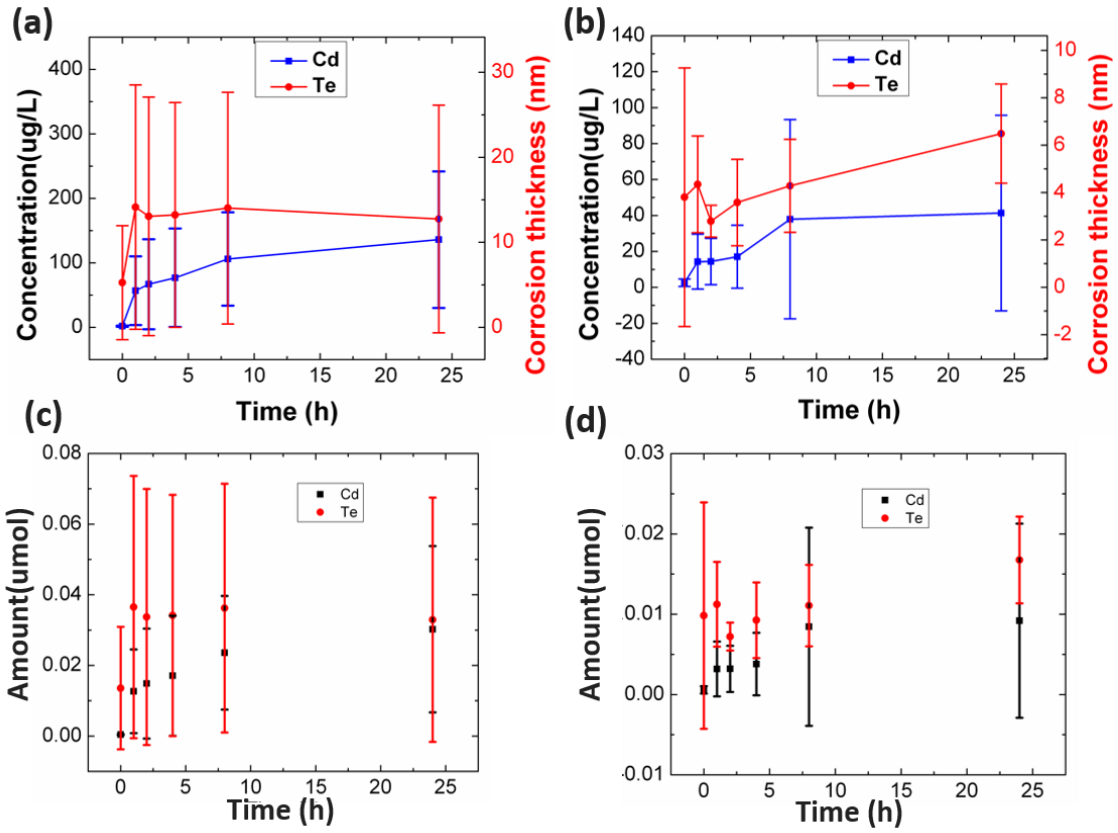

Figure 4.2. (a-b) Concentrations of dissolved Cd, Te species in the working compartment biased at -100 mV vs. RHE in the dark over 24 hours, normalized to 1 cm^2 n-CdTe electrode area and adjusted to 25 mL volume, in H_2(g)-saturated (a) 1.0 M H_2SO_4(aq); (b) 1.0 M KOH(aq). (c-d) total amounts of dissolved Cd, Te species in the working compartment biased at -100 mV vs. RHE in the dark over 24 hours, normalized to 1 cm^2 n-CdTe electrode area, in H_2(g)-saturated (c) 1.0 M H_2SO_4(aq); (d) 1.0 M KOH(aq).

Figure 4.3 shows the SEM images of the n-CdTe electrodes before any test (Figure 4.3a) and after the chronoamperometry test in H_2(g)-saturated 1.0 M H_2SO_4(aq) (Figure 4.3b) and 1.0 M KOH(aq) (Figure 4.3c) after 24 hours. Before the test, the n-CdTe electrode had a smooth surface. After being tested for 24 hours, the n-CdTe showed some pits and bumps. The n-CdTe electrode tested in 1.0 M H_2SO_4(aq) showed more pits than the one tested in 1.0 M KOH(aq). But both surfaces did not show huge corrosion holes or bumps.

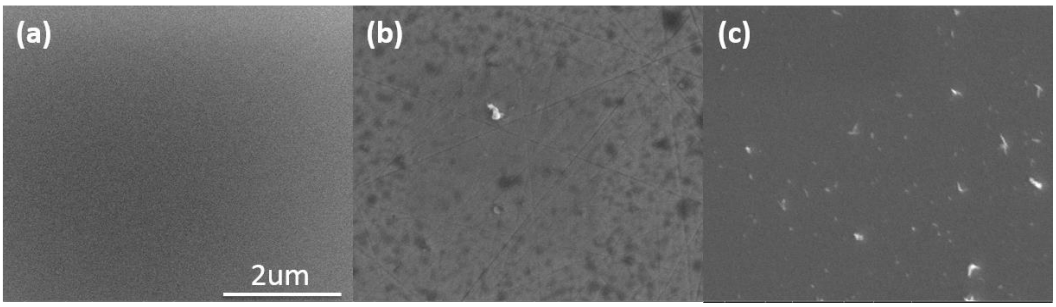

Figure 4.3. SEM images of n-CdTe electrodes (a) before test; (b) after the chronoamperometry test biased at -100 mV vs. RHE in the dark over 24 hours in H_2(g)-saturated 1.0 M H_2SO_4(aq); (c) after the chronoamperometry test biased at -100 mV vs. RHE in the dark over 24 hours in H_2(g)-saturated 1.0 M KOH(aq).

Chemical stability of n-CdTe

Figure 4.4 shows the concentrations and amount of dissolved Cd and Te species of n-CdTe electrodes in the dark with no biased applied in open circuit in H_2(g)-saturated 1.0 M H_2SO_4(aq) (Figure 4.4a and 4.4c) and 1.0 M KOH(aq) (Figure 4.4b and 4.4d) over 24 hours. Like in the study of electrochemical stability of n-CdTe, the concentrations and amount of dissolved Cd and Te species are normalized to 1 cm^2 n-CdTe electrode area, and the concentrations are adjusted to a 25 mL volume. The corrosion thickness in Figure 4.4a and 4.4b is calculated from the amount of dissolved Te species (in μmol, Figure 4.4c and 4.4d) and the density of CdTe. Comparing Figure 4.4a with Figure 4.4b, and comparing Figure 4.4c with 4.4d, we could see that under no bias, the dissolved concentrations of Cd in 1.0 M

H_2SO_4(aq) are higher than in the 1.0 M KOH(aq), but the dissolved concentrations of Te in 1.0 M H_2SO_4(aq) are lower than in the 1.0 M KOH(aq), which is different from the electrochemical case when biased at -100 mV vs. RHE. The concentrations of dissolved Cd species were ~60 μg/L in 1.0 M H_2SO_4(aq) and ~10 μg/L in 1.0 M KOH(aq) at 1 hour, and reached ~90 μg/L in 1.0 M H_2SO_4(aq) and ~10 μg/L in 1.0 M KOH(aq) at 24 hours. The concentrations of dissolved Te species were ~ 150 μg/L in 1.0 M H_2SO_4(aq) and ~370 μg/L in 1.0 M KOH(aq) at 1 hour, and reached ~250 μg/L in 1.0 M H_2SO_4(aq) and ~460 μg/L in 1.0 M KOH(aq) at 24 hours. While when biased at -100 mV vs. RHE, the concentration of dissolved Cd species showed a slow increasing trend, and the concentration of dissolved Te species remained pretty flat after 1 hour in both 1.0 M H_2SO_4(aq) and 1.0 M KOH(aq), when at open circuit voltage, the concentration of dissolved Cd firstly increased, and then arrived at a flat area, and the concentration of Te showed an increasing trend in 1.0 M H_2SO_4(aq) with a slowed down leaching rate over time, and the concentration of Te in 1.0 M KOH(aq) became relatively stable after 4 hours. The corrosion rates in thickness were about 0.50 nm/h in 1.0 M H_2SO_4(aq), and about 1.25 nm/h in 1.0 M KOH(aq), respectively.

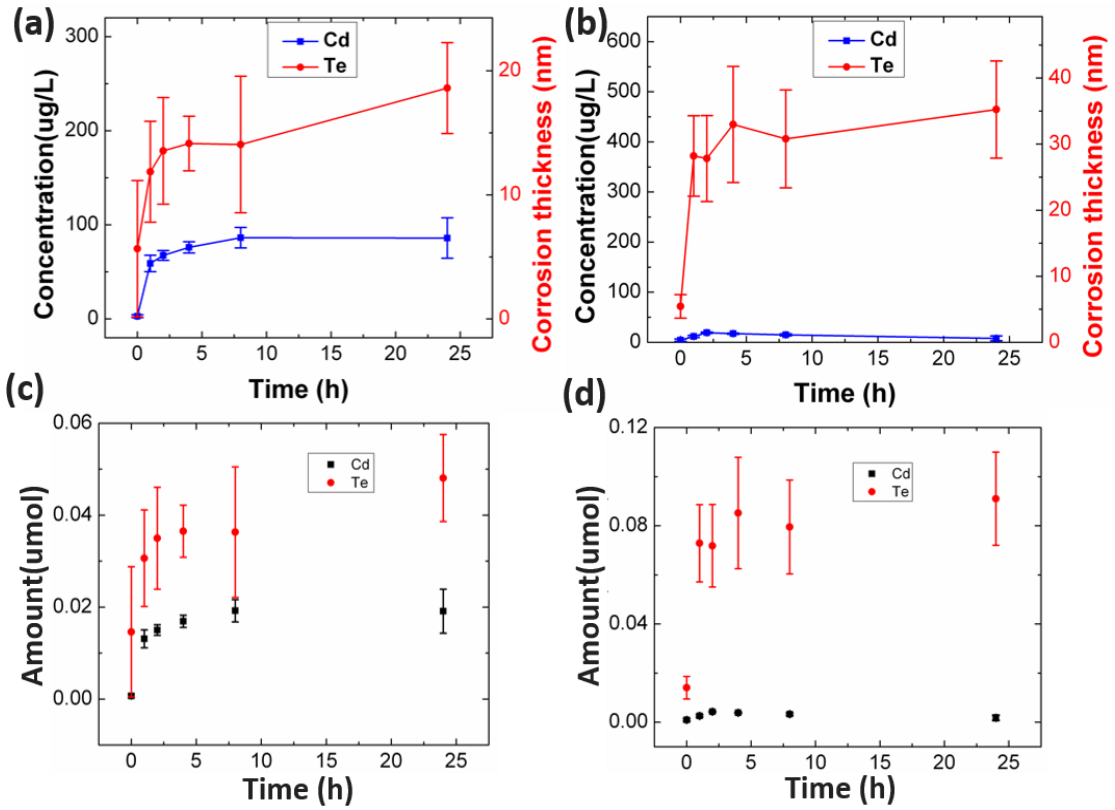

Figure 4.4. (a-b) Concentrations of dissolved Cd, Te species in the working compartment at open circuit voltage (OCV) in the dark over 24 hours, normalized to 1 cm^2 n-CdTe electrode area and adjusted to 25 mL volume, in H_2(g)-saturated (a) 1.0 M H_2SO_4(aq); (b) 1.0 M KOH(aq). (c-d) total amounts of dissolved Cd, Te species in the working compartment at open circuit voltage in the dark over 24 hours, normalized to 1 cm^2 n-CdTe electrode area, in H_2(g)-saturated (c) 1.0 M H_2SO_4(aq); (d) 1.0 M KOH(aq).

Figure 4.5 shows the SEM images of the n-CdTe electrodes after the OCV test in H_2(g)-saturated 1.0 M H_2SO_4(aq) (Figure 5a) and 1.0 M KOH(aq) (Figure 5b) after 24 hours. After being left in the electrolyte at open circuit voltage for 24 hours, the n-CdTe electrode tested in 1.0 M H_2SO_4(aq) showed some non-uniformity, and the n-CdTe tested in 1.0 M KOH(aq) showed a much rougher surface.

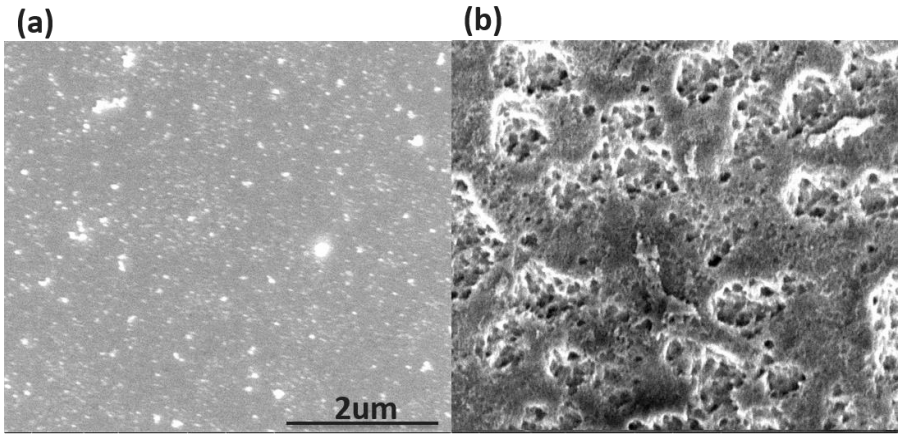

Figure 4.5. SEM images of n-CdTe electrodes after being left at open circuit voltage in the dark for 24 hours in in H_2(g)-saturated (a) 1.0 M H_2SO_4(aq); (b) 1.0 M KOH(aq).

Surface composition of n-CdTe after chemical and electrochemical corrosion

Figure 4.6 shows the Cd (Figure 4.6a) and Te (Figure 4.6b) XPS peaks of n-CdTe electrodes (dark) before and after 24-hour electrochemical tests. Before test, n-CdTe showed an elemental Te 3d 5/2 component at 572.8 eV, an elemental Te 3d 3/2 component at 583.1 eV, and a 3d 5/2 peak at 576.1 eV and a 3d 3/2 peak at 586.5 eV corresponding to TeO_2. After being left at open circuit voltage (chemical corrosion) in 1.0 M H_2SO_4(aq), the TeO_2 peaks are gone, with only the elemental Te peaks remained. After being biased at -100 mV vs. RHE (electrochemical corrosion) in 1.0 M H_2SO_4(aq), there are still TeO_2 peaks but they became very small, and the other Te peaks are Te^0 as before test. In 1.0 M KOH(aq), the TeO_2 peaks remained either after 24-hour chemical corrosion or electrochemical corrosion. However, new peaks at 572.2 eV corresponding to Te^{2-} arose, in both conditions. Besides the TeO_2 peaks, the n-CdTe after chemical corrosion in 1.0 M KOH(aq) had a Te 3d 5/2 peak at 572.5 eV and a Te 3d 3/2 peak at 583.0 eV which are mixed of Te^0 and Te^{2-}.

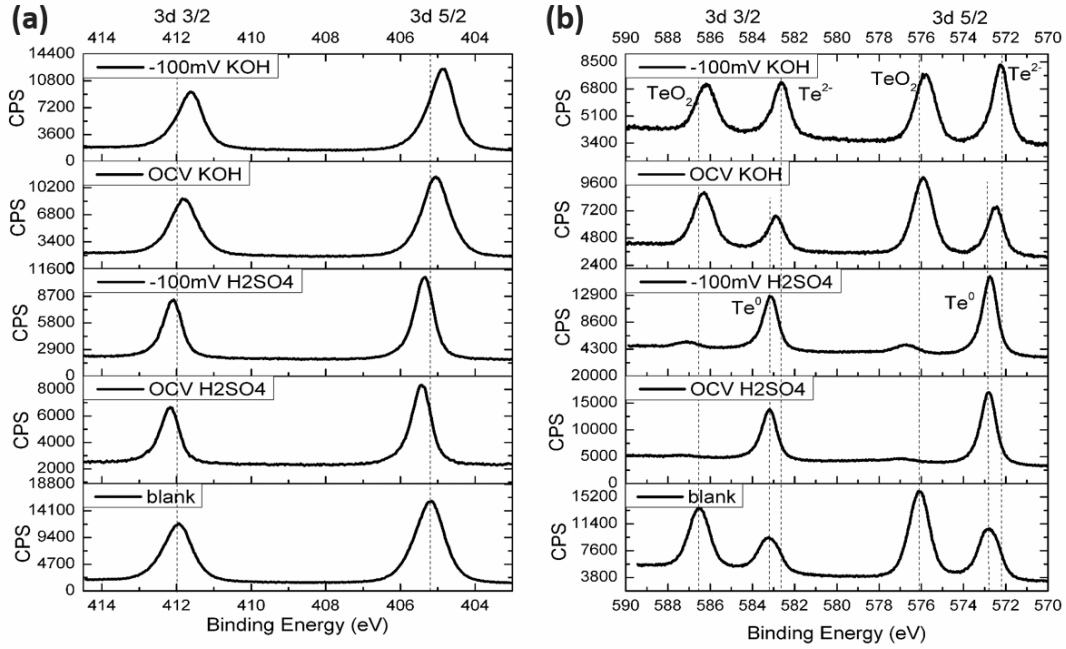

Figure 4.6 XPS of (a) Cd, (b) Te peaks of n-CdTe electrodes (dark). From top to bottom: after 24 hours biased at -100 mV vs. RHE in H_2(g)-saturated 1.0 M KOH(aq); after 24 hours left at open circuit voltage in H_2(g)-saturated 1.0 M KOH(aq); after 24 hours biased at -100 mV vs. RHE in H_2(g)-saturated 1.0 M H_2SO_4(aq); after 24 hours left at open circuit voltage in H_2(g)-saturated 1.0 M H_2SO_4(aq); before electrochemical test.

Electrochemical stability of n-CdTe with Pt catalyst

Figure 4.7 shows the chronoamperometry profiles of n-CdTe electrodes with ~ 2nm sputtered Pt catalyst on the front surface biased at -100 mV vs. RHE in H_2(g)-saturated 1.0 M H_2SO_4(aq) (Figure 4.7a) and 1.0 M KOH(aq) (Figure 4.7b) in the dark. Both curves showed that the current density became stable either in 1.0 M H_2SO_4(aq) or in 1.0 M KOH(aq) after 5 hours. The current density in 1.0 M H_2SO_4(aq) starts at around -0.1 mA/cm^2 and get to around -0.2 mA/cm^2 after 1 hour, which is much bigger than the μA/cm^2 magnitude without Pt, indicating the good catalytic performance of Pt in acid. The current density in 1.0 M KOH(aq) starts at around -0.03 mA/cm^2 and stayed at around -0.003 mA/cm^2 after 1 hour,

which is not much different with the n-CdTe without Pt in KOH. The chronoamperometry curve in 1.0 M H_2SO_4(aq) is more noisy than in 1.0 M KOH(aq).

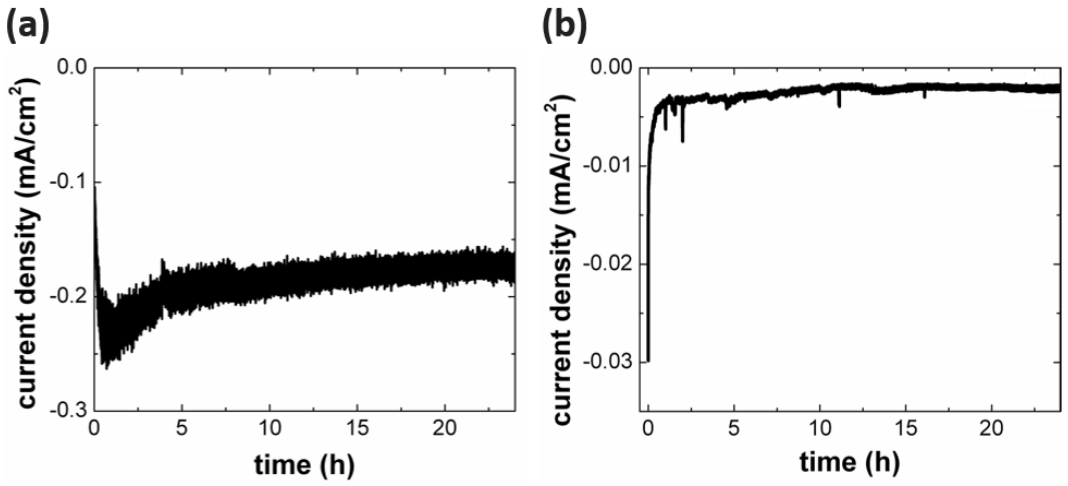

Figure 4.7. Chronoamperometry (current density vs. time) for the n-CdTe electrodes (dark) with ~ 2nm sputtered Pt catalyst on the front surface biased at -100 mV vs. RHE over 24 hours in H_2(g)-saturated (a) 1.0 M H_2SO_4(aq); (b) 1.0 M KOH(aq).

Figure 4.8 shows the concentrations and amount of dissolved Cd and Te species of n-CdTe electrodes with ~ 2 nm sputtered Pt catalyst on the front surface baised at -100 mV vs. RHE in the dark over 24 hours in H_2(g)-saturated 1.0 M H_2SO_4(aq) and 1.0 M KOH(aq). Like in the study of electrochemical stability and chemical stability of n-CdTe, the concentrations and amount of dissolved Cd and Te species are normalized to 1 cm^2 n-CdTe electrode area, and the concentrations are adjusted to a 25 mL volume. The corrosion thickness in Figure 4.8a and 4.8b is calculated from the amount of dissolved Te species (in μmol, Figure 4.8c and 4.8d) and the density of CdTe. Comparing Figure 4.8a with Figure 4.8b, and comparing Figure 4.8c with 4.8d, we could see that the dissolved concentrations of Cd in 1.0 M H_2SO_4(aq) are higher than in the 1.0 M KOH(aq), but the dissolved concentrations of Te in

1.0 M H_2SO_4(aq) are about the same as in the 1.0 M KOH(aq). The concentrations of dissolved Cd species in 1.0 M H_2SO_4(aq) were ~60 μg/L at 1 hour, and reached ~90 μg/L at 24 hours. The concentrations of Cd in 1.0 M KOH(aq) were less than 10 μg/L during the 24 hours and changed very little. Comparing Figure 4.8ab with Figure 4.4ab, we could see that the Cd concentrations are very similar when with Pt biased at -100 mV and when left with no applied potential with no Pt in both 1.0 M H_2SO_4(aq) and 1M KOH. and ~10 μg/L in 1.0 M KOH(aq) at 24 hours. The concentration of dissolved Te species in 1.0 M H_2SO_4(aq) stayed at ~ 50 μg/L after 1 hour, and stayed at ~50 μg/L in 1.0 M KOH(aq) most of the time. When with Pt catalyst and biased at -100 mV vs. RHE, only the concentration of dissolved Cd species in both 1.0 M H_2SO_4(aq) showed a slow increasing trend, and the concentration of Cd in 1.0 M KOH(aq) and concentrations of dissolved Te species in both 1.0 M H_2SO_4(aq) and 1.0 M KOH(aq) remained pretty flat, and the values of the concentrations are the smallest among the three test conditions. The corrosion rates in thickness were about 0.0 nm/h in 1.0 M H_2SO_4(aq), and 0.0 nm/h in 1.0 M KOH(aq), respectively, if calculated from Te as described above. In 1.0 M H_2SO_4(aq) the corrosion rate was 0.29 nm/h if calculated from Cd. In either calculation method, the corrosion rate was lower than the other two test conditions.

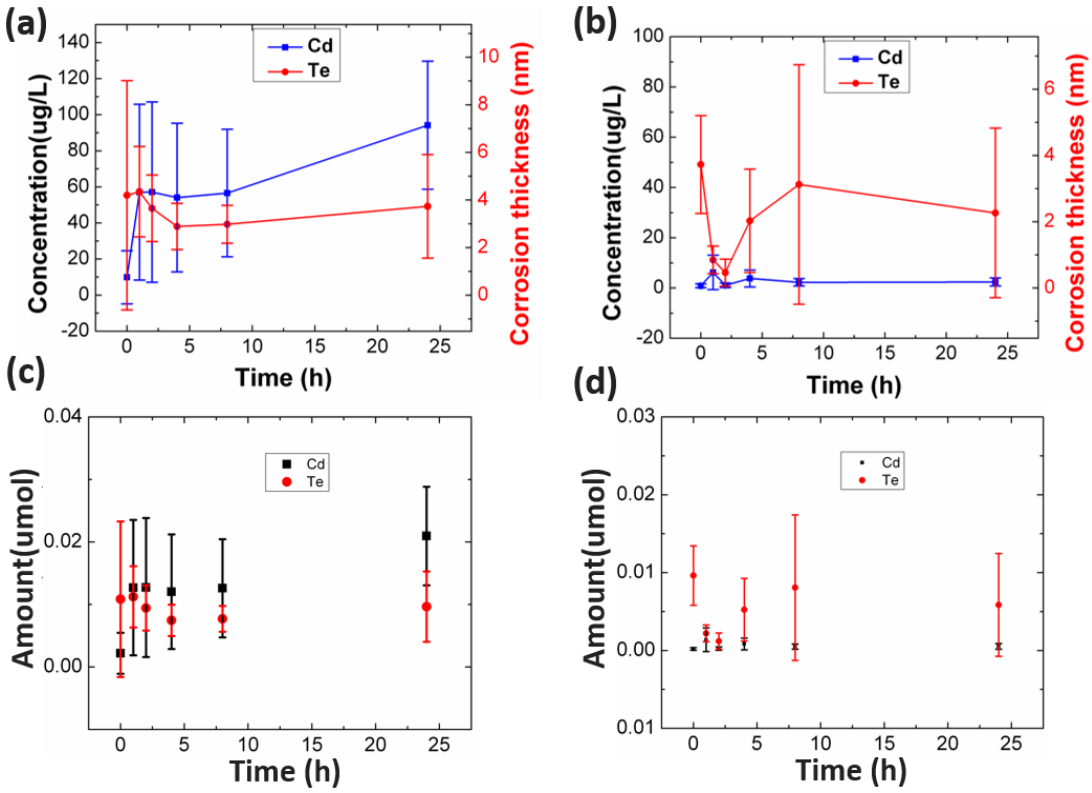

Figure 4.8 Concentrations of dissolved Cd, Te species in the working compartment when ~ 2 nm Pt catalyst is applied and biased at -100 mV vs. RHE in the dark over 24 hours, normalized to 1 cm^2 n-CdTe electrode area and adjusted to 25 mL volume, in H_2(g)-saturated (a) 1.0 M H_2SO_4(aq); (b) 1.0 M KOH(aq).

Figure 4.9 shows the SEM images of the n-CdTe electrodes with ~ 2 nm Pt catalyst after the 24-hour chronoamperometry test in the dark biased at -100 mV vs. RHE in H_2(g)-saturated 1.0 M H_2SO_4(aq) and 1.0 M KOH(aq). Although the electrode in 1.0 M H_2SO_4 (aq) showed very few small holes, both n-CdTe electrodes remained very smooth, which corresponds to the ICP-MS results of very little corrosion.

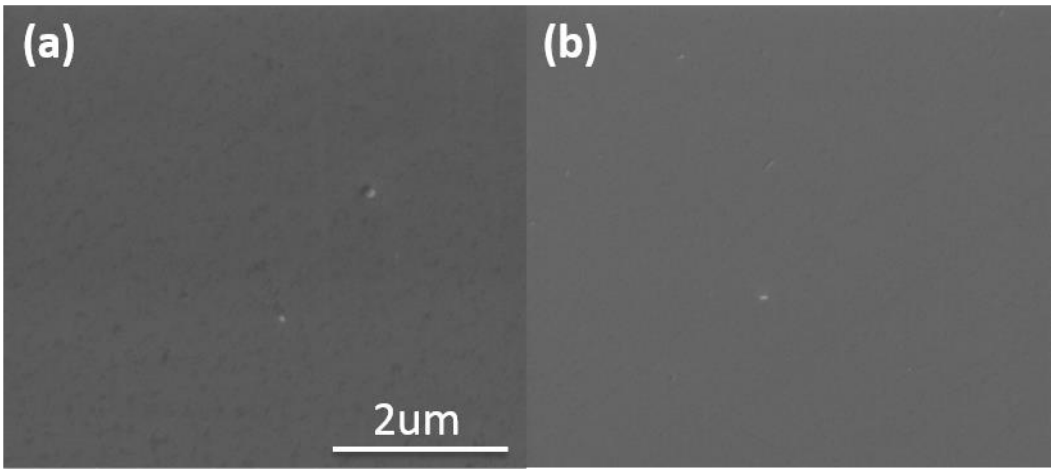

Figure 4.9. SEM images of n-CdTe electrodes with ~ 2 nm sputtered Pt catalyst on the front surface after being biased at -100 mV vs. RHE in the dark for 24 hours in H_2(g)-saturated (a) 1.0 M H_2SO_4(aq); (b) 1.0 M KOH(aq).

4.3 Discussion

CdTe is known to form a native oxide layer in air, mainly consisting of TeO_2 and $CdTeO_3$, and the thickness of native oxide evolves over time. [74]Chemical etching can obtain a consistent surface layer, and can decrease the surface roughness and remove structural damage resulting from the mechanical polishing process from factory production of CdTe substrates. Bromine/methanol (Br_2/CH_3OH) solutions of various concentrations are used as a common etchant. [75] During the etching process, Br_2 oxidizes the tellurium anions to neutrally charged tellurium, as shown in Equation 4.1.

$$Br_2 + Te^{2-} \longrightarrow 2Br^- + Te^0 \qquad (4.1)$$

Br_2/CH_3OH etching results in an enrichment of elemental Te at the surface. [76] The enrichment of Te increases the leakage current [77], and the leakage current could potentially lead to a degradation of the semiconductor in photoelectrochemical cells [78]. Passivating

the Br_2/CH_3OH etched, Te rich surface with hydrogen peroxide can develop a thin insulating oxide layer and minimize the leakage current. [79] The reaction is shown in Equation 4.2, 4.3, and 4.4.

$$2H_2O_2 + Te^0 \longrightarrow TeO_2 + 2H_2O \qquad (4.2)$$

$$3H_2O_2 + Te^{2-} + 2H^+ \longrightarrow TeO_2 + 4H_2O \qquad (4.3)$$

$$3H_2O_2 + CdTe \longrightarrow CdTeO_3 + 3H_2O \qquad (4.4)$$

To study the electrochemical stability of n-CdTe, the n-CdTe electrodes were biased at -100 mV vs. RHE for 24 hours (Figure 4.1). The dark n-CdTe electrodes were biased at -100 mV vs. RHE because in practice many good HER catalysts have an overvoltage of < 100 mV and exhibit a current density of $\geq$10 mA/cm^2 which is reasonable for HER. [80] Here the current densities were ~ 0.01 mA/cm^2 at 24 hours in 1.0 M H_2SO_4(aq) and 1.0 M KOH(aq), indicating sluggish HER kinetics on bare n-CdTe electrodes in the dark without catalyst. The current density curves in the last few hours were both very noisy in 1.0 M H_2SO_4(aq) and 1.0 M KOH(aq), indicating that there were some corrosion reactions going on. The current density in 1.0 M KOH(aq) got to a stable value after 15 hours, which indicates some equilibrium was reached.

To have an idea of how much the current was used for corrosion, and how fast n-CdTe corroded at -100 mV vs. RHE in the electrochemical tests, we collected solution samples for ICP-MS analysis. The results are in Figure 4.2. If we assume a 2-electron charge transfer corrosion process, the corrosion faradaic efficiencies (i.e., the amount of charge transferred in the corrosion process divided by the total amount of charge passed by the potentiostat) were 2.76% in 1.0 M H_2SO_4(aq), and 0.94% in 1.0 M KOH(aq). Even if we assume a 6-electron corrosion process, the corrosion faradaic efficiencies would be 8.28% and 2.82%, respectively. This means that if the corrosion was driven by electrical currents, only a small portion of the currents came from corrosion, and most of the currents were producing

hydrogen. The corrosion rates also agreed that n-CdTe did not corrode significantly in such conditions, with 0.33 nm/h in 1.0 M H_2SO_4(aq), and about 0.10 nm/h in 1.0 M KOH(aq), respectively. In the pourbaix diagram drawn by Zeng, C. et. al.[81], CdTe remains stable from pH -2 to 14 between 0 and -0.5 V vs. RHE, and in the pourbaix diagram drawn by Dremlyuzhenko, S. G. et. al.[82], CdTe is in the form of Cd^{2+} + Te at -100 mV vs. RHE from pH -2 to 2, and in the form of CdTe at -100 mV. Vs. RHE at pH 14. Here we did see that biased at -100 mV vs. RHE, CdTe in 1.0 M H_2SO_4(aq) was less stable than in 1.0 M KOH(aq), both from the ICP-MS results and from that Figure 4.3b showed more pits than in Figure 4.3c. The less stability in 1.0 M H_2SO_4(aq) is likely to be caused by the Cd^{2+} ions leaching out of n-CdTe.

At hour 0 of the blank samples, Cd was close to 0, which agrees with our use of high purity acid or base or other chemicals, but Te had higher concentrations and bigger error bars, and this not only due to variations in samples, but also results from the detection limits of the ICP-MS. In the standard calibration solutions used for ICP-MS, the most dilute standard solution for Cd had a concentration of 0.1704 $\pm$ 6.0815 μg/L, but for Te it was 0.8024 $\pm$ 46.6928 μg/L. Since our ICP-MS test samples were diluted to 1/5 of the original sampled concentration, Te errors can be magnified by 5 times to 233.464 μg/L if we only take the dilution into account without further volume adjustment. This error makes it hard to see how Te concentrations change during one experiment setting over time, because the concentration change was small compared to the error, but still makes Te concentrations in different experiment settings comparable, because those values are obviously different in scale (Figure 4.2, 4.4, and 4.8) and the systematic error is small compared to the differences between the concentrations in different experimental conditions.

Since the corrosion faradaic efficiencies were small, less than 10% from previous calculation, to further investigate if the corrosion is driven by electrochemical reactions or chemical reactions, control samples of n-CdTe electrodes were kept at no potential in H_2(g) saturated 1.0 M H_2SO_4(aq) and 1.0 M KOH(aq) and collected samples for ICP-MS. In 1.0 M H_2SO_4(aq), Cd showed a concentration of ~135 μg/L at -100 mV vs. RHE at 24 hours, and

~90 μg/L at OCV at 24 hours. Electrochemical leaching concentration at 24 hours is higher than the chemical one by ~45 μg/L. This indicates that in 1.0 M H_2SO_4(aq) Cd leaches away from CdTe under chemical corrosion, and a negative bias at -100 mV vs. RHE increases the leaching. This cannot be due to that a negative potential reduces Cd^{2+} in CdTe to Cd^0, because Cd^0 can be plated and bound to the electrode surface, and thus the dissolved Cd in solution should be decreased. The XPS peaks of Cd (Figure 4.6a) shift to a higher binding energy from non-tested CdTe to CdTe tested in 1.0 H_2SO_4(aq), either at OCV or at -100 mV vs. RHE, which also indicates that the Cd species was not reduced on the surface. Since there must be some reduction reaction driven by the negative potential to increase Cd leaching, it can only come from the Te side. Te^{2-} cannot be further reduced, and we see plenty of Te^0 peaks but no Te^{2-} peaks in Figure 6b, so Te^0 which was generated from surface etching was not reduced to Te^{2-}. The possible reaction is that the $CdTeO_3$ from Br_2/CH_3OH etching and H_2O_2 treatment (Equation 4.4) was reduced to Te^0 by the negative potential and Cd^{2+} leached away (Equation 4.5). This is in agreement with the Cd peak shifts in XPS (Figure 4.6a) and the Te^0 on the surface (Figure 4.6b), and also with a decreased Te concentration in the solution, from ~ 250 μg/L at OCV at 24 hours to ~180 μg/L at -100 mV at 24 hours. TeO_2 and $CdTeO_3$ from surface treatment (Equation 4.3 and 4.4) dissolved both in OCV and under -100 mV vs. RHE bias (Figure 4.6b), and most of it dissolved after being in the electrolyte for 1 hour (Figure 4.2 and 4.4). At 1 hour, the concentrations of Te at OCV was ~150 μg/L and at -100 mV vs. RHE it was ~180 μg/L, so the corrosion is concluded to be mainly chemical corrosion as in Equation 4.6 and 4.7, and under negative bias, electrochemical corrosion (Equation 4.5) exposed more $CdTeO_3$ and TeO_2 to be dissolved (Equation 4.6 and 4.7) and thus at hour 1 there was a higher concentration of Te at -100 mV vs. RHE than at OCV. However, as time went by, the electrochemical corrosion in Equation 4.5 plated Te^0 on the surface of CdTe, which to some extent blocks the continuing chemical corrosion of $CdTeO_3$ and TeO_2, so at 24 hours, at -100 mV vs. RHE the solution showed a lower concentration of Te than at OCV. The SEM images (Figure 4.3b and 4.5a) shows that n-CdTe had a rougher surface at -100 mV vs. RHE than at OCV, indicating that some parts on the surface at -100 mV were less exposed and corroded less, resulting in a rougher surface with pits and bumps, and the surface at OCV corroded in a more uniform way.

$$CdTeO_3 + 4e^- + 6H^+ \longrightarrow Cd^{2+} + Te^0 + 3H_2O \quad (4.5)$$

$$CdTeO_3 + 6H^+ \longrightarrow Cd^{2+} + Te^{4+} + 3H_2O \quad (4.6)$$

$$TeO_2 + 4H^+ \longrightarrow Te^{4+} + 2H_2O \quad (4.7)$$

In 1.0 M KOH(aq), Cd showed a concentration of ~40 μg/L at -100 mV vs. RHE at 24 hours, and ~10 μg/L at OCV at 24 hours. Te showed a concentration of ~80 μg/L at -100 mV vs. RHE at 24 hours, and ~460 μg/L at OCV at 24 hours. At OCV, Te leaching was significantly higher at OCV and was greatly reduced at -100 mV vs. RHE. This indicates that in 1.0 M KOH(aq) there was some oxidation of Te species at OCV which was chemical corrosion, and a negative bias at -100 mV vs. RHE suppressed the oxidation. Figure 4.6b shows a small shift of the TeO_2 peaks to lower binding energies (binding energy of TeO_2 from higher to lower: before test, OCV, -100 mV vs. RHE), and Figure 4.6a shows that Cd peaks shift to lower binding too, suggesting that TeO_2 or $Cd^{(2+)}$ cannot be the chemical that got oxidized. Te^0 could be the species that was oxidized in the chemical corrosion, since in Figure 4.6b at OCV the Te^0 peak showed a smaller ratio of the total Te than before test. Te^{2-} was also possibly oxidized. At -100 mV vs. RHE, cathodic reduction occurs, possibly of the reactions in Equation 4.8 and 4.9, which reduced chemical corrosion of Te leaching away from the electrode, so we see less Te dissolved electrochemically, and an increasing peak of Te^{2-} in Figure 4.6b. The more Te leaching in chemical corrosion at OCV led to a rougher surface of the n-CdTe electrode in Figure 4.5b.

$$Cd^{2+} + Te^0 + 2e^- \longrightarrow CdTe \quad (4.8)$$

$$CdTeO_3 + Te^0 + 2e^- \longrightarrow CdTe + TeO_2 \quad (4.9)$$

With ~2 nm Pt catalyst, the dissolution of Cd and Te was greatly reduced compared to without Pt in 1.0 M H_2SO_4(aq) and 1.0 M KOH(aq), with very small corrosion rates close to

0.0 nm/h, indicating that in PEC cells with catalyst, the corrosion of CdTe could be negligible.

4.4 Conclusion

Corrosion of n-CdTe dark electrodes in 1.0 M H_2SO_4(aq) and 1.0 M KOH(aq), biased at -100 mV vs. RHE, with no bias at OCV, and with Pt catalyst biased at -100 mV vs. RHE was studied. The higher dissolved products at OCV in both acid and base suggests chemical corrosion. Electrochemically the corrosion was reduced in both acid and base. When Pt catalyst is applied, the corrosion rate of CdTe was close to 0, indicating a possibility for it to be used as a stable electrode in PEC cells.

Chapter 5

CONCLUSIONS

In this thesis, the electrical and mechanical properties of the interfaces of the common Si/Pt-NPs electrodes were investigated on a nanoscale, revealing the factors limiting the Si/Pt-NPs electrode performance. Efforts have been made to engineer the interface of Si/Pt electrodes with ALD TiO_2, and the improvement of annealed TiO_2 over as grown TiO_2 was explored. Also, we conducted research on the stability/corrosion behaviors of another promising photocathode semiconductor material CdTe, and found that the corrosion mostly comes from chemical corrosion, and is greatly reduced at a -100 mV vs. RHE bias and with Pt catalyst, indicating the possibility of CdTe to be a stable cathode in PEC cells.

Future directions of research can include engineering the semiconductor/catalyst interface with a better material and giving a better performance. Corrosion study of CdTe in other different conditions, i.e., pH, and different biases, is also an interesting area to continue to explore and make the corrosion study more thorough. Extending the stability/corrosion study of CdTe from dark electrodes to photoelectrodes and utilizating CdTe as a photocathode in a real device should also be developed.

PEC cells are a good way to harvest sunlight. A great deal of progress has been made in the field. By engineering a better interface and having a better stability, the photocathode part could be better and contribute to the full PEC device, enabling a new way to generate renewable fuels and decrease carbon emissions.

BIBLIOGRAPHY

1. Walter, M.G.W., E. L.; McKone, J. R.; Boettcher, S. W.; Mi, Q.; Santori, E. A.; Lewis, N. S., *Solar Water Splitting Cells.* Chem. Rev., 2010. **110**: p. 6446-6473.
2. Lewis, N.S., *Research opportunities to advance solar energy utilization.* Science, 2016. **351**(6271): p. 353-+.
3. Walter, M.G., et al., *Solar Water Splitting Cells.* Chemical Reviews, 2010. **110**(11): p. 6446-6473.
4. Nellist, M.R., et al., *Semiconductor-Electrocatalyst Interfaces: Theory, Experiment, and Applications in Photoelectrochemical Water Splitting.* Accounts of Chemical Research, 2016. **49**(4): p. 733-740.
5. Huang, Q.Y., Z.; Xiao, X., *Recent progress in photocathodes for hydrogen evolution.* J. Mater. Chem. A., 2015. **3**: p. 15824-15837.
6. Li, J.W., N., *Semiconductor-based photocatalysts and photoelectrochemical cells for solar fuel generation: a review.* Catal. Sci. Technol., 2015. **5**: p. 1360-1384.
7. Ohashi, K.M., J.; Bockris, J. O., *Stable photoelectrochemical cells for the splitting of water.* Nature, 1977. **266**: p. 610-611.
8. Mathew, X.B., A.; Turner, J. A.; Dhere, R.; Mathews, N. R.; Sebastian, P. J., *Photoelectrochemical Characterization of Surface Modified CdTe for Hydrogen Production.* J. New Mater. Electrochem. Syst., 2002. **5**: p. 149-154.
9. Boettcher, S.W.W., E. L.; Putnam, M. C.; Santori, E. A.; Turner-Evans, D.; Kelzenberg, M. D.; Walter, M. G.; McKone, J. R.; Brunschwig, B. S.; Atwater, H. A.; Lewis, N. S., *Photoelectrochemical Hydrogen Evolution Using Si Microwire Arrays.* J. Am. Chem. Soc., 2011. **133**(5): p. 1216-1219.
10. Seger, B.P., T.; Laursen, A. B.; Vesborg, P. C. K.; Hansen, O.; Chorkendorff, I., *Using TiO2 as a Conductive Protective Layer for Photocathodic H2 Evolution.* J. Am. Chem. Soc., 2013. **135**: p. 1057−1064.
11. Esposito, D.V.L., I.; Moffat, T. P.; Talin, A. A., *H2 evolution at Si-based metal–insulator–semiconductor photoelectrodes enhanced by inversion channel charge collection and H spillover.* Nat. Mater., 2013. **12**: p. 562-568.
12. Kast, M.G.E., L. J.; Gurnon, N. J.; Nadarajah, A.; Boettcher, S. W., *Solution-Deposited F:SnO2/TiO2 as a Base-Stable Protective Layer and Antireflective Coating for Microtextured Buried-Junction H2-evolving Si Photocathodes.* ACS Appl. Mater. Interfaces, 2014. **6**: p. 22830−22837.
13. Lee, M.H.T., K.; Zhang, J.; Kapadia, R.; Zheng. M.; Chen, Y.; Nah, J.; Matthews, T. S.; Chueh, Y.; Ager, J. W.; Javey, A., *p-Type InP Nanopillar Photocathodes for Efficient Solar-Driven Hydrogen Production.* Angew. Chem., 2012. **51**(43): p. 10760-10764.
14. Brown, D.E.M., M. N.; Man, M. C. M.; Turner, A. K., *Preparation and characterization of low overvoltage transition metal alloy electrocatalysts for hydrogen evolution in alkaline solutions.* Electrochim. Acta1984. **29**(11): p. 1551-1556.

15. Nørskov, J.K.B., T.; Logadottir, A.;Kitchin, J. R.; Chen, J. G.; Pandelov, S.; Stimming, U., *Trends in the Exchange Current for Hydrogen Evolution.* J. Electrochem. Soc., 2005. **152**(3): p. J23-J26.
16. Sudhagar, P.e.a., *Hydrogen and CO2 Reduction Reactions: Mechanisams and Catalysts*, in *Photoelectrochemical Solar Fuel Production: From Basic Principles to Advanced Devices*, S. Giménez, and Bisquert, J., Editor. 2016, Springer. p. 109-111.
17. Zheng, Y.J., Y.; Zhu, Y.; Li, L. H.; Han, Y.; Chen, Y.; Jaroniec, M.; Qiao, S. Z., *High Electrocatalytic Hydrogen Evolution Activity of an Anomalous Ruthenium Catalyst.* J. Am. Chem. Soc., 2016.
18. McKone, J.R.S., B. F.; Werlang, C. A.; Lewis, N. S.; Gray, H. B., *Ni–Mo Nanopowders for Efficient Electrochemical Hydrogen Evolution.* ACS Catal., 2013. **3**(2): p. 166-169.
19. Hou, Y.A., B. L.; Vesborg, P. C. K.; Björketun, M. E.; Herbst, K.; Bech, L.; Setti, A. M.; Damsgaard, C. D.; Pedersen, T.; Hansen, O.; Rossmeisl, J.; Dahl, S.; Nørskov, J. K.; Chorkendorff, I. , *Bioinspired molecular co-catalysts bonded to a silicon photocathode for solar hydrogen evolution.* Nat. Mater., 2011. **10**: p. 434-438.
20. Seger, B.L., A. B.; Vesborg, P. C. K.; Pedersen, T.; Hansen, O.; Dahl, S.; Chorkendorff, I., *Hydrogen Production Using a Molybdenum Sulfide Catalyst on a Titanium-Protected n+p-Silicon Photocathode.* Angew. Chem. Int. Ed., 2012. **51**(36): p. 9128-9131.
21. Seger, B.T., D. S.; Pedersen, T.; Vesborg, P. C. K.; Hansen, O.; Grätzel, M.; Chorkendorff, I., *Silicon protected with atomic layer deposited TiO2: durability studies of photocathodic H2 evolution.* RSC Adv., 2013. **3**: p. 25902.
22. Ji, L.M., M. D.; Wang, S.; Posadas, A. B.; Li, X.; Huang, H.; Lee, J. C.; Demkov, A. A.; Bard, A. J.; Ekerdt, J. G.; Yu, E. T., *A silicon-based photocathode for water reduction with an epitaxial SrTiO3 protection layer and a nanostructured catalyst.* Nat Nanotech, 2014. **10**: p. 84-90.
23. Das, C.T., M.; Schmeisser, D., *Si microstructures laminated with a nanolayer of TiO2 as long-term stable and effective photocathodes in PEC devices.* Nanoscale, 2015. **7**: p. 7726.
24. Seo, J.K., H. J.; Pekarek, R. T.; Rose, M. J., *Hybrid Organic/Inorganic Band-Edge Modulation of p-Si(111) Photoelectrodes: Effects of R, Metal Oxide, and Pt on H2 Generation.* J. Am. Chem. Soc., 2015. **137**(9): p. 3173–3176.
25. Andoshe, D.M.C., S.; Shim, Y.; Lee, S. H.; Kim, Y.; Moon, C. W.; Kim, D. H.; Lee, S. Y.; Kim, T.; Park, H. K.; Lee, M. G.; Jeon, J.; Nam, K. T.; Kim, M.; Kim, J. K.; Oh, J.; Jang, H. W., *A wafer-scale antireflective protection layer of solution-processed TiO2 nanorods for high performance silicon-based water splitting photocathodes.* J. Mater. Chem. A., 2016. **4**: p. 9477-9485.
26. Zhou, J.D., S.; Dong, W.; Su, X.; Fang, L.; Zheng, F.; Wang, X.; Shen, M., *Efficient and stable MoS2 catalyst integrated on Si photocathodes by photoreduction and post-annealing for water splitting.* Appl. Phys. Lett. , 2016. **108**: p. 213905.
27. Lin, Y., Battaglia, C., Boccard, M., Hettick, M., Yu, Z., Ballif, C., Ager, J. W., and Javey, A., *Amorphous Si Thin Film Based Photocathodes with High Photovoltage for Efficient Hydrogen Production.* Nano Lett., 2013. **13**(11): p. 5615–5618.

28. Lai, Y.P., H. S.; Zhang, J. Z.; Matthews, P. D.; Wright, D. S.; Reisner, E., *A Si Photocathode Protected and Activated with a Ti and Ni Composite Film for Solar Hydrogen Production.* Chem. Eur. J., 2015. **21**: p. 3919 – 3923.
29. Feng, J.G., M.; Kenney, M. J.; Wu, J. Z.; Zhang, B.; Li, Y.; Dai, H., *Nickel-coated silicon photocathode for water splitting in alkaline electrolytes.* Nano Research, 2015. **8**(5): p. 1577-1583.
30. Bae, D.S., S.; Thorsteinsson, E. B.; Pedersen, T.; Hansen, O.; Seger, B.; Vesborg, P. C. K.; Ólafsson, S.; Chorkendorff, I., *Protection of Siphotocathode usingTiO2 deposited by high power impulse magnetron sputtering for H2 evolution in alkaline media.* Solar Energy Materials & Solar Cells, 2016. **144**: p. 758-765.
31. Boettcher, S.W., et al., *Energy-Conversion Properties of Vapor-Liquid-Solid-Grown Silicon Wire-Array Photocathodes.* Science, 2010. **327**(5962): p. 185-187.
32. Boettcher, S.W., et al., *Photoelectrochemical Hydrogen Evolution Using Si Microwire Arrays.* Journal of the American Chemical Society, 2011. **133**(5): p. 1216-1219.
33. Lombardi, I., et al., *Effect of Pt particle size and distribution on photoelectrochemical hydrogen evolution by p-Si photocathodes.* Langmuir, 2007. **23**(24): p. 12413-12420.
34. McKone, J.R., et al., *Evaluation of Pt, Ni, and Ni-Mo electrocatalysts for hydrogen evolution on crystalline Si electrodes.* Energy & Environmental Science, 2011. **4**(9): p. 3573-3583.
35. Bhuvana and G.U. Kulkarni, *Optimizing growth conditions for electroless deposition of Au films on Si(111) substrates.* Bulletin of Materials Science, 2006. **29**(5): p. 505-511.
36. Arrington, D., et al., *Copper electrodeposition onto the dendrimer-modified native oxide of silicon substrates.* Electrochimica Acta, 2008. **53**(5): p. 2644-2649.
37. Amusan, A.A., et al., *Ag films grown by remote plasma enhanced atomic layer deposition on different substrates.* Journal of Vacuum Science & Technology A, 2016. **34**(1).
38. Utsumi, J., K. Ide, and Y. Ichiyanagi, *Room temperature bonding of SiO2 and SiO2 by surface activated bonding method using Si ultrathin films.* Japanese Journal of Applied Physics, 2016. **55**(2).
39. Wrobel, E., P. Kowalik, and J. Mazurkiewicz, *Selective metallization of solar cells.* Microelectronics International, 2015. **32**(1): p. 1-7.
40. J. A. Aguiar, N.C.A., and N. R. Neale, *Revealing the semiconductor–catalyst interface in buried platinum black silicon photocathodes.* J. Mater. Chem. A., 2016. **4**: p. 8123-8129.
41. P. Gorostiza, R.D., J. Servat, F. Sanz, and J. R. Morante, *Atomic Force Microscopy Study of the Silicon Doping Influence on the First Stages of Platinum Electroless Deposition.* J. Electrochem. Soc., 1997. **144**(3): p. 909-914.
42. Kaemmer, S.B., *Introduction to Bruker's ScanAsyst and PeakForce Tapping AFM Technology.* Bruker Application Notes, 2011. **133**: p. 1-12.
43. Li, C., Minne, S., Pittenger, B. & Mednick, A., in *Bruker Application Notes*. 2011. p. 1-12.

44. Huang, Z.D.W., P.; Poddar, R.; Li, C.; Mark, A.; Nellist, M. R.; Chen, Y.; Jiang, J.; Papastavrou, G.; Boettcher, S. W.; Xiang, C.; Brunschwig, B. S., Microscopy Today, 2016. **24**(6): p. 18-25.
45. Nellist, M.C., Y.; Mark, A.; Gödrich, S.; Stelling, C.; Jiang, J.; Poddar, R.; Li, C.; Kumar, R.; Papastavrou, G.; Retsch, M.; Brunschwig, B.; Huang, Z.; Xiang, C.; Boettcher, S., *Atomic force microscopy with nanoelectrode tips for high resolution electrochemical, nanoadhesion and nanoelectrical imaging.* Nanotechnology, 2017. **28**.
46. Sze, S.M.N., K. K., *Physics of Semiconductor Devices*. 3rd ed. 2007: Wiley.
47. Huang, Z., et al., *PeakForce Scanning Electrochemical Microscopy with Nanoelectrode Probes.* Microscopy Today, 2016. **24**(06): p. 18-25.
48. Hunger, R., et al., *Chemical and electronic characterization of methyl-terminated Si(111) surfaces by high-resolution synchrotron photoelectron spectroscopy.* Physical Review B, 2005. **72**(4).
49. Michaelson, H.B., *Relation Between an Atomic Electronegativity Scale and the Work Function.* 1978. **22**(1): p. 72-80.
50. Rossi, R.C. and N.S. Lewis, *Investigation of the size-scaling behavior of spatially nonuniform barrier height contacts to semiconductor surfaces using ordered nanometer-scale nickel arrays on silicon electrodes.* Journal of Physical Chemistry B, 2001. **105**(49): p. 12303-12318.
51. Smith, W.A., et al., *Interfacial band-edge energetics for solar fuels production.* Energy & Environmental Science, 2015. **8**(10): p. 2851-2862.
52. Lin, F.D. and S.W. Boettcher, *Adaptive semiconductor/electrocatalyst junctions in water-splitting photoanodes.* Nature Materials, 2014. **13**(1): p. 81-86.
53. Gorostiza, P., et al., *Atomic force microscopy study of the silicon doping influence on the first stages of platinum electroless deposition.* Journal of the Electrochemical Society, 1997. **144**(3): p. 909-914.
54. Ego, T.H., T.; Morii, Y.; Fukumuro, N.; Yae, S.; Matsuda, H., *AFM Analysis for Initial Stage of Electroless Displacement Deposition of Silver on Silicon Surface.* ECS Transactions, 2013. **50**(52): p. 143.
55. Nellis, M.R., et al., *Atomic Force Microscopy with Nanoelectrode Tips for High Resolution Electrochemical, Nanoadhesion and Nanoelectrical Imaging.* Nanotechnology, 2017. **28**: p. 095711.
56. Chen, S.Y. and L.W. Wang, *Thermodynamic Oxidation and Reduction Potentials of Photocatalytic Semiconductors in Aqueous Solution.* Chemistry of Materials, 2012. **24**(18): p. 3659-3666.
57. Lin, Y.J., et al., *Amorphous Si Thin Film Based Photocathodes with High Photovoltage for Efficient Hydrogen Production.* Nano Letters, 2013. **13**(11): p. 5615-5618.
58. Malizia, M., et al., *Formation of a p-n heterojunction on GaP photocathodes for H-2 production providing an open-circuit voltage of 710 mV.* Journal of Materials Chemistry A, 2014. **2**(19): p. 6847-6853.
59. Seger, B., et al., *Using TiO2 as a Conductive Protective Layer for Photocathodic H-2 Evolution.* Journal of the American Chemical Society, 2013. **135**(3): p. 1057-1064.

60. Seger, B., et al., *Silicon protected with atomic layer deposited TiO2: durability studies of photocathodic H-2 evolution.* Rsc Advances, 2013. **3**(48): p. 25902-25907.
61. Seger, B., et al., *Silicon protected with atomic layer deposited TiO2: conducting versus tunnelling through TiO2.* Journal of Materials Chemistry A, 2013. **1**(47): p. 15089-15094.
62. Chen, Y.W., et al., *Atomic layer-deposited tunnel oxide stabilizes silicon photoanodes for water oxidation.* Nature Materials, 2011. **10**(7): p. 539-544.
63. Hu, S., et al., *Amorphous TiO2 coatings stabilize Si, GaAs, and GaP photoanodes for efficient water oxidation.* Science, 2014. **344**(6187): p. 1005-1009.
64. Lichterman, M.F., et al., *Stabilization of n-cadmium telluride photoanodes for water oxidation to O-2(g) in aqueous alkaline electrolytes using amorphous TiO2 films formed by atomic-layer deposition.* Energy & Environmental Science, 2014. **7**(10): p. 3334-3337.
65. He, G., Fang, Q., Zhu, L., Liu, M., Zhang, L., *The structure and thermal stability of TiO2 grown by the plasma oxidation of sputtered metallic Ti thin films.* Chem Phys Lett, 2004. **395**: p. 259-263.
66. Matthew T. McDowell, M.F.L., Azhar I. Carim, Rui Liu, Shu Hu, Bruce S. Brunschwig, Nathan S. Lewis, *The influence of TiO2 crystal structure on the photoelectrochemical behavior of stabilized n-Si/TiO2/Ni photoanodes for water oxidation.* Submitted, 2015.
67. Warren, E.L., et al., *pH-Independent, 520 mV Open-Circuit Voltages of Si/Methyl Viologen(2+/+) Contacts Through Use of Radial n(+)p-Si Junction Microwire Array Photoelectrodes.* Journal of Physical Chemistry C, 2011. **115**(2): p. 594-598.
68. Lieber, C.M., C.M. Gronet, and N.S. Lewis, *Evidence against Surface-State Limitations on Efficiency of P-Si/Ch3cn Junctions.* Nature, 1984. **307**(5951): p. 533-534.
69. Bent, R.M.S.F., *Comparative Study of Titanium Dioxide Atomic Layer Deposition on Silicon Dioxide and Hydrogen-Terminated Silicon.* J. Phys. Chem. C, 2010. **114**(23): p. 10498–10504.
70. M. Perego, G.S., G. Scarel, M. Fanciulli, F. Wallrapp, *Energy band alignment at TiO2/Si interface with various interlayers.* J. Appl. Phys., 2008. **103**: p. 043509.
71. E. A. Kraut, R.W.G., J. R. Waldrop, S. P. Kowalczyk, *Semiconductor core-level to valence-band maximum binding-energy differences: Precise determination by x-ray photoelectron spectroscopy.* Phys. Rev. B, 1983. **28**: p. 1965.
72. E. A. Kraut, R.W.G., J. R. Waldrop, S. P. Eowalczyk, *Precise Determination of the Valence-Band Edge in X-Ray Photoemission Spectra: Application to Measurement of Semiconductor Inter face Potentials.* Phys. Rev. Lett., 1980. **44**: p. 1620-1623.
73. Klein A, M.T., Thissen A, Jaegermann W, Bunsen-Magazin, 2008. **10**(4): p. 124-139.
74. Zázvorka, J., Franc, J., Beran, L., Moravec, P., Pekárek, J., Veis, M., *Dynamics of native oxide growth on CdTe and CdZnTe X-ray and gamma-ray detectors.* Science and Technology of Advanced Materials, 2016. **17**: p. 792-798.
75. Babar, S., Sellin, P.J., Watts, J.F., Baker, M.A., *An XPS study of bromine in methanol etching and hydrogen peroxide passivation treatments for cadmium zinc telluride radiation detectors.* Appl. Surf. Sci., 2013. **264**: p. 681-686.

76. Kotinay, I.M., Tukhkoneny, L. M., Patsekinay, G. V., Shchukarevz, A. V., Gusinskii, G. M., *Study of CdTe etching process in alcoholic solutions of bromine.* Semicond. Sci. Technol., 1998. **13**: p. 890-894.
77. Bensalah, H., Plaza, J. L., Crocco, J., Zheng, Q., Carcelen, V., Bensouici, A., Dieguez, E., *The effect of etching time on the CdZnTe surface.* Appl. Surf. Sci., 2011. **257**(10): p. 4633-4636.
78. Nandjou, F., Haussener, S., *Degradation in photoelectrochemical devices: review with an illustrative case study.* J. Phys. D: Appl. Phys., 2017. **50**.
79. Özsan, M.E., Sellin, P. J., Veeramani, P. , Hinder, S. J., Monnier, M. L., Prekas, G. , Lohstroh, A., Baker, M. A., *Chemical etching and surface oxidation studies of cadmium zinc telluride radiation detectors.* Surf. Interface Anal., 2010. **42**: p. 795-798.
80. Saadi, F.H., Carim, A. I., Verlage, E., Hemminger, J. C., Lewis, N. S., Soriaga, M. P., *CoP as an Acid-Stable Active Electrocatalyst for the Hydrogen-Evolution Reaction: Electrochemical Synthesis, Interfacial Characterization and Performance Evaluation.* J. Phys. Chem. C, 2014. **118**: p. 29294-29300.
81. Zeng, C., Ramos-Ruiz, A., Field, J. A., Sierra-Alvarez, R., *Cadmium telluride (CdTe) and cadmium selenide (CdSe) leaching behavior and surface chemistry in response to pH and O2.* Journal of Environmental Management, 2015. **154**: p. 78-85.
82. Dremlyuzhenko, S.G., Voloshchuk, A. G, Zakharuk, Z. I., Yurijchuk, I. N. , *Thermodynamic Evaluation and Potentiometric Study of Cd 1 – x Mn x Te and Cd 1 – x Zn x Te Dissolution in Acid and Alkaline Solutions.* Inorganic Materials, 2008. **44**(1): p. 21-29.